Compton Scattering on Complex Materials -an investigation on the electronic structure of alkali-metal doped Si-clathrates

DISSERTATION

zur Erlangung des Doktorgrades der
Naturwissenschaften
des Fachbereiches Physik der Universität Dortmund

vorgelegt von

Martin Volmer

2006

Contents

Introduction

In search of more effective thermoelectric materials the concept of a phonon glass and an electron crystal (PGEC) is at the center of recent research [Fujita2006, Gao2005, Slack1995]. It suggests materials possessing electronic properties associated with a good semiconductor single crystal while having a thermal conductivity normally found in amorphous or glass-like materials. The figure of merit of a good thermoelectric material is defined by the quantity Z [Goldsmid1986]. It is often displayed as a dimensionless quantity ZT with T being the absolute temperature: $ZT = S^2\sigma/\kappa\ T$. Here S is the Seebeck coefficient, σ the electrical conductivity and κ the total thermal conductivity. It was in the mid 1990s, when group-IV clathrates reentered the focus of scientific interest as good candidate materials for thermo-electric applications. Group-IV clathrates are inclusion compounds built up of nanosized cage-like structures with trapped guest atoms or molecules in the center of the cages. The word 'clathrate' has its origin in the Greek word 'klethra', meaning 'enclosed by bars of a grating' and was introduced in science by Powell [Powell1948] in 1948. In 1952 Pauling and Marsh [Pauling1952] extended the term to the description of solid state gas hydrate structures, which are isostructural to the group-IV clathrates. Recent studies on this ice clathrates could show that the low glass-like thermal conductivity of these materials can be attributed to low frequency rattling modes of the guest atoms or molecules, respectively [Tse2005]. If the group-IV clathrates showed similiar behaviour they would represent a novel candidate material for improved thermo-electric applications. The anew interest in group-IV clathrates gave rise to a wide spectrum of interesting and promising physical properties like superconductivity and hardness as well as optoelectrical and thermoelectric applications. As it was pointed out recently by San-Miguel [San-Miguel2005 (b)] , the understanding of the interaction of the guest atoms with the host lattice is a key to gain fundamental insight into the physical properties of the clathrates.

Focussing on the interacting electron system of the guest atoms and the host lattice this study presents a combined experimental and theoretical analysis on alkali-metal doped silicon clathrates with Compton scattering experiments at its center. Especially the interaction of the alkali-metal valence electrons with the host atoms of the clathrates is discussed controversially in literature, ranging from a neutral free atomic guest [Gryko1996, Pouchard2002] to a partially [Conesa 2004] or fully [Moriguchi2000, Tse2000, Moewes2002] ionized dopant.

Compton scattering is a unique tool to study ground state properties and Fermiology of electrons in a solid because the measured quantity in Compton scattering experiments is the projected momentum density of the electron system in its ground state. The correct interpretation of the Compton effect in 1923 by Arthur Holly Compton [Compton1923] is a milestone in the developement of quantum mechanics but played only a minor role as an experimental tool for analysing electronic properties of solids. In 1929 DuMond and collaborators were the first to explain the shape of a Compton profile of beryllium theoretically within the Fermi-Dirac statistics [DuMond1929]. Although a couple of studies concerning the relation of Compton profiles and the electron momentum densities have been performed in the 1930s [DuMond1933, Kappeler1936], it was only after 25 years with the developement of a new generation of photon detectors that the technique was reestablished by Weiss and others in the mid 1960s (see for example [Cooper2004] and references therein). With the advent of 3rd generation synchrotron radiation sources along with the further improvement of the detector technology, Compton scattering is now an established tool for a variety of systems ranging from fundamental research on simple metals, high Z materials up to measuring magnetic properties using polarized incident photons.

In the present study the valence contribution to the Compton profile of the guest atoms in the clathrates is digested by comparing the alkali-metal doped silicon clathrates with an adequate reference material. Especially the charge transfer of the alkali-metal guests to the silicon host as well as the state of hybridization are discussed. An overview of the structure of the thesis along with a short description of the content of each chapter is given below.

In **chapter 1**, the theoretical background for Compton scattering experiments is presented. The directional Compton profile is derived explicitly from the double differential scattering cross section with the use of the so called Impulse Approximation. At the end of the chapter relativistic corrections as well as limits of the Impulse Approximation are discussed. The chapter closes with a description of a free electron gas model of the momentum density.

Chapter 2 contains a brief introduction to the computational schemes used in this work starting with the Hartree-Fock approximation and is followed by a survey of the basics of Density Functional Theory.

Chapter 3 attends to the origin, the structure, the synthetization, and finally the physical properties of silicon clathrates.

Chapter 4 is dedicated to the experimental setup and a detailed description of the data analysis. The chapter closes with first comparisons of the experimental data with theoretical predictions and literature.

In **chapter 5** the experimentally obtained spectra are presented and compared with the theory. Both, theoretical and experimental results are discussed in terms of charge transfer.

The concluding **chapter 6** summarizes the thesis and gives an outlook for further studies. It is followed by the appendices and the acknowledgements.

Chapter 1

Theory of Compton scattering

In this chapter the theoretical basics of Compton scattering are discussed. Starting with the inelastic scattering process in general (section 1.1), the non-relativistic double differential scattering cross-section (DDSCS) and the so-called dynamic structure factor are derived (sections 1.2 and 1.3). A review on the theory of Compton scattering is given at the end of the chapter including the Impulse Approximation (1.4), the directional Compton profile (1.5), limitations of the Impulse Approximation (1.7), and finally relativistic corrections (1.8).

1.1 Inelastic x-ray scattering

The geometry of an inelastic x-ray scattering experiment is depicted in figure (1.1). A photon with energy $\hbar\omega_1$, wave vector $\vec{k}_1$ and polarization vector $\vec{\epsilon}_1$ interacts with a

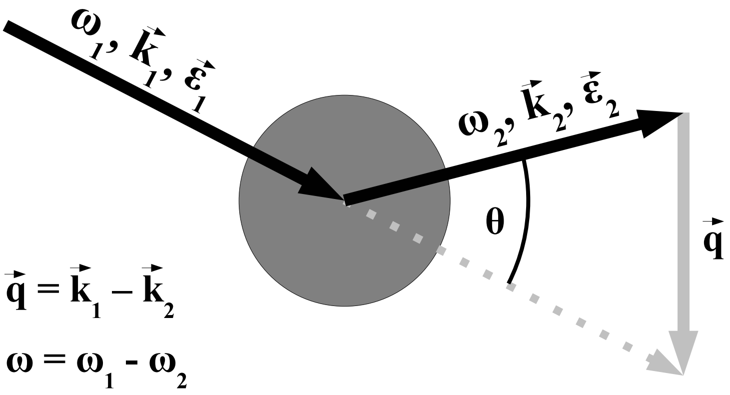

Figure 1.1: *Inelastic x-ray scattering process with energy transfer $\hbar\omega$ and momentum transfer $\hbar\vec{q}$.*

given system and is scattered at an angle θ. The scattered photon has an energy $\hbar\omega_2$, a wave vector $\vec{k}_2$ and a polarization vector $\vec{\epsilon}_2$. The transferred energy to the system is $\hbar\omega = \hbar\omega_1 - \hbar\omega_2$, the transferred momentum $\hbar\vec{q} = \hbar\left(\vec{k}_1 - \vec{k}_2\right)$. The modulus of $\vec{q}$ is given by

$$|\vec{q}| = \sqrt{\omega_1^2 + \omega_2^2 - 2 \cdot \omega_1 \cdot \omega_2 \cdot \cos\theta}. \tag{1.1}$$

If the transferred energy $\hbar\omega$ is small compared to the incident energy $\hbar\omega_1$, equation (1.1) reduces to

$$|\vec{q}| \approx 2\vec{k}_1 \sin\frac{\theta}{2} \quad . \tag{1.2}$$

The aim of an inelastic x-ray scattering experiment is to measure the double differential scattering cross section $(d^2\sigma/d\Omega d\omega_2)$, which is a function of a given fraction of the solid angle $d\Omega$ and the energy interval $\hbar d\omega_2$ of the scattered photons. The incident energy $\hbar\omega_1$ and the scattering angle θ will be fixed during an experiment and $d^2\sigma/d\Omega d\omega_2$ is measured as a function of $\vec{q}$ and ω. For the derivation of the DDSCS as well as in chapter 2 natural units, where $\hbar = c = 1$, are used.

1.2 The non-relativistic double differential scattering cross-section

For deriving the DDSCS within the non-relativistic limit the interaction Hamiltonian is given by

$$H_{\text{em}} = \sum_j \frac{e^2}{2m}\,\vec{A}(\vec{r}_j)^2 - \sum_j \frac{e}{m}\,\vec{p}_j \cdot \vec{A}(\vec{r}_j) = H^{(1)}_{\text{em}} + H^{(2)}_{\text{em}} \ . \tag{1.3}$$

Here $\vec{p}_j$ is the momentum operator of the electron j and $\vec{A}(\vec{r}_j)$ the corresponding vector potential operator of the electromagnetic field at the position $\vec{r}_j$. Furthermore, e denotes the elementary charge of an electron and m is its rest mass. In the so-called 2nd quantization the vector potential operator $\vec{A}(\vec{r}_j)$ is developed in terms of photon creation $a^\dagger_\lambda$ and annihilation operators a_λ:

$$\vec{A}(\vec{r}_j) = \sum_{\lambda,\vec{k}} \sqrt{\frac{2\pi}{V_0\omega_{\vec{k}}}}\left(\vec{\epsilon}\,(\lambda,\vec{k})\ a(\lambda,\vec{k})\ e^{i\vec{k}\cdot\vec{r}_j} + \vec{\epsilon}^{\,*}(\lambda,\vec{k})\ a^\dagger(\lambda,\vec{k})\ e^{-i\vec{k}\cdot\vec{r}_j}\right) . \tag{1.4}$$

Where $\vec{\epsilon}_\lambda$ is the polarization unit vector, $\vec{k}_\lambda$ is the wave vector of the electromagnetic plane wave, and the index λ counts the two possible directions of the polarization. Finally $\vec{A}(\vec{r}_j)$ is normalized to a given volume V_0.

In equation (1.3), the term $\vec{A}(\vec{r}_j)^2$ describes each - the creation and the annihilation of a photon - and therefore elastic as well as inelastic scattering processes. In first order perturbation theory the term $\vec{p}_j \cdot \vec{A}(\vec{r}_j)$ describes either the creation or the annihilation of a photon and thus will not contribute to the DDSCS. To calculate the DDSCS with equations (1.3) and (1.4) $H_{em}^{(1)}$ contributes in first, $H_{em}^{(2)}$ in second order perturbation theory. This leads to the Kramers-Heisenberg-equation [Kramers1925]:

$$\begin{aligned}
\frac{d^2\sigma}{d\Omega d\omega_2} &= r_0^2 \, \tfrac{\omega_2}{\omega_1} \, \textstyle\sum_{i,f} \Bigg| \left\langle f \middle| \sum_j e^{i\vec{q}\cdot\vec{r}_j} \middle| i \right\rangle \cdot \; (\vec{\epsilon}_1 \cdot \vec{\epsilon}_2) && \text{[a]} \\
&- \tfrac{1}{m} \textstyle\sum_n \left\{ \frac{\left\langle f \middle| \vec{\epsilon}_2 \cdot \sum_j \vec{p}_j e^{-i\vec{k}_2\cdot\vec{r}_j} \middle| n \right\rangle \left\langle n \middle| \vec{\epsilon}_1 \cdot \sum_j \vec{p}_j e^{i\vec{k}_1\cdot\vec{r}_j} \middle| i \right\rangle}{E_n - E_i - \omega_1 + \frac{1}{2}\, i\Gamma_n} \right. && \text{[b]} \\
&+ \left. \frac{\left\langle f \middle| \vec{\epsilon}_1 \cdot \sum_j \vec{p}_j e^{i\vec{k}_1\cdot\vec{r}_j} \middle| n \right\rangle \left\langle n \middle| \vec{\epsilon}_2 \cdot \sum_j \vec{p}_j e^{-i\vec{k}_2\cdot\vec{r}_j} \middle| i \right\rangle}{E_n - E_i - \omega_2} \right\} \Bigg|^2 && \text{[c]} \\
&\times \delta\left(E_f - E_i - \omega\right). && \text{[d]}
\end{aligned} \tag{1.5}$$

m: electron mass r_0: classical electron radius

$|i\rangle$: initial state $|f\rangle$: final state $|n\rangle$: intermediate state

Here, E_i, E_n, and E_f are the energies of the initial, the intermediate and the final states of the electrons, respectively. The summations are over all initial and final states ($|i\rangle\,|f\rangle$), all intermediate states ($|n\rangle$) and all j electrons of the system. Term [a] in equation (1.5) describes the scattering of a photon on a given system, with a direct transition from an initial state $|i\rangle$ to a final state $|f\rangle$. Here the cross section is a function of the final and the initial states as well as the transferred energy and momentum to the system. The delta function ensures that energy is conserved (term [d]). The fractions [b] and [c] of equation (1.5) are suppressed by a factor of $1/m$ compared with the term [a], so that the latter will dominate the cross section as long as the incident energy of the photons is far away from the binding energies of the electron system.

For ω_1 close to the binding energies of the tested system term [b] will show resonant behaviour. Here the photon is absorbed and the system excites into an intermediate

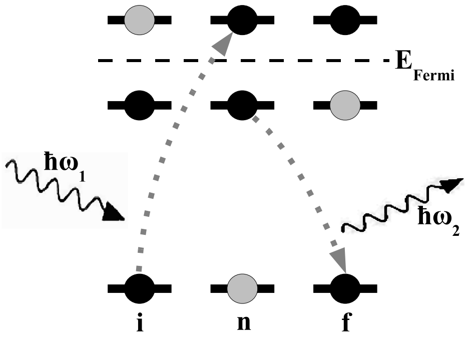

Figure 1.2: *Resonant inelastic x-ray scattering process: An incoming photon excites a bound core electron into an unoccupied state above the Fermi level. Finally a valence electron fills the core-hole by emitting a photon.*

state $|n\rangle$ with a finite lifetime $\tau_n = \Gamma_n^{-1}$. After emitting a photon it will reach a final state $|f\rangle$. The general course of the resonant inelastic x-ray scattering process (RIXS) is illustrated in figure (1.2). In case of Compton scattering experiments the energies of the incident photons are far above the binding energies of the system so that the focus will be on the non-resonant term [a] of equation (1.5). As the terms [b] and [c] can be neglected the cross section becomes

$$\frac{d^2\sigma}{d\Omega d\omega_2} = r_0^2 \, (\vec{\epsilon}_1 \cdot \vec{\epsilon}_2)^2 \, \left(\frac{\omega_2}{\omega_1}\right) \sum_{i,f} \left| \left\langle f \middle| \sum_j e^{i\vec{q}\cdot\vec{r}_j} \middle| i \right\rangle \right|^2 \, \delta\left(E_f - E_i - \omega\right) \, . \tag{1.6}$$

1.3 The dynamic structure factor

The non-relativistic double differential scattering cross section can be separated into two terms:

$$\frac{d^2\sigma}{d\Omega d\omega_2} = \left(\frac{d\sigma}{d\Omega}\right)_{\mathrm{Th}} S\left(\vec{q}, \omega\right) . \tag{1.7}$$

The first term is the Thomson cross section for elastically scattered photons on electrons

$$\left(\frac{d\sigma}{d\Omega}\right)_{\mathrm{Th}} = r_0^2 \, (\vec{\epsilon}_1 \cdot \vec{\epsilon}_2)^2 \, \left(\frac{\omega_2}{\omega_1}\right) , \tag{1.8}$$

the second term denotes the so-called dynamic structure factor $S\left(\vec{q}, \omega\right)$

$$S\left(\vec{q}, \omega\right) = \sum_{i,f} \left| \left\langle f \middle| \sum_j e^{i\vec{q}\cdot\vec{r}_j} \middle| i \right\rangle \right|^2 \, \delta\left(E_f - E_i - \omega\right) . \tag{1.9}$$

It describes the dynamic response of the electronic system to an external perturbance.

For understanding the different processes described by $S(\vec{q}, \omega)$ the ratio between the modulus of the momentum transfer q and the characteristic distances of the system and the comparison of ω with characteristic frequencies of the system ω_c have to be considered. Here, the characteristic distances are the interparticle distances r_c (e.g. the expectation value of the electron nucleus distance). As long as $q \cdot r_\mathrm{c} \ll 1$ long ranging correlations of the electronic system will dominate and the collective properties of the system are probed as a whole. If on the contrary $q \cdot r_\mathrm{c} \gg 1$, the response of the system is limited to short-ranged correlations.

Neglecting the phonon excitations the non-resonant inelastic x-ray scattering process can be divided into three regimes:

1. **Valence electron excitations:** Plasmons and particle-hole pair excitations can be observed as long as the energy transfer ω is close to the plasmon frequency ω_P and $q \cdot r_\mathrm{c} \approx 1$ [Schülke1991]. In this work these excitations are playing a minor role.

2. **Non-resonant x-ray Raman scattering:** If the transferred energy ω is close to binding energies ω_B of the system the DDSCS yields similar results as in absorption spectroscopy. If in addition $q \cdot r_\mathrm{c} > 1$, multipole transitions become possible. A more detailed discussion of non-resonant x-ray Raman scattering is given in section (4.4.1).

3. **Compton scattering:** In the Compton regime, the energy transfer is large compared to the binding energies of the electrons, $\omega \gg \omega_\mathrm{B}$ and $q \cdot r_\mathrm{c} \gg 1$. If both conditions are fullfilled, the DDSCS can be discussed in the limit of the Impulse Approximation, which is done in detail below.

1.4 Impulse Approximation

The essence of the Impulse Approximation is to assume that the scattering process itself is so fast, that the electron system has no time to rearrange itself and the interaction is taking place under a constant potential. In consequence the transferred energy $\omega \gg \omega_{\mathrm{B}}$ and momentum $q \cdot r_{\mathrm{c}} \gg 1$ are large enough to consider the excited electron as a free electron. Keeping the above in mind, one has to go back to equation (1.6). Using the δ-function in its Fourier representation

$$\delta\big(E_f - E_i - \omega\big) = \delta\big(\omega + (E_i - E_f)\big) = \frac{1}{2\pi}\int dt\, e^{i\big(\omega+(E_i-E_f)\big)t} \tag{1.10}$$

leads to

$$\begin{aligned}\frac{d^2\sigma}{d\Omega d\omega_2} = \left(\frac{d\sigma}{d\Omega}\right)_{\mathrm{Th}} \frac{1}{2\pi}\int dt\; e^{-i\omega t}\sum_{i,f}\Big\langle i\Big|\sum_{j\prime} e^{-i\vec{q}\cdot\vec{r}_{j\prime}}\Big|f\Big\rangle \\ \times\Big\langle f\Big|e^{iE_f t}\sum_{j} e^{i\vec{q}\cdot\vec{r}_j}\; e^{-iE_i t}\Big|i\Big\rangle \quad .\end{aligned} \tag{1.11}$$

As E_i and E_f are eigenvalues of the Hamilton operator H of the electron system, equation (1.11) can be written as

$$\frac{d^2\sigma}{d\Omega d\omega_2} = \left(\frac{d\sigma}{d\Omega}\right)_{\mathrm{Th}} \frac{1}{2\pi}\int dt\; e^{-i\omega t}\Big\langle i\Big|\sum_{j\prime} e^{-i\vec{q}\cdot\vec{r}_{j\prime}}\; e^{iHt}\;\sum_{j} e^{i\vec{q}\cdot\vec{r}_j}\; e^{-iHt}\Big|i\Big\rangle \quad , \tag{1.12}$$

where for the sake of simplicity the sum over all initial states is neglected. Dividing the Hamiltonian into a kinematic term H_0 and a constant potential V its exponential can now be expanded:

$$e^{iHt} \approx e^{iH_0 t}\; e^{iVt}\; e^{-\frac{1}{2}[H_0,V]t^2} \; . \tag{1.13}$$

In the Compton regime

$$\frac{1}{2}\langle[H_0, V]\rangle \approx E_{\mathrm{B}}^2 \ll \omega^2 \; , \tag{1.14}$$

and

$$e^{-\frac{1}{2}[H_0,V]t^2} \simeq 1 \tag{1.15}$$

for $t \gg 1/\omega$. Therefore, equation (1.12) simplifies to

$$\frac{d^2\sigma}{d\Omega d\omega_2} = \left(\frac{d\sigma}{d\Omega}\right)_{\text{Th}} \frac{1}{2\pi} \int dt\; e^{-i\omega t} \Big\langle i \Big| \sum_{j\prime} e^{-i\vec{q}\cdot\vec{r}_{j\prime}}\; e^{iH_0 t}\; \sum_{j} e^{i\vec{q}\cdot\vec{r}_j}\; e^{-iH_0 t} \Big| i \Big\rangle \ . \tag{1.16}$$

Note, that the potential V commutes with the electron position $\vec{r}_j$ and thus cancels out. A detailed analysis of equation (1.16) is given in [LOEWDIN1955]. In the following the discussion is reduced to a one electron atom. In this case the summations over j and $j\,'$ can be left out:

$$\frac{d^2\sigma}{d\Omega d\omega_2} = \left(\frac{d\sigma}{d\Omega}\right)_{\text{Th}} \frac{1}{2\pi} \int dt\; e^{-i\omega t} \Big\langle i \Big| e^{-i\vec{q}\cdot\vec{r}}\; e^{iH_0 t}\; e^{i\vec{q}\cdot\vec{r}}\; e^{-iH_0 t} \Big| i \Big\rangle \ . \tag{1.17}$$

Now a complete set $\sum_{|\vec{p}\rangle} |\vec{p}\rangle\langle\vec{p}|$ of eigenfunctions $|\vec{p}\rangle$ of H_0 is introduced with

$$e^{(iH_0 t)}|\vec{p}\rangle = e^{i\varepsilon(\vec{p})t}|\vec{p}\rangle \tag{1.18}$$

and

$$\varepsilon(\vec{p}) = \vec{p}^{\,2}/2m \ . \tag{1.19}$$

Performing the time integration in equation (1.17) will reintroduce a δ-function and one ends up with

$$\frac{d^2\sigma}{d\Omega d\omega_2} = \left(\frac{d\sigma}{d\Omega}\right)_{\text{Th}} \sum_{\vec{p}} \left| \Big\langle i \Big| e^{-i\vec{q}\cdot\vec{r}} \Big| \vec{p} \Big\rangle \right|^2 \;\delta\left[\varepsilon(\vec{p}) - \varepsilon(\vec{p}-\vec{q}) - \omega\right] \ . \tag{1.20}$$

After redefining $\vec{p}$ by

$$\vec{p}\,' \equiv \vec{p} - \vec{q} \tag{1.21}$$

and again renaming $\vec{p}\,'$ as $\vec{p}$, the system changes from a discrete to a continuous system and the summation over $\vec{p}$ transforms to an integration. According to equations (1.19) and (1.21)

$$\varepsilon(\vec{p}) - \varepsilon(\vec{p}-\vec{q}) = \varepsilon(\vec{p}\,'+\vec{q}) - \varepsilon(\vec{p}\,') = q^2/2m + \vec{p}\cdot\vec{q}/m \tag{1.22}$$

and finally the DDSCS changes to

$$\frac{d^2\sigma}{d\Omega d\omega_2} = \left(\frac{d\sigma}{d\Omega}\right)_{\text{Th}} \frac{1}{(2\pi)^3} \int \left|\left\langle i \middle| \vec{p} \right\rangle\right|^2 \delta\left[q^2/2m + \vec{p}\cdot\vec{q}/m - \omega\right] \, d\vec{p} \, . \tag{1.23}$$

Here $q^2/2m$ is the non-relativistic Compton shift for an electron at rest and $\vec{p}\cdot\vec{q}/m$ gives the Doppler shift of an electron with a finite momentum $\vec{p}$ in its initial state.

The integrand of equation (1.23) represents the momentum space density of the scattering system in the ground state and thus gives the probability of finding an electron with a given momentum $\vec{p}$:

$$\begin{aligned} \rho\left(\vec{p}\right) &= \frac{1}{(2\pi)^3} \left|\left\langle i \middle| \vec{p} \right\rangle\right|^2 = \left|\chi(\vec{p})\right|^2 \\ &= \frac{1}{(2\pi)^3} \left|\int \psi(\vec{r}) e^{-i\vec{p}\cdot\vec{r}} d\vec{r}\right|^2 \, , \end{aligned} \tag{1.24}$$

with $\psi(\vec{r})$ representing the wavefunction of the electrons in real space and $\chi(\vec{p})$ the corresponding wavefunction in momentum space. If in addition $\vec{q}$ is pointing into z-direction, equation (1.23) becomes

$$\frac{d^2\sigma}{d\Omega d\omega_2} = \left(\frac{d\sigma}{d\Omega}\right)_{\text{Th}} \frac{m}{q} \int\int \rho(p_x, p_y, p_z) \, dp_x dp_y \tag{1.25}$$

with

$$\begin{aligned} p_z &= \frac{m}{q}\omega - \frac{q}{2} \\ &\approx m \frac{\omega_1 - \omega_2 - \frac{\omega_1\omega_2}{m}(1-\cos\theta)}{\sqrt{\omega_1^2 + \omega_2^2 - 2\omega_1\omega_2\cos\theta}} \, . \end{aligned} \tag{1.26}$$

1.5 The Compton profile

The integral in equation (1.25) defines the so-called (directional) Compton profile:

$$\frac{d^2\sigma}{d\Omega d\omega_2} = \frac{r_0^2}{2}\frac{\omega_2}{\omega_1}\frac{m}{q} J(p_z) \tag{1.27}$$

with

$$J\left(p_z\right) = \int\int \rho(p_x, p_y, p_z) \, dp_x dp_y \, . \tag{1.28}$$

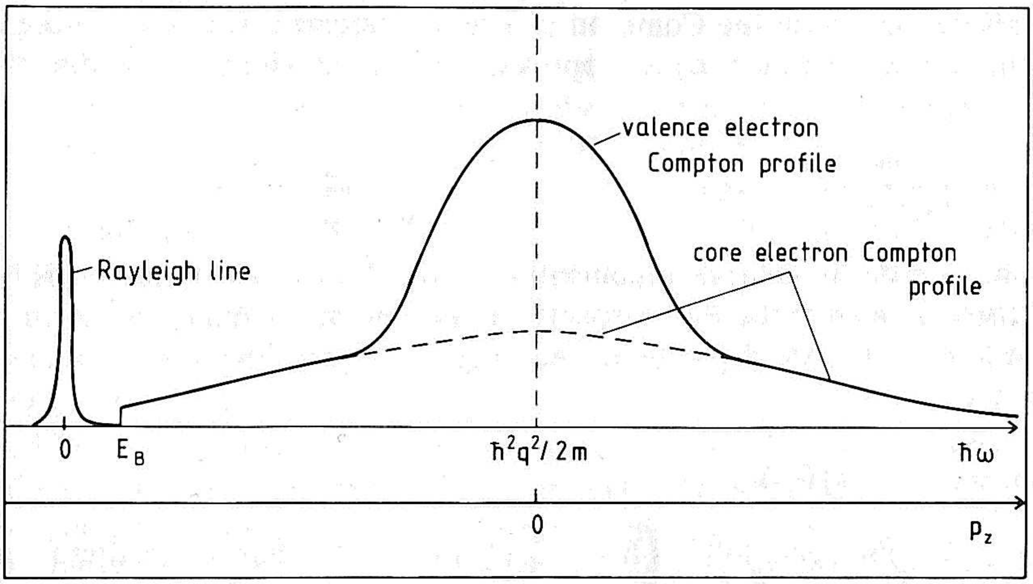

Figure 1.3: *Schematic overview of a Compton profile together with the Rayleigh line of the quasi elastically scattered photons both at energy loss scale and at the projected momentum transfer* p_z *scale* [SCHÜLKE1991].

Equation (1.28) is the projection of the momentum density $\rho(\vec{p})$ over a plane perpendicular to the scattering vector $\vec{q}$. A schematic overview of a Compton profile is depicted in figure (1.3). The x-axis is given both on a p_z and an energy loss scale. At zero energy transfer the Rayleigh line of the quasi elastically scattered photons is located. The typical electron binding energies E_B of a given system define the onset of the Compton profile of the core electrons. The Compton profile can be separated into a core electron contribution (core Compton profile) and a valence electron contribution (valence Compton profile). As the core electrons are tightly bound to the atoms in real space their momentum is widely smeared in momentum space, whereas the contribution of the valence electrons is well concentrated around $p_z = 0$.

All Compton profiles can be absolutely scaled to the number of electrons per atom via the so-called f-sum rule [SCHÜLKE1991]:

$$\int J(p_z)dp_z = N\,. \tag{1.29}$$

1.6 The free electron gas model

A most simple model of a valence electron system is a system of free electrons at zero temperature. As a consequence Pauli's principle leads to a momentum distribution of the electrons as follows:

$$\begin{aligned} &\rho(p) = 1 \quad \text{for } p \leq p_\mathrm{F} \quad (p_\mathrm{F} = \text{Fermi momentum}) \\ &\rho(p) = 0 \quad \text{for } p < p_\mathrm{F}\,. \end{aligned} \tag{1.30}$$

All states up to the Fermi momentum p_F are occupied, whereas all states above p_F are empty resulting in an inverted parabola for the valence Compton profile with zero value above p_F and below $-p_\mathrm{F}$, the so-called Fermi break:

$$J(p_z) = \pi(p_\mathrm{F}^2 - p_z^2) \tag{1.31}$$

1.6.1 Electron-electron correlation

To model electron-electron interactions one can start by assuming a homogeneous interacting electron gas. This is achieved by adding a continuous function $\rho^c(p)$ to a Heaviside function with stepsize z_F at the Fermi momentum:

$$\rho(p) = z_F \theta(p_F - p) + \rho^c(p)\,. \tag{1.32}$$

z_F is called the renormalization constant [SCHÜLKE2004]. Now the valence electrons occupy states above the Fermi level and the valence Compton profile contributes for $p > p_\mathrm{F}$ also. The Fermi break is diminished, which is characterized by the value of z_F. The resulting valence Compton profiles together with the corresponding electron momentum densities are depicted in figure (1.4).

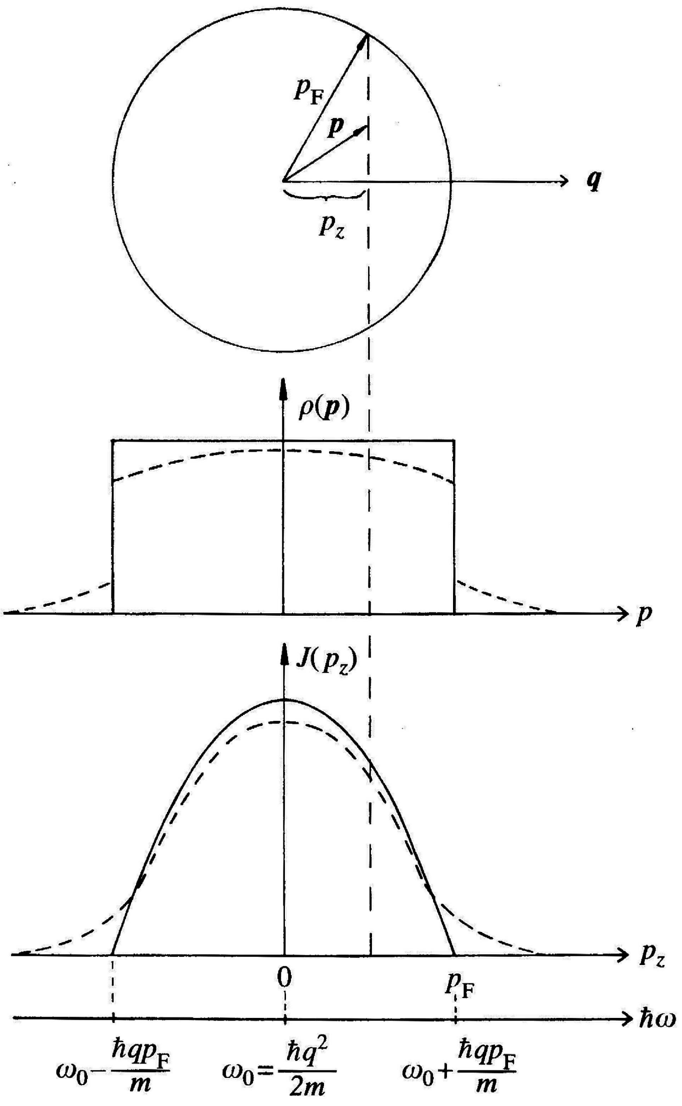

Figure 1.4: *For a free electron gas the Fermi surface is a sphere with radius* p_F *- the Fermi-momentum. The Compton profile of the valence electrons is calculated by integrating over slices perpendicular to the momentum transfer* $\vec{q}$*. The middle picture shows the momentum space density of a free electron gas at zero temperature (solid line) as well as for an interacting electron gas (dashed line). Below the corresponding valence Compton profiles are depicted* [SCHÜLKE2004].

1.7 The asymmetry of Compton profiles and limitations of the Impulse Approximation

By definition of equation (1.28), the Compton profile should be a symmetric function of p_z with its maximum at $\mathrm{p}_z = 0$. In fact, measured Compton profiles show an intrinsic asymmetry, which can be attributed to the failure of the Impulse Approximation [Huotari2001]. First corrections were estimated by Eisenberger and Platzman [Eisenberger1970] and are of the order of $(E_\mathrm{B}/E_\mathrm{R})^2$, where E_B is the binding energy of the initial electron state and $E_\mathrm{R} = q^2/2m$ is the recoil energy. Therefore, the asymmetry of the core electron Compton profile is of particular interest. Holm and Ribberfors (HR) [Holm1989] calculated a first order correction of the series in equation (1.13). Since then, other approaches have been made including quasi-self-consistent field (QSCF) theory [?]. Sternemann *et al.* [Sternemann2000] studied the asymmetry of valence Compton profiles in lithium for low incident photon energies of 8 keV to 10 keV. They could show, that the valence Compton profile asymmetries are caused by the interactions of the scattered electrons with the created electron holes. In figure (1.5) experimentally obtained asymmetries of sodium and beryllium core electron Compton profiles are compared with HR and QSCF calcula-

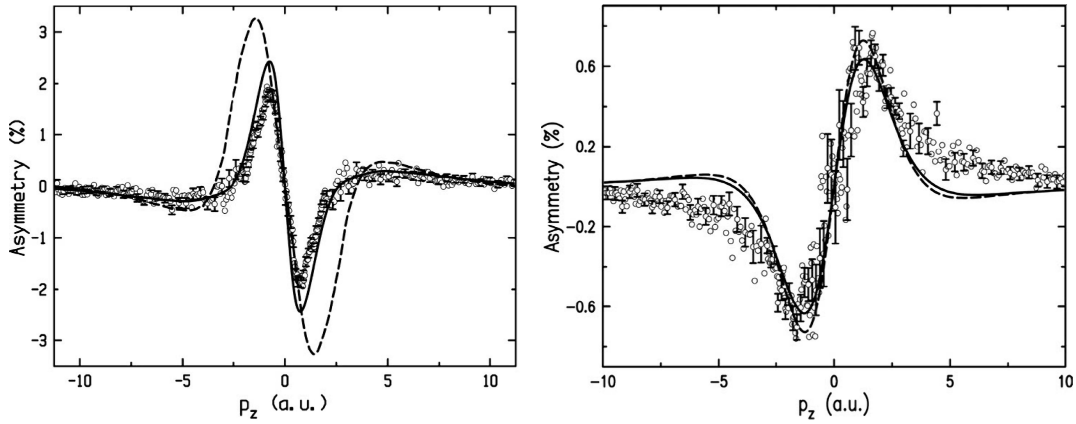

(a) (b)

Figure 1.5: *Intrinsic asymmetries of the core electron Compton profiles of sodium (a) and beryllium (b). The experimental data (open circles) is compared with the HR correction (dashed line) and QSCF theory (solid line)* [Huotari2001]. *For beryllium both methods provide similar results, whereas for sodium only the QSCF calculations are able to represent the experimental data.*

tions [Huotari2001]. Here, the asymmetry of the core electron Compton profiles is given as a percentage relative to the value of the Compton profile at $p_z = 0$

$$\Delta J(p_z) = \frac{J(p_z) - J(-p_z)}{J(0)} \ , \tag{1.33}$$

with $J(0) = 3.7$ for sodium and 1.8 for beryllium. It is important to note, that the asymmetries are element specific. Additionally, as the sign of $\Delta J(p_z)$ is different for sodium and beryllium, an experimental origin of the asymmetries can be excluded. Furthermore the authors note that by varying the incident energy ω_1, the asymmetry is not changing in shape but is magnified for lower ω_1.

Although both calculations do give a good approximation of the asymmetries, the results are not suited to directly subtract a calculated spectrum from the experimental data.

1.8 Relativistic effects

To enable Compton scattering experiments on elements with high atomic number Z the energy of the incident x-rays has increased from about 10 keV for the first Compton scattering experiments in the 1930s to about 100 keV, starting in the early 1970s. Here, the recoil electron can no longer be treated as non-relativistic. Consequently the DDSCS has to be corrected for relativistic effects. Following Ribberfors [Ribberfors1975], the strict separation of the dynamic response of the system and the coupling of the photons to the electrons can be maintained by utilizing an approximate relativistic treatment resulting in

$$\frac{d^2\sigma}{d\Omega d\omega_2} = \frac{r_0^2}{2} \, \frac{\omega_2}{\omega_1} \, X(p_z) \, \frac{m}{q} J(p_z) \ . \tag{1.34}$$

Ribberfors heuristic approach is valid for all scattering angles and even anisotropic momentum distributions. With a rigorous relativistic treatment its validity was proven later by Holm [Holm1988]. In the scope of this work linear polarized photons are used. The X-factor is then calculated by the sum over the two polarization states of the scattered photons to

$$X(p_z) = \frac{R}{R\,'} + \frac{R\,'}{R} - 2\sin^2\theta\cos^2\beta \ , \tag{1.35}$$

where β denotes the angle between the scattering plane and the polarization vector of the incident photons. The scattering angle θ and the factors R and $R\,'$ are given by

$$\begin{aligned} R &= \omega_1 \left(m - (\omega_1 - \omega_2 \cos\theta) \frac{p_z}{q} \right) \\ R\,' &= R - \omega_1 \omega_2 (1 - \cos\theta) \ . \end{aligned} \tag{1.36}$$

Chapter 2

Models for the theoretical treatment of Compton profiles

In this chapter the basic equations and ideas of the computational schemes for calculating the Compton profiles of the silicon clathrates are presented. As the Compton profile is obtained by the two dimensional integration of the Fourier transform of the electron density function (see chapter [1]), an accurate model of the electron system is required. In section (2.1) the important Hartree-Fock approximation is discussed briefly. It gives good results for the core electron contribution to the Compton profile. In section (2.2) a survey of the Density Functional Theory along with possible approximations for the electron density is given. Because the Density Functional Theory accounts for correlation and exchange effects of the electron-electron interactions, it provides a more accurate description especially for the valence electrons compared to the Hartree-Fock approximation.

2.1 The Hartree-Fock approximation

A more sophisticated approach then to postulate a free electron gas would be to start with the Schrödinger equation for an N-particle system with N counting all the electrons of the solid.

Following the Born-Oppenheimer approximation the nuclei have fixed positions $\vec{R}_k$:

$$H\Psi = [(T + V_{\text{ext}}) + U]\,\Psi \tag{2.1}$$

$$= \sum_{i=1}^{N} \left(-\frac{1}{2m}\nabla_i^2\Psi - Ze^2 \sum_k \frac{1}{\left|\vec{r}_i - \vec{R}_k\right|}\Psi \right) + \frac{1}{2}\sum_{i\neq j} \frac{e^2}{|\vec{r}_i - \vec{r}_j|}\Psi = E\Psi\,. \tag{2.2}$$

The first term represents the kinetic energy T of the electrons and the second term the static external potential V_{ext} of the fixed nuclei. The last term in equation (2.2) U describes the electron-electron interaction of the system. In a first step this interaction is generated by a smooth distribution of negative charge with charge density ρ [Ashcroft1976]. The resulting potential of an electron in such a field would be

$$U_{\text{H}} = -e \int d\vec{r}'\rho(\vec{r}')\frac{1}{|\vec{r} - \vec{r}'|} \tag{2.3}$$

and is often referred to as the Hartree potential U_{H}.

In a second step, the wave function Ψ is developed as a Slater determinant of one-electron wave functions to account for the Pauli principle. With the introduction of the spin states of the electrons σ this leads to the Hartree-Fock equations:

$$\epsilon_i\psi_i(\vec{r}) = \left(-\frac{1}{2m}\nabla^2 + V_{\text{ext}}(\vec{r})\right)\psi_i(\vec{r}) + \left(e^2\sum_j \int d\vec{r}'\frac{|\psi_j(\vec{r}')|^2}{|\vec{r} - \vec{r}'|}\right)\psi_i(\vec{r})$$

$$- e^2\sum_j \delta_{\sigma_i\sigma_j}\int d\vec{r}'\frac{\psi_j^*(\vec{r}')\,\psi_i(\vec{r}')}{|\vec{r} - \vec{r}'|}\psi_j(\vec{r}) \tag{2.4}$$

The last term of equation (2.4) is accounting for the effect, that electrons of like spin tend to avoid each other. The Hartree-Fock equations can be solved for example for a free-electron gas model. In this work the tabulated Compton profiles of free atoms calculated by Biggs, Mendelsohn, and Mann are used [Biggs1975]. Especially the core contribution to the overall Hartree-Fock Compton profile is a good approximation of the core Compton profile in a solid as long as the Impulse Approximation is valid [Cooper2004].

2.2 Density Functional Theory

An at least formally exact method of calculating ground state properties of many electron systems is given by the Density Functional Theory (DFT). Instead of solving equation (2.1) for the $3N$ dimensional wave function Ψ, the DFT reduces the problem to finding the minimum of the total energy functional of the system via the 3 dimensional ground state electron density $\rho(\vec{r})$. It is based on two theorems of Hohenberg and Kohn published in 1964 [HOHENBERG1964]:

1. The external potential V_{ext} is determined within a trivial additive constant by the electron density $\rho(\vec{r})$ of a non-degenerate system. Therefore, the total energy of the electron system is a functional of $\rho(\vec{r})$: $E_{\text{tot}} = E_{\text{tot}}[\rho(\vec{r})]$.
2. For any given non-negative trial density $\rho(\vec{r})$ that integrates to the correct number of electrons N the true ground state energy E^0_{tot} satisfies the relation:

$$E^0_{tot} = E[\rho^0(\vec{r})] \leq E[\rho(\vec{r})] \,. \tag{2.5}$$

Therefore, the total energy functional $E_{\text{tot}}[\rho(\vec{r})]$ follows a variational principle with its minimum being the total ground state energy E^0_{tot} at the exact ground state electron density $\rho^0(\vec{r})$. It is expressed as

$$E_{\text{tot}}[\rho(\vec{r})] = F[\rho(\vec{r})] + \int \rho(\vec{r})\, v_{\text{ext}}(\vec{r})\, d\vec{r} \,. \tag{2.6}$$

$F[\rho(\vec{r})]$ does not depend on the external potential $v_{\text{ext}}(\vec{r})$ and is a universal functional of $\rho(\vec{r})$ in the sense that it is the same for all systems described by equation (2.1). Although powerful in their statements the two theorems do not provide a way to calculate the total energy as the functional $F[\rho(\vec{r})] = T[\rho(\vec{r})] + U[\rho(\vec{r})]$ is unknown.

2.2.1 The Khon-Sham equations

In 1965 Khon and Sham [KOHN1965] published a concept, which solves equation (2.6) by introducing a system of non-interacting electrons within an effective external potential $v_{\text{eff}}(\vec{r})$. It is constructed in such a way, that the electron density of the non-interacting system equals that of the interacting system of interest. Then, the total energy functional can be written as

$$E_{\text{KS}} = T_{\text{KS}} + \int \rho(\vec{r})\, v_{\text{eff}}(\vec{r})\, d\vec{r} \,. \tag{2.7}$$

The kinetic energy functional $T_{\text{KS}}[(\vec{r})]$ and the electron density $\rho(\vec{r})$ of this system are expressed using one-particle wavefunctions, the so-called Kohn-Sham orbitals:

$$\rho\left(\vec{r}\right) = n\sum_{i}^{n_{\mathrm{occ}}} \left|\varphi_i\left(\vec{r}\right)\right|^2 \text{ and } T_{\mathrm{KS}}[\rho\left(\vec{r}\right)] = \sum_{i}^{n_{\mathrm{occ}}} \int \varphi_i^*\left(\vec{r}\right)\left(-\frac{1}{2m}\nabla^2\right)\varphi_i\left(\vec{r}\right)d\vec{r}\,. \tag{2.8}$$

The Kohn-Sham orbitals are constructed in such a way that they will follow the Pauli principle: $\Psi_{\mathrm{KS}} = \frac{1}{\sqrt{N!}}\, det\, [\varphi_i\left(\vec{r}_i\right)]$ and the summations are over the lowest occupied states n_{occ} of the system with i denoting spatial and spin quantum numbers. Applying the variational principle to equation (2.7) leads to the Kohn-Sham equations

$$\left[-\frac{1}{2m}\nabla^2 + v_{\mathrm{eff}}\left(\vec{r}\right) - \mu\right]\varphi_i\left(\vec{r}\right) = \epsilon_i\,\varphi_i\left(\vec{r}\right)\,. \tag{2.9}$$

Here μ and ϵ_i represent the Lagrange parameters guaranteeing charge conservation and orthonormality of the Khon-Sham orbitals. To solve the equations (2.9) one still has to find an expression for the effective potential v_{eff}. Therefore, one has to go back to equation (2.6) and divide the functional $F[\rho\left(\vec{r}\right)]$ into three parts:

$$F[\rho\left(\vec{r}\right)] = T_{\mathrm{KS}}[\rho\left(\vec{r}\right)] + E_{\mathrm{H}}[\rho\left(\vec{r}\right)] + E_{\mathrm{xc}}[\rho\left(\vec{r}\right)]\,, \tag{2.10}$$

with

$$E_{\mathrm{H}}[\rho\left(\vec{r}\right)] = \frac{1}{2}\int \frac{\rho\left(\vec{r}\right)\rho\left(\vec{r}'\right)}{\left|\vec{r}-\vec{r}'\right|}d\vec{r}d\vec{r}'\,, \tag{2.11}$$

the Hartree energy of the electrons and

$$E_{\mathrm{xc}}[\rho\left(\vec{r}\right)] = T[\rho\left(\vec{r}\right)] - T_{\mathrm{KS}}[\rho\left(\vec{r}\right)] + U[\rho\left(\vec{r}\right)] - E_{\mathrm{H}}[\rho\left(\vec{r}\right)]\,, \tag{2.12}$$

the exchange-correlation energy functional. $T[\rho\left(\vec{r}\right)]$ and $U[\rho\left(\vec{r}\right)]$ are representing the exact kinetic energy and the electron-electron interaction, respectively. The variational principle applied to equation (2.6) together with equation (2.10) gives

$$\frac{\delta T_{\mathrm{KS}}[\rho\left(\vec{r}\right)]}{\delta\rho\left(\vec{r}\right)} + v_{\mathrm{ext}} + \int \frac{\rho\left(\vec{r}'\right)}{\left|\vec{r}-\vec{r}'\right|}d\vec{r}' + \frac{\delta E_{\mathrm{xc}}[\rho\left(\vec{r}\right)]}{\delta\rho\left(\vec{r}\right)} - \mu = 0\,. \tag{2.13}$$

With an effective potential

$$v_{\mathrm{eff}} = v_{\mathrm{ext}} + \int \frac{\rho\left(\vec{r}'\right)}{\left|\vec{r}-\vec{r}'\right|}d\vec{r}' + v_{\mathrm{xc}} \tag{2.14}$$

and

$$v_{\mathrm{xc}} = \frac{\delta E_{\mathrm{xc}}[\rho(\vec{r})]}{\delta \rho(\vec{r})}, \tag{2.15}$$

equation (2.13) would lead to a formally identical equation (2.9). Thus, the Kohn-Sham equations (2.8) and (2.9) together with equation (2.14) define a set of equations, which can be solved self-consistently.

2.2.2 Approximations for the exchange-correlation functional

Although being exact in principle, the exchange-correlation functional $E_{\mathrm{xc}}[\rho(\vec{r})]$ is unknown and has to be approximated. However, the achievement of Kohn and Sham is that they have minimized the unknown contribution to the total energy. In the past decades many approximations for E_{xc} have been found with remarkably good results. The simplest approximation is called the Local Density Approximation (LDA). It consists of approximating locally the true exchange-correlation energy of a system by the exchange-correlation energy $\epsilon_{\mathrm{xc}}^{\mathrm{LDA}}$ associated with a homogeneous electron gas of the same density:

$$E_{\mathrm{xc}}^{\mathrm{LDA}}[\rho(\vec{r})] = \int \rho(\vec{r})\, \epsilon_{\mathrm{xc}}^{\mathrm{LDA}} d\vec{r}. \tag{2.16}$$

The LDA was first proposed by Hohenberg and Khon in their original publication in 1964 [HOHENBERG1964]. Despite their skepticism it gives good results for many applications. For strongly inhomogeneous systems the Generalized Gradient Approximation (GGA) improves the results of the DFT calculations significantly by introducing a gradient of the electron density:

$$E_{\mathrm{xc}}^{\mathrm{GGA}}[\rho(\vec{r})] = \int \rho(\vec{r})\, \epsilon_{\mathrm{xc}}^{\mathrm{LDA}} f_{\mathrm{xc}}[\rho(\vec{r}), \nabla \rho(\vec{r})] d\vec{r}. \tag{2.17}$$

In contrast to the LDA the exact form of the functional $f_{\mathrm{xc}}[\rho(\vec{r}), \nabla\rho(\vec{r})]$ is not unique. Useful representations of f_{xc} are given by Perdew and Wang [PERDEW1992] or Becke [BECKE1988].

Chapter 3

Silicon clathrates

Silicon clathrates are cage-like covalently bond materials. After their synthetization and characterization [Cros1965, Kasper1965, Cros1970, Cros1971] the interest in these compounds has recently grown in numerous fields of experimental and theoretical research due to their manifold physical properties (section 3.3). In section (3.1) the most common structure I and structure II clathrates are described and their synthesis is detailed in section (3.2).

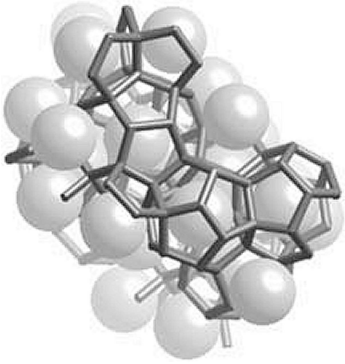

Figure 3.1: *Structure of alkali-metal doped silicon clathrates* [Univ. of Liege 2006].

3.1 The structure of clathrates

Nine different structures have been reported for silicon and germanium clathrates [Mudryk2002]. But the body of semiconductor clathrates can be classified into two cubic structures, which are isostructural to the hydrogen bonded clathrate hydrates called structure I and structure II, respectively [Sloan1998]. Semiconductor clathrates are inclusion compounds with the elements silicon, germanium, tin and hypothetically carbon building up a fourfold coordinated, covalently bond host network of nano-sized cages. Because the host atoms belong to the fourth row of the table of elements they are often referred to as group-IV clathrates. They are stabilized by trapped guest atoms consisting of alkali, alkaline-earth or even halogen atoms. The general buildup of a clathrate structure is displayed in figure (3.1).

The grey spheres symbolize the guest atoms trapped in the silicon host cages represented by the dark gray bars (Si-Si bondings). The framework atoms are sp^3 hybridized with bond length and bonding angles only slightly differing from the diamond phase (see table 3.3) [Gryko2000, Kahn1997, Kasper1965]. They build up face sharing Si_{20}, Si_{24} and Si_{28} fullerene-like cages in which the guest atoms can be trapped and are residing mainly in the center of the polyhedra. However, in the large hexakaidecahedra (Si_{28}) of structure II [Tournus2004] and under high pressure [Tse2002, Kume2004] the atoms are moving away from the center position. In previous publications [Kasper1965, Cros1965, Cros1970, Cros1972] the guest atoms were thought of being essential for the stability of the clathrate structure. Recently, the empty-caged silicon clathrates of structure I and structure II were predicted of being metastable. Exemplarily, the total energy per atom calculated as a function of the reduced volume of Adams *et al.* and Menon *et al.* are depicted in figure (3.2) [Adams1994, Menon1997]. The graphs show, that the minima of the total energy are only 0.03 eV to 0.06 eV above the total energy of the diamond silicon phase and are in accordance to other publications [Demkov1994, Kahn1997, Moriguchi2000]. Compared to the β-tin phase of silicon with 0.27 eV per atom [Yin1982], the total energy difference is rather low and in 2000 pure Si_{136} compounds were synthesized succesfully [Gryko2000]. In fact, the empty-caged structure II clathrate turns out to be rather stable even under hightpressure of up to 10 GPa [San-Miguel1999, Ramachandran2000]. At

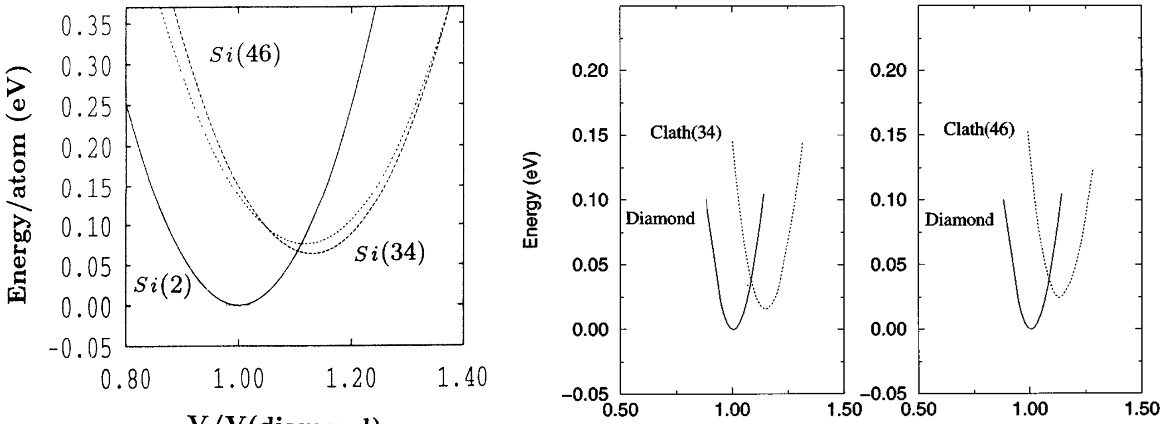

Figure 3.2: *The total energy of diamond phase silicon, Si_{34}, and Si_{46} as a function of the reduced volume $V/V_{diamond}$ as given in reference* [Adams1994] *(left) and* [Menon1997] *(right).*

even higher pressure, Si_{136} as well as Na_8Si_{46} transform into the β-tin phase of silicon. With growing size of the guest atom, Na, K, Rb, the behaviour of the doped clathrates changes dramatically. Here, two types of phase transitions can be observed. At the first transition a reversible isostructural volume collapse occurs with its onset depending strongly on the type of guest atom. The second transition takes place at even higher pressures and transforms the clathrates to an amorphous phase (table 3.1) [San-Miguel2002, Tse2002]. For K_8Si_{46} and Ba_8Si_{46}, an isostructural change of the electronic structure was observed at lower pressures of about 6 GPa [San-Miguel2005 (a), Kume2004, Kume2003]. According to Kume *et al.* the phase transition can be explained due to a disordering of the guest atoms. A detailed description of the high pressure behaviour of silicon clathrates can be found in a recent review by [San-Miguel2005 (b)].

Table 3.1: Phase transition in silicon clathrate compounds

Formula	P_{T1}[GPa]	$P_{V_{T2}}$[GPa]	$P_{amorph.}$[GPa]
cd-Si		11.5(β-tin)	
Si_{136}		11.5 ± 1(β-tin)	
Na_8Si_{46}		13 ± 2(β-tin)	
Ba_8Si_{46}	6 ± 1	13 ± 2(reversible volume collapse)	40 ± 3
K_8Si_{46}	6.5 ± 1.5	23 ± 3(reversible volume collapse)	32 ± 3
Rb_6Si_{46}		26 ± 3(reversible volume collapse)	35 ± 3
$I_8Si_{44}I_2$		35 ± 3(reversible volume collapse)	47 ± 3

[San-Miguel2005 (b)]

3.1.1 The structure I silicon clathrate

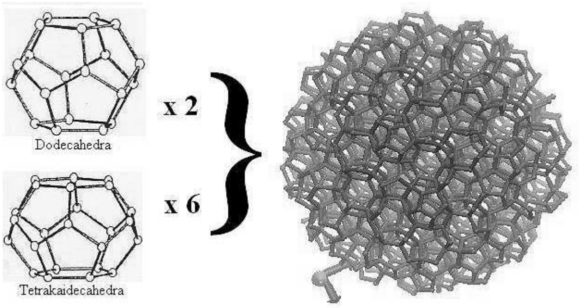

Figure 3.3: *Silicon cages of a structure I clathrate. Two dodecahedra and six tetrakaidecahedra are forming a 46 atom unit cell with up to eight guest atoms or molecules.*

The structure of a hypothetically empty-caged silicon type-I clathrate is presented in figure (3.3). A unit cell consists of two smaller Si_{20} and six larger Si_{24} cages resulting in 46 silicon atoms with up to 8 guest atoms at the given empty sites. The dodecahedra (Si_{20}) show 12 solely pentagonal faces (5^{12}), whereas the tetrakaidecahedra (Si_{24}) are built of 12 pentagonal and two opposing hexagonal faces ($5^{12}6^2$). M_xSi_{46}, also referred to as $M_x@Si_{46}$ is simple cubic (*sc*) with space group $Pm\bar{3}n$ and a lattice constant a of about 10.2 Å (see table [3.2]) depending on the type of dopant M. The occupation number x varies from full occupation (M= Na, Ba) to fractional occupation [M = K(x=7.6), Rb(x=6.7)] while the six larger tetrakaidecahedra are filled first [RENY1998]. Using Wyckoff notation [WYCKOFF1963] three non-equivalent sites for the silicon atoms exist at the 6c [Si(1)], 16i [Si(2)] and 24k [Si(3)] positions, while the guest atoms reside at the center of the small (2a) and the large (6d) cages. Four distinct Si-Si bond lengths and eight distinct Si-Si-Si bonding angles can be found (see table [3.3] and figure [3.4]). Although the volume per atom is about 15% larger in silicon clathrates than in diamond silicon the mean bond length as well as the mean bonding angles vary only slightly if compared to the cubic diamond silicon (cd-Si). More complex clathrates are known with different

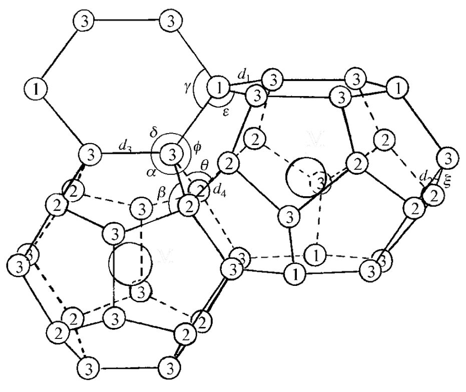

Figure 3.4: *Representation of two connected cages in the M_8Si_{46} structure. The eight non-equivalent bonding angles and the four Si-Si bond lengths are indicated* [RENY1998].

types of dopants filling the two Si_{20} and the six Si_{24} cages ($M_6N_2Si_{46}$) [Kawaji1995] as well as ternary compounds with transition metals (TM = Au, Ag, Ni, Pt, Pd or Cu) replacing up to $y = 6$ of the silicon atoms in the host lattice ($M_8Si_{46-y}TM_y$) [Hermann1998, Cordier1991].

Table 3.2: Lattice constants of distinct silicon clathrates of structure I and structure II (M = type of guest atom, x = the occupation number and δ = replaced silicon atoms).

	Space group	Formula	Lattice constant [Å]
Structure I	$Pm\bar{3}n$	$M_xSi_{46-\delta}M_\delta$	
		Si_{46} (hypoth.)	10.007-10.35[5,7,8,9,10,11]
		Na_8Si_{46}	10.196[7]
		$K_{7.6}Si_{46}$	10.278[12]
		$Rb_{6.7}Si_{46}$	10.293
		Ba_8Si_{46}	10.192-10.328[4,5]
		$I_8Si_{44}I_2$	10.42[3]
Structure II	$Fd\bar{3}m$	M_xSi_{136}	
		Si_{136}	14.479-14.626[2,6,8,9,11]
		Na_1Si_{136}	14.643[13]
		$Na_{20.5}Si_{136}$	14.703[13]
		$Na_{24}Si_{136}$	14.643[1]
cd-Si	$Fd\bar{3}m$	Si	5.43

[1] [Tournus2004], [2] [Nolas2003], [3] [Reny2002(a)], [4] [Yamanaka2000], [5] [Moriguchi2000], [6] [Gryko2000], [7] [Ramachandran1999(a)], [8] [Kahn1997], [9] [Menon1997], [10] [Saito 1995], [11] [Adams1994], [12] [Tse2002], [13] [Reny1998]

3.1.2 The structure II silicon clathrate

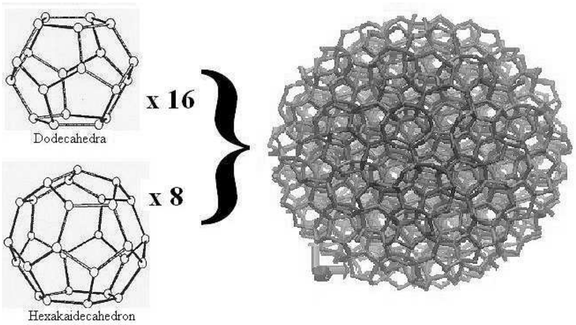

Figure 3.5: *Silicon cages of a structure II clathrate. 16 dodecahedra and 8 tetrakaidecahedra are forming a 136 atom unit cell with up to 24 guest atoms or molecules.*

The empty-caged type-II clathrate is depicted in figure (3.5). A unit cell consists of 16 smaller Si_{20} and 8 larger Si_{28} cages resulting in 136 silicon atoms with up to 24 guest atoms at the given empty sites. The dodecahedra (Si_{20}) show 12 solely pentagonal faces (5^{12}), whereas the hexakaidecahedra (Si_{28}) are built of 12 pentagonal and four hexagonal faces ($5^{12}6^{4}$). The stoichiometric composition is M_xSi_{136}. The type-II clathrate is a face centered structure (fcc) with space group $Fd\bar{3}m$ and a lattice constant a of about 14.6 Å (table [3.2]). In contrast to the structure I clathrate the filling of the cages can be tuned freely ($0 \leq x \leq 24$). But again the larger cages are exclusively filled first [Reny1998]. Three non-equivalent sites for the silicon atoms exist at the 2a [Si(1)], 32c [Si(2)] and 96g [Si(3)] positions while the guest atoms reside at the center of the small (8b) and the large (16c) cages. The Si-Si bond lengths and the Si-Si-Si bonding angles can be found in table (3.3) and are indicated in figure (3.6). Again, the mean Si-Si bonds and mean bonding angles differ only slightly to those of cubic diamond silicon. While ternary structure II clathrates are well known no replacing of the lattice atoms has been observed until now.

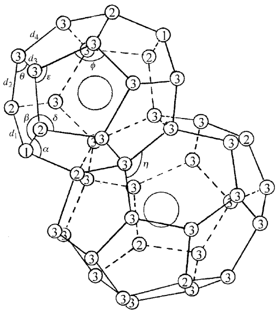

Figure 3.6: *Representation of two connected cages in the M_xSi_{136} structure. The eight non-equivalent bonding angles and the four Si-Si bond lengths are indicated* [Reny1998].

Table 3.3: Atomic coordinates, Si-Si distance and Si-Si-Si bonding angles of selected structure I and structure II silicon clathrates.

	Pm$\bar{3}$n (structure I)		Fd$\bar{3}$m (structure II)		
	$Na_8Si_{46}^1$	$Ba_8Si_{46}^2$	cd-Si^3	Si_{136}^4	$Na_{20.5}Si_{136}^1$
Atomic positions (Wyckoff notation[a]) ... of the silicon atoms	6c Si(1) 16i Si(2) 24k Si(3)		8a	8a Si(1) 32a Si(2) 96a Si(3)	
... of the guest atoms	2a M(1) 6d M(2)		- -	- -	8b 78% Na(1) 16c Na(2)
Bond length spread [Å] (Si-Si)	2.31 -2.39	2.27 -2.48	- -	2.34 -2.38	2.34 -2.42
(M(1)-Si)	3.26 -2.37	3.34 -3.39	- -	- -	3.91 -3.99
(M(2)-Si)	3.43 -3.79	3.50 -3.82	- -	- -	3.18 -3.38
Mean bond length [Å]	2.37	-	2.35	2.34	2.37
Bonding angle spread [°] (Si-Si-Si)	105.2 -124.8	105.5 -123.7	- -	105.7 -119.5	105.3 -119.8
Mean bonding angle [°]	≈ 109.5	≈ 109.5	109,5	≈ 109.5	≈ 109.5

[a][Wyckoff1963], [1][Reny1998], [2][Yamanaka2000], [3][Melinon1999], [4][Gryko2000], [5][Kahn1997]

3.2 Synthesis of silicon clathrates

Without exception, group-IV clathrates are synthetically prepared materials. The first synthesis of silicon and germanium clathrates was realized by Cros *et al.* [Cros1965, Kasper1965] and Gallmeier *et al.* [Gallmeier1967, Gallmeier1969] through thermal decomposition of alkaline silicides and germanides. Depending on the type of dopant, the pyrolysis temperature, and the decomposition under vacuum or inert atmosphere, either the structure I clathrate or the structure II clathrate is formed. In the scope of the last decades the core of the preparation process has remained unchanged.

In a first step the Zintl phase silicide MSi (with M = Na, K, Rb) is prepared by heating a mixture of silicon and an excess of the corresponding metal under inert or vacuum conditions at temperatures of $600-1000$ K for a couple of hours in a stainless steel vessel. After the removal of the remaining silicon and metal, the highly reactive silicide powder is wrapped in tantalum foil and put into a dry box with evacuated (10^{-5}Pa) or inert atmosphere (e.g. argon). The box is put into a furnace and heated for about 60 h.

For sodium both structure I and structure II clathrates can be obtained. Under vacuum conditions only the structure II Na_xSi_{136} is built [Ramachandran1999(b)] with $3 \leq x \leq 13$ corresponding to the temperature used (T = 330-460°C). The structure I Na_8Si_{46} is only obtained by treating the NaSi under argon atmosphere at a temperature of $T = 450$°C. The occupation of the empty sites in the structure II sodium clathrate can be tuned above $x = 13$ by adding sodium vapor to the stainless steel vessel. Thus a full occupancy of the cages with $x = 24$ can be obtained. For potassium ($T = 530$°C) and rubidium ($T = 530$°C) only structure I clathrates are known. While the potassium doped clathrate shows nearly full occupancy of the cages, $K_{7.6}Si_{46}$, the rubidium fills the larger Si_{24} cages and some of the Si_{20} cages, $Rb_{6.7}Si_{46}$. The cesium ($T = 500$°C) resides in the Si_{28} cages of the structure II clathrate (Cs_7Si_{136}), and does not form a structure I clathrate because of its size.

The first quasi empty-caged clathrate was produced by prolonged heating of the structure II sodium clathrate for several days and was realized by Gryko *et al.* [Gryko2000]. Due to extended defects in the structure of the clathrate [Nistor1994, Ramachandran1998] the sodium evaporates and is subsequently washed out of the sample using hydrochloric acid. Recently, Ammar *et al.* [Ammar2004] presented a novel method to prepare the empty-caged clathrate by the use of iodine resulting in a further reduction of the sodium content to $x = 0.0058$.

The obtained finely powdered samples can contain small amounts of crystalline silicon of about 1 % to 5 % [QIU2001, AMMAR2004, NOLAS2003, FANG1998]. Additionally, amorphous silicon oxide impurities of the same order of magnitude have been reported by several authors [HE2001, GRYKO2000, AMMAR2004]. For the sodium clathrates traces of the respective other structure [QIU2001, AMMAR2004, RAMACHANDRAN1999(A), RENY1998] can be separated by using a centrifuge after solving the sample in an organic liquid like chlormethane or dibromomethane. The powders have an average grain size of about 2-3 μm. Aside from an at least 50 Å measuring layer of amorphous silicon dioxide at the grain boundery [HE2001] the compounds are inert and do not react with air, moisture and most acids with the exception of hydrofluoric acid.

It should be noted that some clathrates need high pressure and high temperature (HPHT) conditions for their synthesis (e.g. Ba_8Si_{46} or $I_8Si_{44}I_2$) [RENY2000, RENY2002(A), YAMANAKA2000].

3.3 Properties and research

Aside from the remarkable stability and high pressure behaviour of the silicon clathrates discussed in section (3.1), many interesting physical properties have been found for the different silicon clathrate compounds. The initial interest focused on the electrical properties. While the heavily doped structure I sodium and potassium clathrates show metallic behaviour, the structue II Na_xSi_{136} is semiconducting for $x < 8$ and transforms to a metal with increased doping above $x = 8$ [CONESA 2004, MOTT1973, CROS1970].

The research on silicon clathrates intensified again after the discovery of superconductivity in alkali-metal doped fullerenes M_3C_{60} [HEBARD1991, ROSSEINSKY1991, TANIGAKI1991]. The proximity of fullerene and clathrate structures led to the hope of finding superconductivity in the group-IV clathrates as well. But no superconduction transitions were evidenced for sodium doped silicon clathrates down to a temperature of 2 K [ROY1992]. In 1995, Yamanaka *et al.* [YAMANAKA1995] successfully encapsulated barium atoms into the structure I silicon clathrate to form a mixed barium and sodium doped structure, $Na_{2.9}Ba_{4.5}Si_{46}$. Its superconductivity with T_C of about 4 K was shown by the same group [KAWAJI1995]. In the same year, structural calculations [SAITO 1995] showed a strong hybridisation of the barium 5d electrons with the silicon atoms of the host lattice leading to a high density of states at the Fermi level. In the Bardeen-Cooper-Schrieffer model [BARDEEN1957] a strong phonon coupling as well as a high density of states at the Fermi level are important parameters for superconductivity and have been studied extensively in the following years along with the synthesis of other superconducting clathrates [YAMANAKA1995, MELINON1999, YAMANAKA2000, YOKOYA2001, RENY2002(B)]. The highest value of the critical temperature of 8 K was found in the completly barium doped silicon clathrate Ba_8Si_{46}. A detailed list on the superconducting properties of group-IV clathrates is given in [SAN-MIGUEL2005 (B)].

In various theoretical publications a wide band gap has been proposed for the empty-caged structure I and structure II silicon clathrates as well as for the iodine doped I_8Si_{46} [SAITO 1995, ADAMS1994, DEMKOV1994, MELINON1998, MENON1997, CONNETABLE2001, BLASE2003] offering promising optoelectric applications. They predicted a widening of the band gap of about 0.7 eV compared to that of the diamond phase of silicon leading to a direct band gap of about 1.9 eV. At least for the Si_{136} clathrate the predictions could be verified experimentally [GRYKO2000].

Another broad field of recent research on clathrate materials are their thermoelectric properties. The figure of merit of a good thermoelectric material Z is given by

$$ZT = S^2\sigma / (\kappa\ T) \tag{3.1}$$

with the Seebeck coefficient S, electrical and thermal conductivity σ and κ (see e.g. [SLACK1995]). The absolute temperature T is introduced to obtain a dimensionless quantity ZT. A first concept to design thermoelectrics was developed by Ioffe [IOFFE1957] and introduced the use of semiconductors, which are heavily doped with high Z elements like tellurides of antimony and bismuth (e.g. Bi_2Te_3). The figure of merit for those materials is only large for a specialized temperature regime and does not exceed $ZT \approx 1$, while $ZT \geq 3$ would be needed to outperform the efficiency of conventional cooling systems. In 1995 Slack [SLACK1995] proposed the concept of a phonon glass and an electron crystal (PGEC) with glasslike thermal conductivity and a crystal like electrical conduction. Therefore, group-IV clathrates are good candidates for thermoelectric materials. Their glass-like thermal conductivity was evidenced both experimentally [NOLAS1998, COHN1999, TSE2000, MUDRYK2002] and theoretically [Blake1999, Qiu2001, Dong2001] and is believed to have its origin in the scattering of thermal phonons of the guest atom. This is due to the avoided-crossing of localized phonon bands of the metal with the framework accoustic branch of the same symmetry [Tse2001]. Numerous works have studied the vibrational modes and the phonon density of states and could verify the above model [Kahn1997, Fang1998, Melinon1999, Reny2002(b)]. It should be noted that Nolas [Nolas2003] found low thermal conductivity also in the empty-caged Si_{136}, so that at least some of the thermal properties are intrinsic properties of the silicon host lattice.

In summary, the guest-host interactions in silicon clathrates are of essential importance in order to understand the varying attributes of the complex materials. For example the phonon coupling on the meV scale is a key to understand superconductivity as well as thermal properties of the clathrates. Electron-electron interactions like a charge transfer or hybridization of guest and host orbitals are on the eV scale. On the one hand, the sodium to silicon distance in the clathrates exceeds that of the ionic silicide. On the other hand, the empty caged Si_{136} is a semiconductor. With increased doping of sodium it first becomes a semi-metal and finally shows metallic electrical conductivity, which leads to the assumption of a transfer of the sodium valence electron to the silicon host lattice.

Chapter 4

Compton scattering on silicon clathrates

In order to study the guest-host interaction in silicon clathrates a systematic Compton scattering study on alkali-metal doped silicon clathrates was performed. Compton scattering is a unique tool to observe the electron momentum distribution of a given material in its ground state and thus is sensitive to a change of the electron wave function itself. Charge transfer, metallic or insulating properties especially influence the shape and broadness of the valence contribution to the overall Compton profile. The aim of the experiment is to digest the valence Compton profile of the alkali-metal guest atoms and to compare the results with DFT calculations.

This chapter begins with the description of the two setups for Compton scattering experiments at the European Synchrotron Radiation Facility (ESRF) in Grenoble, France [ESRF2006]. It is followed by a detailed overview of the data evaluation process. Afterwards, the reference Compton profiles of polycrystalline silicon and the empty-caged Si_{136} are compared with calculated spectra and results of a former experiment. Finally, a first analysis of the Compton profiles of the alkali-metal doped silicon clathrates is presented.

4.1 Compton scattering at beamline ID15B at the ESRF

All Compton scattering experiments were performed at ID15B of the ESRF in Grenoble, France. For two different incident energies of about 60 keV and 90 keV two different setups, setup A and setup B, were used. Both setups are described below.

4.1.1 Setup A: Standard Compton scattering setup using 60 keV incident photon energy

The general outline of the experimental endstation of beamline ID15B with a scanning-type Compton spectrometer is illustrated in figure (4.1). A schematic overview is given in figure (4.2). The incoming beam was generated by an asymmetric multipole wiggler and monochromatized by a Ge(440) bent Bragg-crystal to an energy of 56.735 keV. The incoming flux was monitored by a pin diode and the signal was analyzed in back scattering geometry ($\theta = 173°$) by a Rowland type spectrometer using a Si(400) spherically bent analyzer Bragg-crystal and a NaI solid state detector. Additionally, a germanium detector was positioned at a scattering angle of $\theta_{\mathrm{Ge}} = 160°$ using a multi channel analyzer to read out the data. By integrating over all channels the obtained signal was used as a second monitoring signal. The experimental resolution was determined by the full width and half maximum of the Rayleigh line. Following [Suortti2001] the resolution at the Compton peak ($p_z = 0$ a.u.) was extrapolated to 0.16 a.u. The beam was focused to the sample to a broadness of 0.3 mm and a height of 5 mm. The corresponding horizontal gap and vertical gap of the monochromator slit-system were 5 mm and 3.5 mm, respectively. A more detailed description of the beamline setup can be found in references [Suortti1995, Suortti1999]. Compton

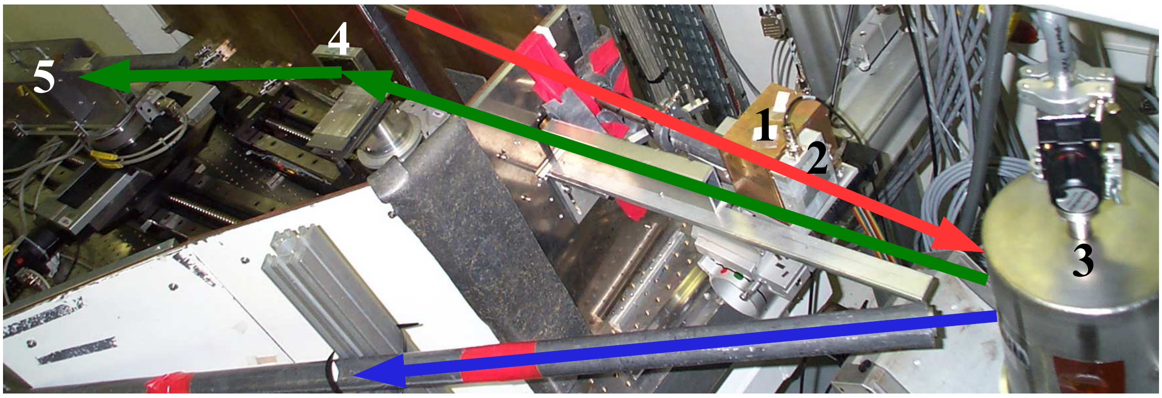

Figure 4.1: *Experimental setup at ID15B with 60 keV incident photon energy. The incoming beam (red) passes a slit system (1) and is monitored by a pin diode (2). It interacts with the sample, which is placed in a vacuum chamber (3). The scattered photons are measured twofold: First, a germanium detector was used to obtain a second monitor signal (blue). Second, the scattered beam (green) is analyzed by a spherically bent Si(400) crystal (4) and measured by a solid state NaI detector (5).*

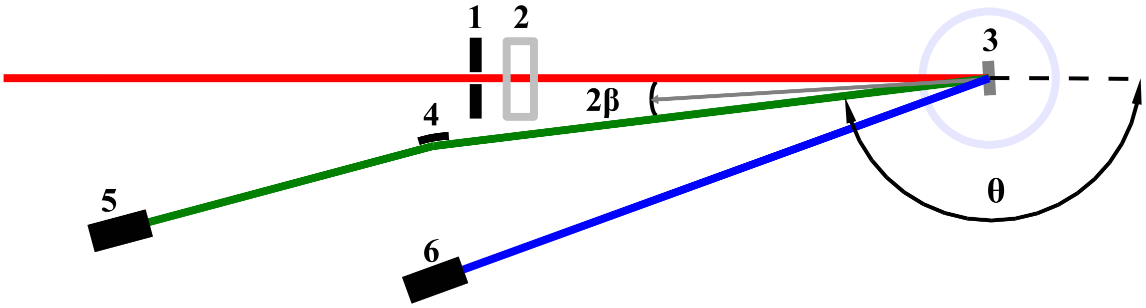

Figure 4.2: *Schematic picture of the experimental setup at ID15B with 60 keV incident photon energy. The incoming beam passes a slit system (1) and is monitored by a pin diode (2). It interacts with the sample, which is placed in a vacuum chamber (3). The surface normal of the sample (dark grey) is pointing to half of the angle between incident and scattered photon beam (2β). Moreover, the germanium detector (6) the spherically bent Si(400) crystal (4) and the solid state NaI detector (5) are shown.*

spectra were measured for sodium and potassium doped silicon clathrates as well as the empty-caged structure II silicon clathrate and polycrystalline silicon as reference materials. The powdered samples were filled into a sample holder consisting of a 2 mm channel countersunk into a 1 mm thick and 2 cm by 2 cm wide aluminum plate. In beam direction, the channel was limited by Kapton foils of 25 μm thickness. In positioning the surface normal of the sample holder to $\beta = -(180° - \theta)/2 = -3.5°$ the momentum transfer was chosen perpendicular to the surface of the sample at $p_z = 0$ a.u. To reduce the amount of air scattering, the sample was placed into a vacuum chamber, which is evacuated to a pressure of 10^{-6} Pa. The incident photon energy was calibrated to 56.74 keV using the fluorescence lines of Sn. A broad and a narrow scan range were defined for measuring the Compton profiles. For a proper analysis of the core electron contribution to the Compton profile the broad scan ranged from -17.2 a.u. to 12 a.u. on the p_z-scale. It covers a large portion of the overall Compton profile as well as the Rayleigh line. The narrow scan ranged from -3 a.u. to 3 a.u. on the p_z-scale and covers the region of interest of the valence Compton profile. To remain sensitive to systematic errors multiple single scans with the focus on the narrow scans were performed until a statistical accuracy of about 0.1 % at the maximum of the Compton profile was achieved.

For each sample a diffraction pattern was measured by using the available imaging plate setup at the beamline. The imaging plate [MAR345] has a diameter of 345 mm and was placed 1006 mm behind the sample. To enhance the resolution of the diffraction patterns, the horizontal and the vertical gap of the monochromator were reduced to 0.2 mm both. The diffraction patterns were measured by opening the beam shutter for 1 to 4 seconds.

4.1.2 Setup B: Dispersion compensating setup at 90 keV incident photon energy

The incident beam for this setup was first monochromatized by a Si(511) cylindrically bent Laue crystal. The incoming flux was monitored by a pin diode and the scattered photons were analyzed by a second Laue type Si(400) crystal at $\theta = 173.5°$. A germanium detector was positioned at a scattering angle of $\theta_{\mathrm{Ge}} = 160°$ and used as a second monitor. At the sample the beam was 2 mm broad while the height of the beam had to be varied according to the sample size. Therefore, the experimental resolution ranged from 0.09 a.u. for Si_{136} to 0.13 a.u. for diamond silicon, silicon oxide and silicon dioxide. The resolution was calculated as for setup A. In order to enhance the energy resolution at the high incident energy, the geometry of the setup is designed to compensate for the energy dispersion of the incident beam. A

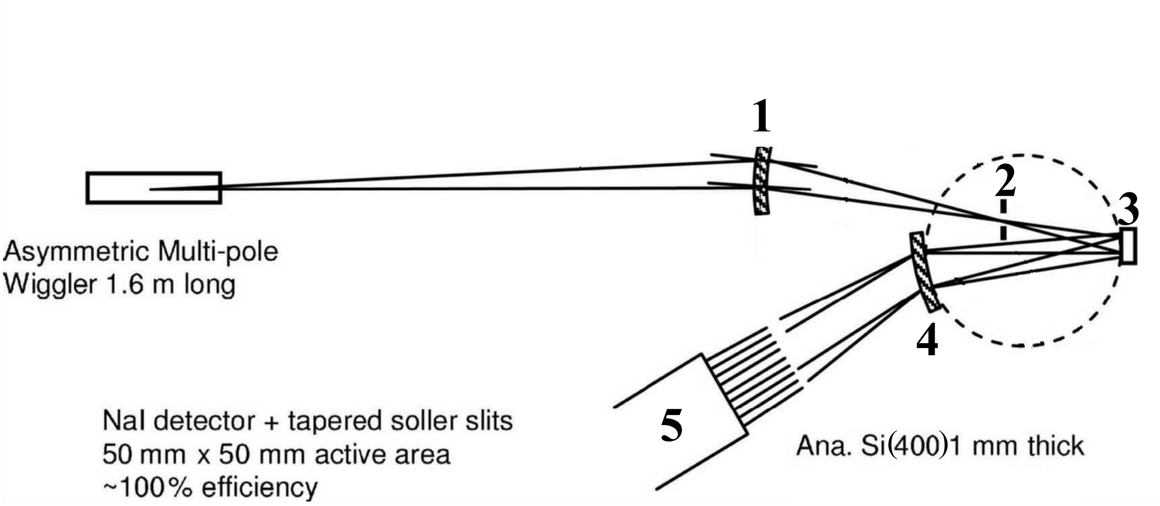

Figure 4.3: *Experimental setup at ID15B with 90 keV incident photon energy. The photon source is an asymmetric wiggler and the photon energy is monochromatized by a Laue type Si(511) crystal (1). The bending of the crystal focuses the beam to a slit system (2). After hitting the sample (3) the scattered photons are analyzed by a second Laue type crystal (4) and a NaI solid state detector system (5)* [HIRAOKA2005].

more detailed description of this setup can be found in references [HIRAOKA2005, SUORTTI2001].

Compton spectra were measured for silicon oxide, silicon dioxide, silicon and the empty caged silicon structure II clathrate. The powdered samples were filled into a sample holder consisting of a 3 mm channel countersunk into a 1 mm thick and 2 cm by 2 cm wide aluminum plate. The thickness of the Kapton windows of the sample holders was 8 μm and for the Si_{136} no Kapton was needed at all because the clathrate was pressed to a disc of 4 mm in diameter and 0.5 mm thickness. Again the sample holder was positioned to $\beta = -(180° - \theta)/2 = -3.25°$, so that the momentum transfer was perpendicular to the surface of the sample at $p_z = 0$ a.u. To reduce the background signal, a slit system together with a lead shielded metal tube was installed in front of the analyzer crystal of the spectrometer. The incident photon energy was calibrated to 88.4 keV by using the fluorescence lines of Pb. The broad scans ranged from -17.2 a.u. to 12 a.u. on the p_z-scale the narrow scans from -3 a.u. to 3 a.u. Single spectra were measured with the focus on the narrow scans in order to reach a statistical accuracy on the Compton peak of 0.1 %. For this beamtime no imgaing plate setup was available.

4.2 Data analysis

To obtain the directional Compton profile from a Compton scattering experiment the measured intensitiy $I(\omega_2)$ has to be corrected for various contributions. It depends on the experimental and electronic background B, a constant factor C, an energy dependent correction factor $(A/B)_{\mathrm{total}}(\omega_2)$ and a contribution of the multiple scattered photons $MS(\omega_2)$:

$$I(\omega_2) = B + C \cdot (A/B)_{total}(\omega_2) \cdot (J(\omega_2) + MS(\omega_2)) \; . \tag{4.1}$$

The data analysis is similar for both setups. In a first step the single spectra have to be added and checked for systematic errors. The resulting added spectra of the two scan ranges are merged by adding the tails of the Compton profile of the larger scan range to the more detailed narrow scans of the valence regime (section 4.2.1). In a second step the spectra are corrected for energy dependent factors like air absorption or relativistic corrections to the cross section (section 4.2.3). Afterwards, the contribution of multiple scattered photons to the Compton profile is calculated from Monte Carlo simulations and subtracted from the data (section 4.2.5). The remaining asymmetry of the resulting Compton profiles is then extracted from the experimental data and subtracted as well (section 4.2.6). Finally all spectra are normalized to the number of electrons per silicon atom.

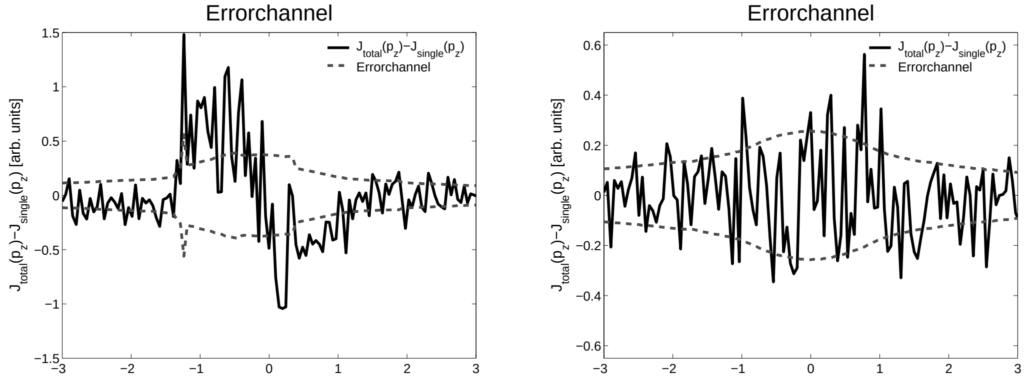

(a) (b)

Figure 4.4: *The difference between a single spectrum and the total sum of the spectra (solid line) of the* K_8Si_{46} *sample compared with the errorchannel of the single spectrum (dashed line). (a) The measured Compton profile directly after an injection. (b) A spectrum without any systematic deviations.*

4.2.1 First analysis of the data

The electronic noise is determined by measuring the signal of the detectors with a closed beam shutter for 100 seconds. The background signal is measured by decalibrating the analyzer crystal for 1° and performing a scan over the p_z-range of the broad scans. After subtracting the background signals the data analysis starts with adding up the single spectra $J_{\text{single}}(p_z)$ to a total spectrum $J_{\text{total}}(p_z)$ of the experiment. Each single spectrum is analyzed for systematic errors by comparing the difference spectrum $J_{\text{total}} - J_{\text{single}}$ with the corresponding errorchannel $\pm\sigma_{J_{\text{single}}}$. Especially after an injection or a downtime of the storage ring, the monochromator needs some time to reach equilibrium temperature and some spectra cannot be added to the total spectrum (see figure 4.4).

4.2.2 The 'glitch' of the Rowland spectrometer

The experimental setup of the Rowland spectrometer shows a typical glitch at -1.7 a.u., which is due to a Bragg reflection of the analyzer crystal of the spectrometer. As the glitch would strongly influence the asymmetry of the Compton profiles, the

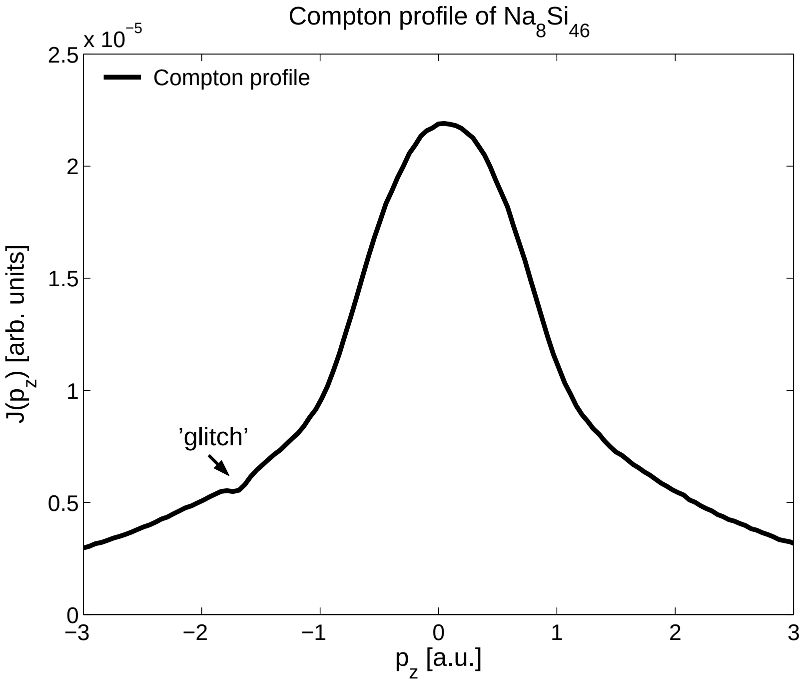

Figure 4.5: *The glitch of the Rowland spectrometer for the* 60 *keV setup at* -1.7 *a.u.*

relevant area is cut out of the data set (see e.g. [Huotari2001]). Note that the cut out area has to be interpolated in the course of the data analysis.

4.2.3 Energy dependent corrections

The measured intensities of a Compton scattering experiment have to be corrected for energy dependent factors. Though the energy of the incident photons remains constant during a Compton scattering measurement, the scattered photons show an energy spectrum. Therefore, the energy dependent correction factors strongly affect the shape of the measured profile. Some energy dependencies are due to the experimental setup (air transmission, sample thickness, sample density, element type as well as the efficiency and the geometry of the spectrometer), while some have theoretical origin (relativistic corrections, scale correction). Although the correction factors are a function of the incident and the scattered energy, the mathematical formulation is the same for both setups. Where necessary it will be distinguished between setup A and setup B.

Air transmission

As the incident photon energy is constant only the air absorption of the scattered radiation has to be accounted for. Note, that the distance between sample and detector d_{air} changes with the analyzed photon energy. The parameter μ_{air} represents the absorption coefficient for air at standard pressure (1013 hPa) and θ_B denotes the Bragg angle of the analyzer crystal:

$$(A/B)_{\mathrm{air}} = e^{-(d_{\mathrm{air}}(\theta)\,\mu_{\mathrm{air}}(\omega_2))}\,. \tag{4.2}$$

Sample absorption

In case of the photon absorption in the sample itself both, the incident photon beam and the scattered beam have to be accounted for. The correction factor depends on the absorption coefficient of the given sample $\mu_{\mathrm{S}} = \mu(\omega_1)+\mu(\omega_2)$, the sample thickness d_s and the angle $\beta = 3.5°$. As the sample is adjusted so that its surface normal points to the middle of the scattering angle, the angle of the incident beam and the observed scattered photons to the sample surface are the same:

$$(A/B)_{\mathrm{sample}} = \frac{1 - e^{-d_{\mathrm{s}}\mu_{\mathrm{s}}/\cos(180-\beta)}}{\mu_{\mathrm{s}}/\cos(180-\beta)}\,. \tag{4.3}$$

Vertical acceptance of the Rowland spectrometer (setup A)

The vertical acceptance of the Rowland spectrometer is a function of the distance p between sample and analyzer and the distance q between analyzer and detector . Both are a function of the Bragg angle θ_B, while the distance of the sample to the analyzer slit $d = 703$ mm remains constant. With the vertical opening of the detector $h_\mathrm{D} = 70$ mm, the analyzer slit $h_\mathrm{s} = 35$ mm and the height of the analyzer crystal $h_\mathrm{A} = 61$ mm, the acceptance of the spectrometer is calculated as follows:

$$A_\mathrm{acc} = \left(min \left\{ \frac{h_\mathrm{S}}{d} \, ; \frac{h_\mathrm{A}}{p} \, ; \frac{h_\mathrm{D}}{p+q} \right\} \right) . \tag{4.4}$$

Analyzer reflectivity (setup A)

The reflectivity of the analyzer crystal A_refl is calculated by the program REFLECT available at beamline ID15. It accounts for the polarization state of the scattered photons and is founded on the dynamical theory of diffraction (for details see [EROLA1990]).

Scale correction (setup A)

As the spectrometer does not measure the intensity of the scattered photons as a function of the energy ω_2 but of the Bragg angle θ_B, a scale correction has to be introduced:

$$\frac{d^2\sigma}{d\Omega d\omega_2} = \frac{d^2\sigma}{d\Omega d\theta_\mathrm{B}} \frac{d\theta_\mathrm{B}}{d\omega_2}$$

resulting in a correction factor

$$A_\mathrm{scale} = \frac{d\omega_2}{d\theta_\mathrm{B}} = \frac{\omega_2}{\tan\theta_\mathrm{B}} . \tag{4.5}$$

Vertical acceptance, analyzer reflectivity and scale correction (setup B)

The vertical acceptance of setup B is defined by the vertical opening of the analyzer slit $h_\mathrm{A} = 25$ mm. The reflectivity of the analyzer crystal was calculated by N. Hiraoka [HIRAOKA2006] and the resulting correction factor $B_\mathrm{refl/scale}$ is available at beamline ID15. The calculation already includes the scale correction factor.

Relativistic cross section correction

Finally the spectra have to be corrected for relativistic effects. As the incident photons are linearly polarized, equation (1.35) defines the correction factor $(A/B)_{\mathrm{rel}}$. It depends on the incident energy ω_1 and the scattered energy ω_2 of the photons, the scattering angle θ and finally β, the angle between the scattering plane and the polarization vector of the incident photons.

4.2.4 The total energy correction factors for setup A and setup B

In summary, the total correction factors are

$$A_{\mathrm{total}} = A_{\mathrm{air}} \cdot A_{\mathrm{sample}} \cdot A_{\mathrm{acc}} \cdot A_{\mathrm{refl}} \cdot A_{\mathrm{scale}} \cdot A_{\mathrm{rel}} \tag{4.6}$$

for setup A and

$$B_{\mathrm{total}} = B_{\mathrm{air}} \cdot B_{\mathrm{sample}} \cdot B_{\mathrm{acc}} \cdot B_{\mathrm{refl/scale}} \cdot B_{\mathrm{rel}} \tag{4.7}$$

for setup B.

As solely $(A/B)_{\mathrm{sample}}$ depend on the analyzed material, the correction factors are shown for one sample per setup exemplarily: In figure (4.6) for $\mathrm{Na_8Si_{46}}$ (60 keV incident energy) and in figure (4.7) for $\mathrm{Si_{136}}$ (90 keV incident energy). For reasons of comparability all correction factors are normalized to the first point of the given curve. According to equation (4.1), the Compton profiles are corrected by dividing the data by the given factor A_{total} and B_{total}, respectively. The obtained spectrum contains only the multiple scattering contributions and the directional Compton profile itself. Before continuing with the analysis of the data the spectra are transformed to the p_z-scale using equation (1.26).

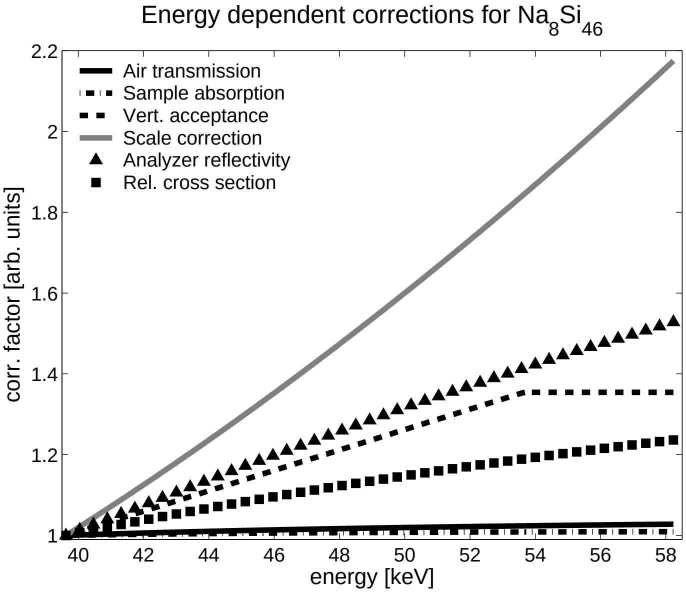

Figure 4.6: *Data correction factors at 60 keV incident photon energy for* Na_8Si_{46}*. The major factors are scale correction (solid grey line), analyzer reflectivity (triangles) and the vertical acceptance of the analyzer crystal (dashed line). At* 53.7 *keV the analyzer crystal is illuminated completly. The relativistic cross section correction (squares) is less important than for the* 90 *keV photons of setup B. Likewise, the absorption in air (solid line) and in the sample (dashed dotted line) are playing a minor role.*

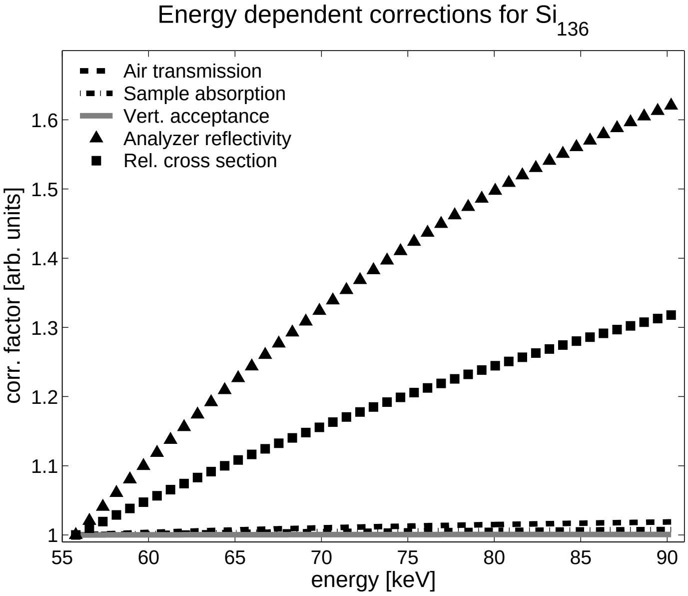

Figure 4.7: *Data correction factors at* 90 *keV incident photon energy for* Si_{136}*. The major factors are the reflectivity of the analyzer crystal, including scale correction (triangles) followed by the relativistic cross section correction (squares). Air absorption (dashed line), sample absorption (dashed dotted line) and vertical acceptance (solid grey line) of the spectrometer are playing a minor role.*

4.2.5 Multiple scattering

As a bulk sensitive method using hard x-rays, the multiple scattering contributions to the measured spectra are playing a minor role if compared to other experimental methods. Nontheless the contributions are of the order of up to 8 % (Fe at 90 keV incident energy [Cooper2004]) of the overall Compton profile and show asymmetries with respect to the Compton peak at $p_z = 0$ a.u. Especially the type of guest atoms changes significantly the amount, if not the shape of the spectra of the doubly and triply scattered photons. As the multiple scattering contribution depends on the incident energy, the polarization of the photons, the sample geometry and the scattering angle an exact calculation is a complex problem. Therefore, Monte Carlo simulations are widely used to model its shape and size (e.g. [Pitkänen1987]). For this work a Monte Carlo code available at beamline ID15 was used [Honkamäki2006]. Besides the above mentioned parameters the program accounts for the sample thickness, the density of the sample and the chemical formula of the material. After defining the number of incoming photons, the program calculates the primary scattered photons as well as the doubly and triply scattered ones. Thus it gives an estimate of the

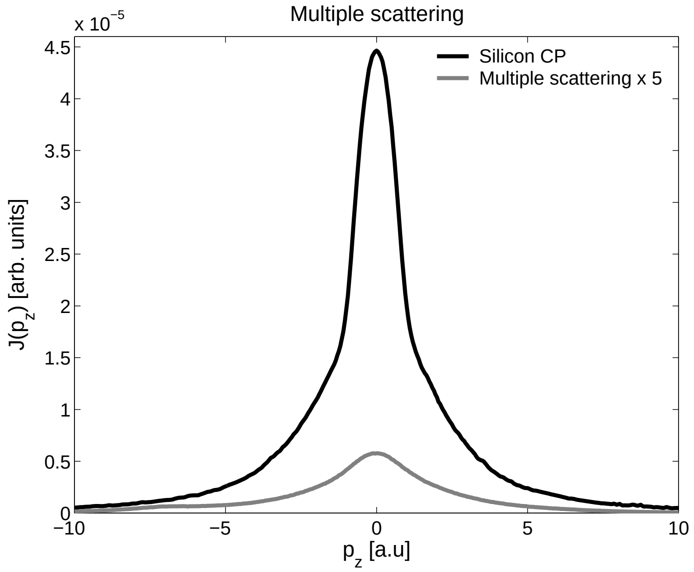

Figure 4.8: *The multiple scattering contribution (grey line) for silicon at* 60 *keV incident photon energy is depicted together with the corresponding measured spectrum (black line). To visualize the slight asymmetry of the calculated data the spectrum for the multiple scattering contribution is multiplied with a factor of five.*

relative contribution of multiple scattered photons to the measured data. For each spectrum the number of photons was varied in five steps from 10^5 to $2 \cdot 10^9$ to verify the convergency of the code. No significant difference was found between the spectra for 10^8, 10^9, and $2 \cdot 10^9$ incoming photons. The shape of the spectra for the tested samples remains similar in a given setup while only the magnitude varies with the material. The integral contribution of doubly scattered photons to the overall Compton profile ranges from 2% for the low density Si_{136} to 3% for the potassium doped K_8Si_{46}, whereas triply scattered events add only about 0.05% to the overall spectrum. Therefore, higher order contributions are not considered. In case of setup A the spectra show an asymmetry towards larger momentum transfer, whereas the spectra for 90 keV incident energy are more symmetric with respect to $p_z = 0$. As an example the measured and energy corrected spectrum of silicon is shown in figure (4.8) along with its second and third order contributions estimated by the Monte Carlo simulations. The spectrum for the multiple scattering contribution is magnified by a factor of five.

4.2.6 Asymmetry of the Compton spectra and normalization

As already mentioned in chapter (1.4), higher order corrections to the Impulse Approximation result in an intrinsic asymmetry of Compton profiles, which is element specific and depends on the energy of the incident photons. The asymmetry is defined as follows:

$$J_{\text{asym}} = \frac{J(p_z) - J(-p_z)}{2} \tag{4.8}$$

Therefore, the experimental data is interpolated to a p_z-scale ranging from -10 a.u. to 10 a.u. For setup A J_{asym} is fitted with a sine function excluding the range of the 'glitch' from the fit. The resulting function is subtracted from the spectrum. In case of setup B the experimentally gained asymmetries are directly subtracted from the data. In figure (4.9), the Compton profile of silicon at 90 keV incident photon energy is presented together with the asymmetry J_{asym} of the spectrum. The spectra are presented as a percentage of the Compton peak of the silicon Compton profile. The silicon Compton profile itself is devided by a factor of ten to enhance the shape of the asymmetry. The main structures of J_{asym} can be found in the valence regime of the Compton profile and are of the order of ±0.3 % of the Compton peak.

After subtracting the asymmetries all spectra have to be normalized to the number of electrons per silicon atom according to the f-sum rule (equation 1.29) discussed in chapter 1. As an experimental Compton profile is measured on a finite p_z-range, the number of electrons have to be weighted accordingly. This is done by normalizing the experimental spectra to the corresponding integral of the already correctly normalized Hartree-Fock spectra on a p_z-range of -10 a.u. to 10 a.u. For silicon and Si_{136}, the spectra are normalized to the Hartree-Fock spectrum of silicon. For the alkali-metal doped silicon clathrates an appropriate set of Hartree-Fock Compton profiles is used (e.g. $J^{\mathrm{HF}}_{\mathrm{silicon}} + 8/46 \cdot J^{\mathrm{HF}}_{\mathrm{sodium}}$ for $\mathrm{Na_8Si_{46}}$). Before the relevant areas are integrated, the Hartree-Fock Compton profiles are convoluted with a Gaussian function to match the experimental resolution of the corresponding measured Compton profile. In a final step all experimental spectra of setup B are convoluted with a Gaussian function to match the experimental resolution (FWHM) of setup A ($\sigma_A = 0.16$ a.u.). The FWHM of the Gaussian function σ_x is calculated by

$$\sigma_x = \sqrt{\sigma_A^2 - \sigma_B^2}\,, \tag{4.9}$$

with σ_B being the FWHM of the given spectrum.

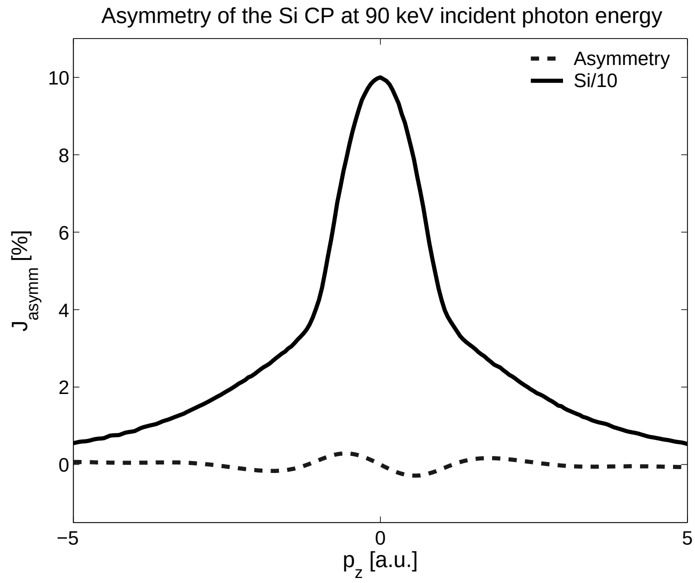

Figure 4.9: *Asymmetry of the silicon Compton profile at* 90 *keV incident photon energy after all corrections (dashed line) together with the Compton profile itself (solid line). The spectra are normalized to the Compton peak of the Compton profile of silicon, which is devided by a factor of ten.*

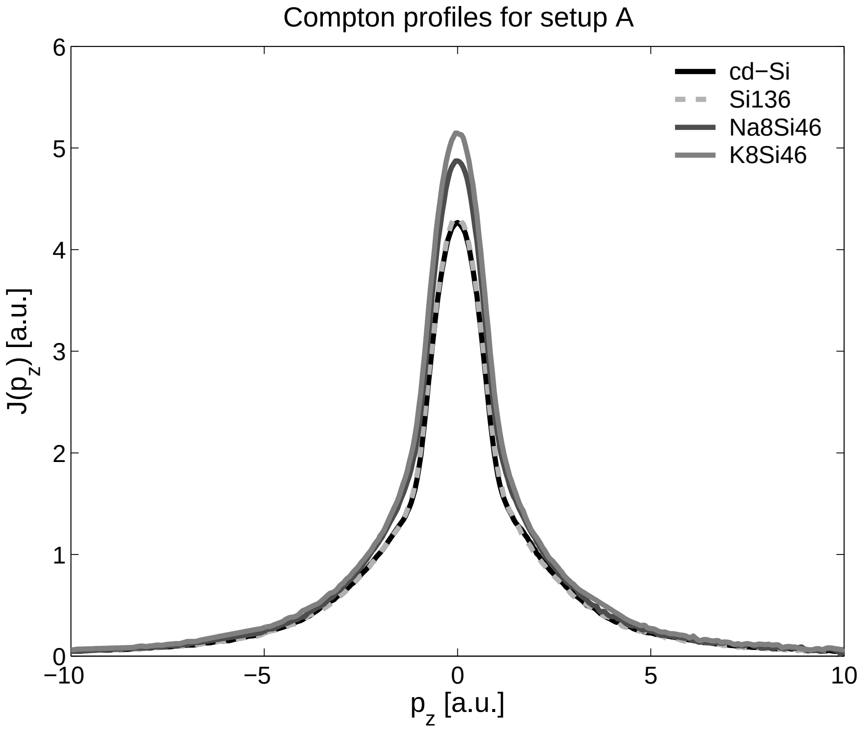

Figure 4.10: *Digested Compton profiles for setup A.*

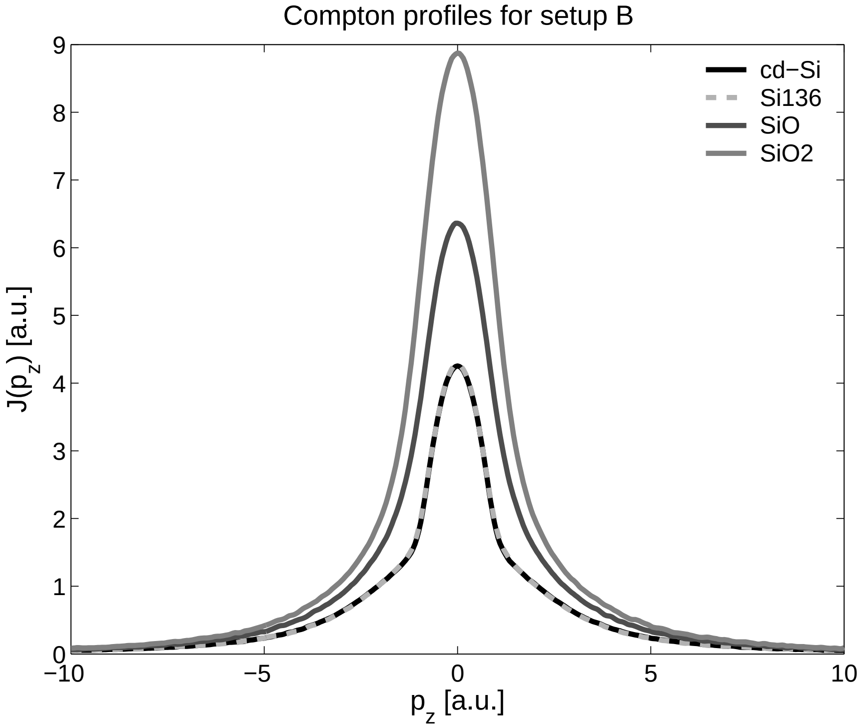

Figure 4.11: *Digested Compton profiles for setup B.*

4.3 Compton profiles of the valence electrons

The general idea of the experiment is to extract the valence Compton profiles of the different alkali-metal guest atoms of the doped silicon clathrates. Therefore, the contribution of the silicon host to the Compton profile has to be found. In this work this is achieved by measuring the Compton profile of an adequate reference material. The best suited material for such an analysis would be the empty-caged structure I Si_{46} clathrate, which could not be synthesized until now. Nonetheless, crystalline silicon and the structure II Si_{136} clathrate share the same sp^3 bonding as the Si_{46} host lattice. Additionally, the bond length and the average bonding angles are similar in the three materials (see table [3.3]). Thus, cubic diamond silicon and especially the empty caged structure II silicon clathrate are a good alternative as a reference material. Before beginning with the extraction of the valence contribution of the alkali-metal guest atoms though (see section 4.3.2), the systematic error made by the use of an alternative reference has to be estimated. Here, the difference between the Compton profiles of Si and Si_{136} gives an upper limit for this error (see section 4.3.1).

To obtain the valence electron contribution of the guest atoms, the silicon host lattice as well as the contribution of the guest atoms core electrons to the total Compton profile have to be subtracted from the spectra. Assuming guest-host interactions have little influence on core electrons, Hartree-Fock calculated Compton profiles are a good measure of the contribution of the guest atoms core electrons to the total Compton profile [Cooper2004]. In this work, tabulated Compton profiles for free atoms calculated by Biggs *et al.* are used [Biggs1975].

4.3.1 Analysis of the reference materials

Before discussing the digested valence Compton profiles a thorough analysis of the reference materials is important to estimate the error made by subtracting Si_{136} or polycrystalline silicon instead of a Si_{46} Compton profile. Below, the valence Compton profiles of polycrystalline silicon and the empty-caged structure II silicon clathrate are compared with DFT calculated spectra before the difference profile of silicon and Si_{136} is discussed. If available, the results are compared with recently published experiments or theory.

The calculations were performed within the Density Functional Theory using the Becke exchange and Perdew-Wang correlation, commonly known as B3LYP

[Stephens1994, Barone1994]. The atomic basis sets were taken from the CRYSTAL website [Crystal2006]. The calculations were performed with a Monkhorst-Pack k-point set [Monkhorst1976]. Calculations of the properties were performed with a large k-point set of $8 \cdot 8 \cdot 8$ or $12 \cdot 12 \cdot 12$ points, respectively. The Compton profiles have been calculated for the [100], the [110] and the [111] direction and averaged over all directions to account for the polycrystalline structure and the cubic symmetries of the studied samples [Tse2006].

Polycrystalline silicon

In figure (4.12) the experimental Compton profile of polycrystalline silicon is plotted together with the Hartree-Fock Compton profile of the core electrons. Exemplarily, only the measured Compton profile for setup A is presented. The spectra are in good agreement for $|p_z| > 2$ a.u. For $|p_z| < 2$ a.u. the contribution of the valence electrons is obvious. After subtracting the Hartree-Fock Compton profile from the experimental data, the resulting Compton profile of the silicon valence electrons is compared with calculated Compton profiles in figure (4.13) for both setups. To verify the experimental and theoretical results of this work, the spectra are plotted together with

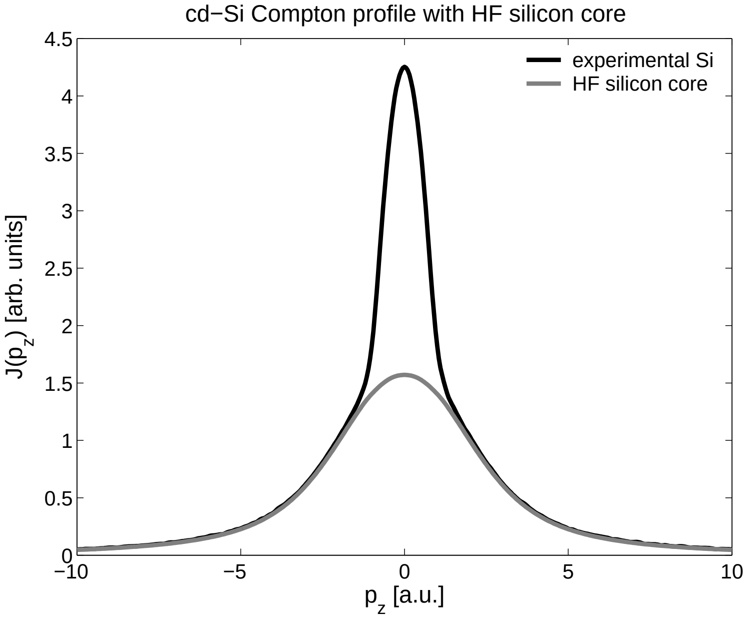

Figure 4.12: *Experimental silicon Compton profile (solid black line) plotted with the Hartree-Fock Compton profile of the core electrons (solid grey line).*

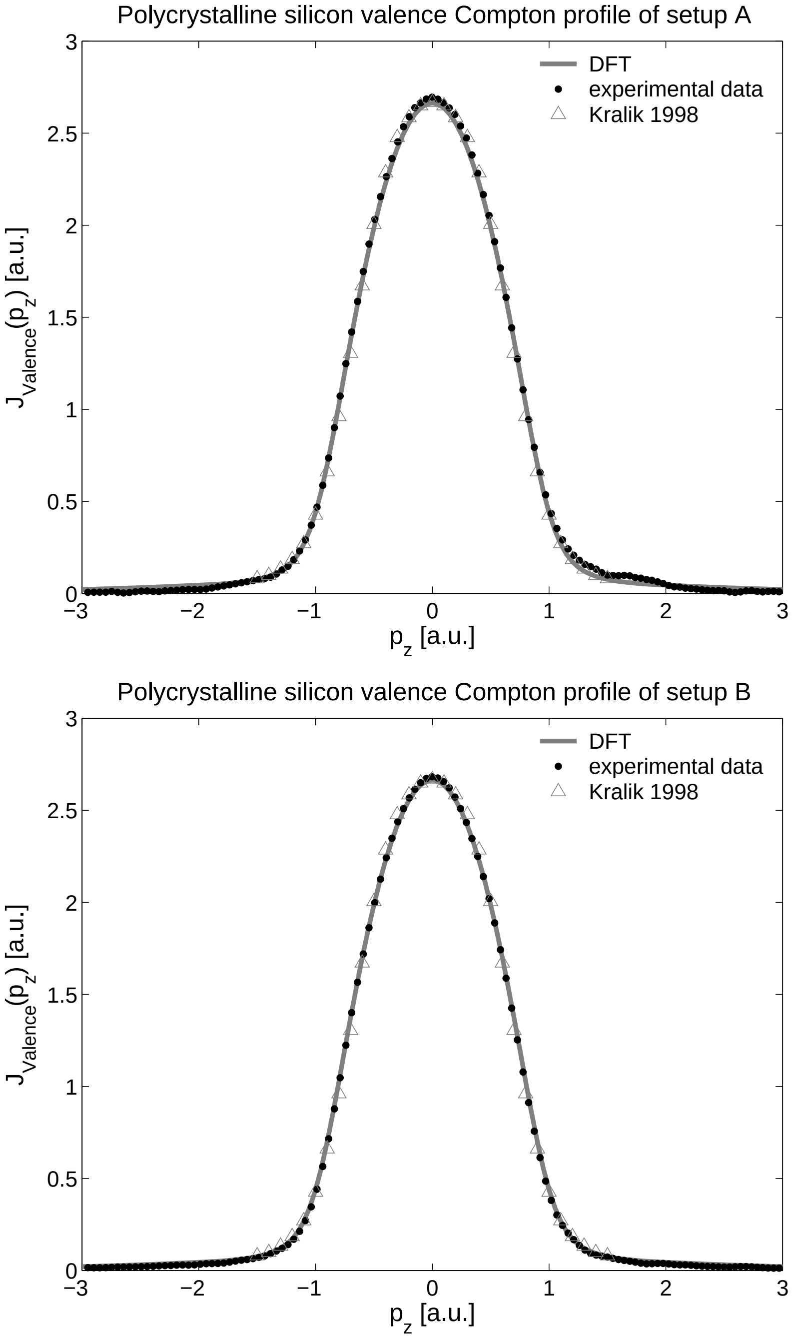
Polycrystalline silicon valence Compton profile of setup A

Polycrystalline silicon valence Compton profile of setup B

Figure 4.13: *Valence Compton profile of silicon (dotted) compared with DFT calculated Compton profiles of polycrystalline silicon (solid grey line), and digitalized DFT-LDA calculated Compton profiles of Kralik et. al (open triangles)* [Kralik1998]. *The results are presented for setup A (top) and setup B (bottom). The point size is chosen to reflect the statistical error of the experimental data, the open triangles emphasize the uncertainty of the digitalization procedure.*

formerly published DFT calculations of silicon for the [100] direction, which has been digitalized from the paper of Kralik *et al.* [KRALIK1998]. The point size is chosen to reflect the statistical error of the experimental data, the open triangles emphasize the uncertainty of the digitalization procedure. The spectra show an overall good agreement with the experimental data. The Compton peak is slightly underestimated by the theory and still contributes to the overall Compton profile for $p_z > 2$ a.u., while the broadness and the shape of all three spectra are the same. At 1.8 a.u. for setup A the experimental data shows a small feature. Therefore, only the negative p_z-range of the spectrum is discussed for further analysis because here concordant results are obtained for setup A and setup B measurements.

The empty-caged structure II silicon clathrate

A Rietfield analysis of the diffraction pattern measured in the course of the experiment yields a 4% content of crystalline silicon in the sample and was corrected for. The diffraction pattern together with the subtraction process can be found in appendix A.

In figure (4.14) the measured Compton profile of the empty-caged structure II silicon clathrate is depicted together with the contribution of the core electrons calculated in the Hartree-Fock approximation. Exemplarily, only the measured profile for setup A is presented. The good agreement with the experimental data underlines

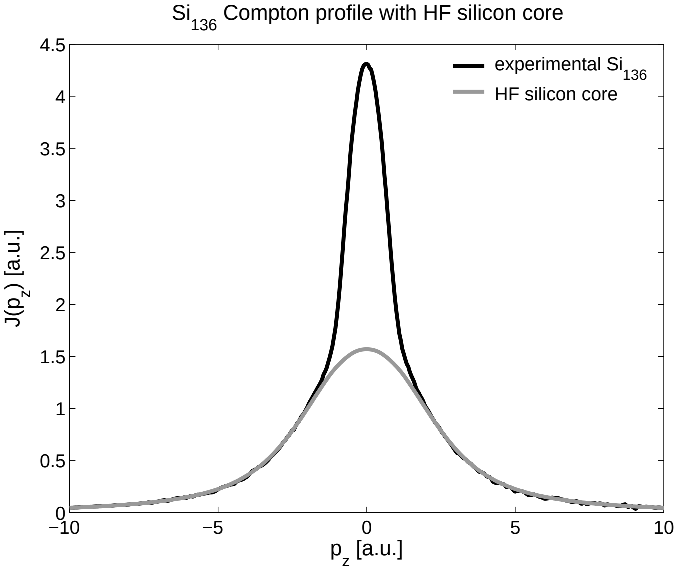

Figure 4.14: *Experimental Si_{136} Compton profile (solid black line) plotted with the Hartree-Fock core Compton profile of silicon (solid grey line).*

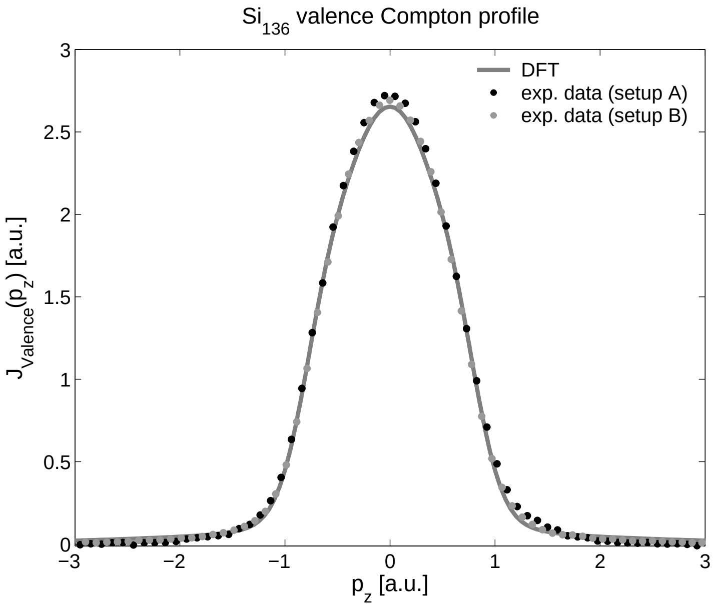

Figure 4.15: *Extracted valence Compton profile of* Si_{136}. *The results for setup A (black dotted) and setup B (grey dotted) are compared with DFT calculated Compton profiles (solid dark grey line).*

the quality of the Hartree-Fock Compton profiles regarding the contributions of the core electrons. The valence Compton profiles of Si_{136} for both setups are extracted and presented together with DFT calculated profiles in figure (4.15). A good overall agreement of shape and broadness regarding theory and experiment is apparent but is improved for the measurements of setup B. Again the calculated spectra show a stronger contribution for $|p_z| > 2$ a.u. if compared to the experiment. This results in an underestimation of the Compton peak by the DFT calculations with respect to the experimental data.

The Compton profile difference of polycrystalline silicon and Si_{136}

In summary the overall agreement of theoretically calculated Compton profiles with the experimental data is good. Finally, a comparison of the Compton profile difference of diamond phase silicon and Si_{136} will give an estimate of the error made by subtracting the reference profile from the alkali-metal doped silicon clathrates instead of using a Si_{46} reference. In figure (4.16 [a]) the difference profile is plotted for the experimentally obtained spectra of setup A (circles), setup B (triangles) and DFT calculated ones (solid grey line). For reasons of comparability only every second point

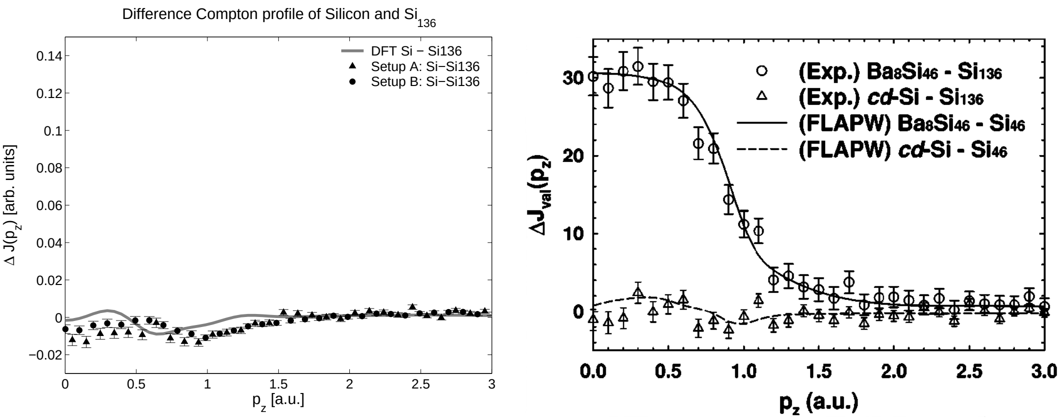

(a) (b)

Figure 4.16: *Difference spectra of silicon and silicon clathrate: In figure (a) the difference Compton profile of cd-Si and* Si_{136} *is plotted both for the experimental results of setup A (triangles), setup B (circles), and the calculated Compon profiles (solid grey line). In figure (b) the experimentally obtained difference profile (open triangles) and the calculated profile (dashed line) are plotted together with the experimental (open circles) and theoretical difference of the superconducting* Ba_8Si_{46} *and the empty-caged clathrate* Si_{46} *(solid black line)* [Itou2005].

of the experiment is depicted. Additionally, the depicted points are chosen not to overlap each other. The difference spectra are normalized to the Compton peak value of the experimentally obtained Si_{136} Compton profile of setup B. The axes of the figure are scaled to match the scaling of figure (4.16 [b]). While up to 1.5 a.u. the difference profiles of theory and experiment are differing in shape, they are converging to zero for higher p_z values.

In figure (4.16 [b]) the results of Itou *et al.* are plotted [Itou2005]. The open triangles are again representing the experimental difference profile, while the dashed line depicts the calculated difference profile of cd-Si and Si_{46}. Starting at 0.3 a.u., the theoretical predictions are matching the experimental data, while at low p_z a systematic deviation between theory and experiment can be observed. Thus FLAPW (Full potential linearized augmented plane wave) calculations of the Compton profile difference between cd-Si and Si_{136} give a better agreement of experiment and theory. Especially the minimum around $p_z = 1$ a.u. is reproduced correctly. However, the experimental result especially matches with the results presented in this work and the maximum difference of the measured Compton profiles of the reference materials is found to be at 1 % of the Compton peak. Due to the small deviations between the polycrystalline silicon and the Si_{136} clathrate the Compton profile of the empty caged silicon clathrate is evidenced to be a good reference for the further analysis of the alkali-metal doped silicon clathrates.

4.3.2 Alkali-metal doped silicon clathrates

In the following the Compton profiles of the alkali-metal guest atoms in the clathrates are extracted by subtracting the Si_{136} Compton profile from the given spectra. As in chapter (4.3), the obtained profiles are first compared to the corresponding Hartree-Fock core Compton profile of the alkali-metal, which is normalized with respect to the ratio of guest atoms per silicon atom.

Valence electron contribution of sodium in Na_8Si_{46}

Samples of Na_8Si_{46} could be provided only with a crystalline silicon content of 28.5 %, which was verified by a Rietveld analysis of the corresponding diffraction pattern. The procedure for subtracting the silicon contribution from the spectrum is detailed in appendix A. The Rietveld analysis further confirms the full occupancy of the silicon cages to $x = 8$. In figure (4.17) the experimental difference Compton profile between Na_8Si_{46} and Si_{136} (solid black line) is compared with a Hartee-Fock core Compton profile of free atomic sodium (solid grey line). The latter is multiplied by a factor of 8/46, the ratio between sodium and silicon in the sample. Additionally, the Compton profile difference of the reference samples is again depicted to give an estimate of the error made by subtracting the alternative reference Compton profile.

The deviations of the difference spectrum and the corresponding Hartree-Fock core Compton profile show an unusual behaviour. The experimental profile is overestimated by the Hartree-Fock calculations between 1.8 a.u. and 5.5 a.u. It is expected that the Hartree-Fock core Compton profile matches the experimental Compton profile at least for $|p_z| \geq 2$ a.u. In this range the valence Compton profile shows only marginal contributions to the total Compton profile and the core electron contribution has to be well predicted by the Hartree-Fock theory [Cooper2004]. Thus the deviations depicted in figure (4.17) are an indication to an additional contribution to the Compton profile, which is not accounted for so far.

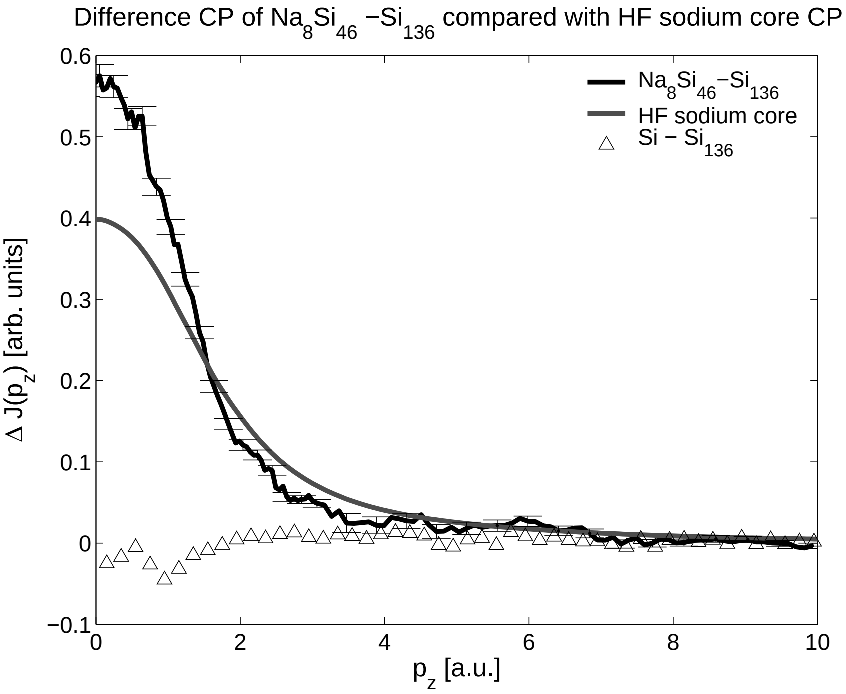

Figure 4.17: *The difference profile of* Na_8Si_{46} *(solid black line) is plotted together with a free atomic Hartree-Fock core Compton profile of sodium (solid grey line) and the difference profile of silicon and* Si_{136} *(open triangles). The errorbars are depicted for every fourth point.*

Valence electron contribution of potassium in K_8Si_{46}

The Rietveld analysis for the K_8Si_{46} sample yields no contribution of cd-Si impurities (see appendix A). The occupation number of the clathrate was determined to $x = 7.6$ by the same analysis. In figure (4.18) the experimental difference Compton profile of K_8Si_{46} and Si_{136} (solid black line) is compared with a Hartee-Fock core Compton profile of free atomic potassium (solid grey line). According to the Rietveld analysis, the Hartree-Fock core Compton profile is weighted by a factor of 7.6/46. Again the estimated contribution of the core electrons of the alkali-metal guest does not match the experimental data. Between 1.8 a.u. and 5 a.u. the values of the calculations are overestimating the experimental results. As in the Na_8Si_{46} compound, an additional contribution not yet accounted for could lead to such a result.

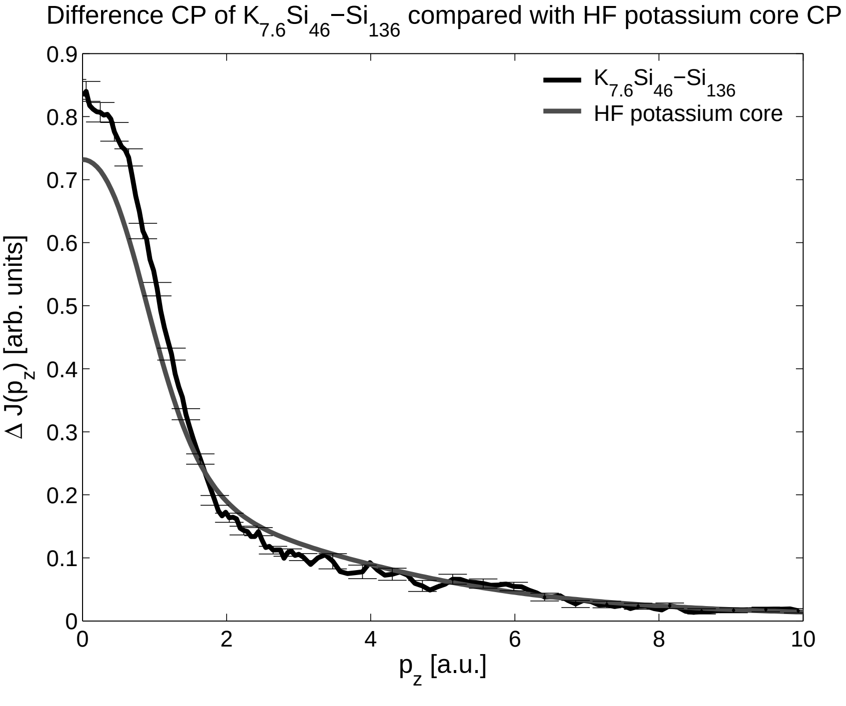

Figure 4.18: *The difference profile of $K_{7.6}Si_{46}$ and Si_{136} (solid black line) is plotted together with a free atomic Hartree-Fock core Compton profile of potassium (solid grey line). The errorbars of the difference spectrum are depicted for every fourth point.*

Direct difference of $K_{7.6}Si_{46}$ and Na_8Si_{46}

To further analyse the spectra, direct differences of $K_{7.6}Si_{46}$ and Na_8Si_{46} are compared with the corresponding difference of the DFT calculations. In figure (4.19) the direct difference between Na_8Si_{46} and $K_{7.6}Si_{46}$ is plotted for the experimental (dots) and the theoretical results (solid grey line). Within the limits of the experimental resolution the spectra are equivalent in shape broadness and absolute values. As a result, the deviations found above are canceled out to great extend if direct differences of the Compton profiles are compared. Therefore, the systematic errors most probably have the same origin and are of the same order of magnitude.

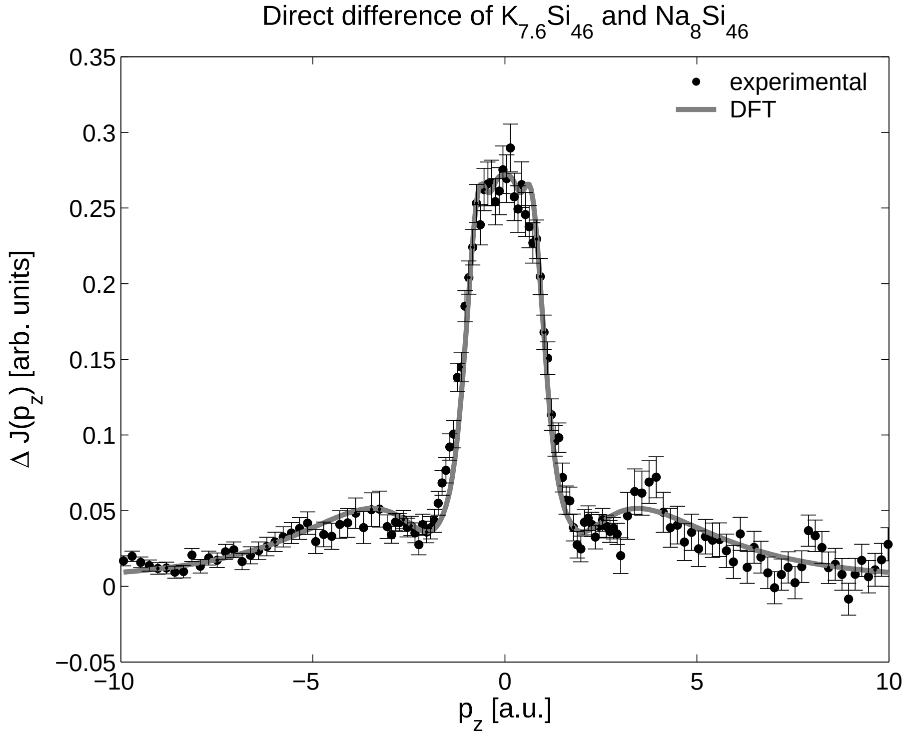

Figure 4.19: *The Direct difference of* $K_{7.6}Si_{46}$ *and* Na_8Si_{46} *is plotted for both the DFT results (solid grey line) and the experimental results (dots) with the according errorbars.*

4.4 Amorphous silicon dioxide in $K_{7.6}Si_{46}$ and Na_8Si_{46}

In summary the spectra of the diamond phase silicon and the empty-caged structure II silicon clathrate are in good agreement with theoretical predictions while the difference Compton profiles of sodium and potassium doped silicon clathrates show systematic errors. Both digested spectra disagree with the Hartree-Fock calculations between 2 a.u. to 5 a.u., where a good agreement has to be expected. As already mentioned in section (3.2), amorphous silicon oxides are often found in clathrate compounds [Gryko2000, Ammar2004]. Especially He *et al.* [He2001] found an at least 50 Å layer of amorphous silicon dioxide at the surface of the powdered samples. As an amorphous material is difficult to be detected in a diffraction pattern, the silicon L-edges of silicon clathrates and amorphous silicon oxides have been analyzed using the bulk sensitive non resonant x-ray Raman scattering technique (NRIXS). The results suggest a significant amount of amorphous silicon dioxide in the given samples. A survey of the theoretical background and the experimental setup of the measurements are given below. This is followed by the description of a computational scheme to digest the SiO_2 amount in the samples from the original Compton scattering results in section (4.4.2).

4.4.1 X-ray Raman scattering at the silicon L-edge of alkali-metal doped silicon clathrates

X-ray Raman scattering (XRS) also referred to as non-resonant inelastic x-ray scattering is an experimental tool, which offers to measure absorption edges of low Z materials using hard x-rays. In the so-called dipole limit it is equivalent to classical absorption spectroscopy, while by using large momentum transfers q it will even give information about multipole transitions of the electron system [Sternemann2003]. By the use of hard x-rays, many of the experimental difficulties are negligible if compared to electron energy loss spectroscopy or absorption spectroscopy. For example the XRS is volume sensitive and thus is hardly depending on the surface preperation of the given samples. This is of special importance because the Compton scattering technique is also bulk sensitive. Thus, a surface sensitive technique like photon absorption spectroscopy would not provide an adequate analysis of the samples. In general, the lowered requirements to the sample and the sample environment opens new fields of absorption edge spectroscopy for example for liquid systems or high pressure research. Before describing the experimental setup and presenting the results of the XRS measurements on silicon clathrates, a very brief introduction of the theoretical background is discussed.

Non-resonant x-ray Raman scattering

For a theoretical and experimental description of non-resonant x-ray Raman scattering it is necessary to go back to equation (1.6):

$$\frac{d^2\sigma}{d\Omega d\omega_2} = r_0^2 \left(\vec{\epsilon}_1 \cdot \vec{\epsilon}_2\right)^2 \left(\frac{\omega_2}{\omega_1}\right) \sum_{i,f} \left| \left\langle f \middle| \sum_j e^{i\vec{q}\cdot\vec{r}_j} \middle| i \right\rangle \right|^2 \delta\left(E_f - E_i - \omega\right) .$$

By expanding the exponential

$$e^{-i\vec{q}\cdot\vec{r}} = 1 + i\vec{q}\cdot\vec{r} - \frac{\left(\vec{q}\cdot\vec{r}\right)^2}{2} - \ldots , \tag{4.10}$$

it is evident, that for $q \cdot r \ll 1$ the contributions of the quadratic term and higher order terms become negligible. In the late 1960s Mizuno and Ohmura [Mizuno1967] already calculated the excitation of a core electron in a ground state $|0\rangle$ with an energy E_0 and a one-electron Bloch-state $\left|\vec{k}\right\rangle$ with energy $E_{\vec{k}}$ to

$$S\left(\vec{q}, \omega\right) = \vec{q} \cdot T(\omega) \cdot \vec{q} \tag{4.11}$$

with

$$T(\omega) = \sum_{\vec{k}} \left| \left\langle \vec{k} \left| \vec{r} \right| 0 \right\rangle \right|^2 \cdot \delta\left(E_{\vec{k}} - E_0 - \hbar\omega\right) . \tag{4.12}$$

Here the δ-function gives rise to an edge-like structure. Starting with an energy transfer $\hbar\omega = E_0$ the excitation of a core electron becomes possible and with rising energy transfer the unoccupied electron density of states is tested. Similar to the traditional absorption spectroscopy, the method is able to gather information about the unoccupied density of states of the electrons. Mizuno and Ohmura could further show, that the cross-section of absorption spectroscopy is determined by the same matrix elements $T(\omega)$ if compared with the dipole limit of the NRIXS cross-section:

$$\sigma(\omega) = 4\pi^2 e^2 \omega \vec{\epsilon} \cdot T(\omega) \cdot \vec{\epsilon}. \tag{4.13}$$

Overall the shape of the x-ray Raman spectra is similar to the absorption edges of traditional absorption spectroscopy as long as $q \cdot r \ll 1$. The multipole transitions are observable for momentum transfers with $q \cdot r \geq 1$.

X-ray Raman scattering at beamline ID16, ESRF

Measurements of the silicon $L_{II,III}$-edge using the XRS technique were performed at beamline ID16 of the ESRF. The incident beam of the undulator beamline was monochromatized by a Si(555) analyzer crystal to an incident energy of 9.89 keV. The energy loss spectra at the Si $L_{II,III}$-edge were measured for Si,Si_{136}, Na_8Si_{46} and $K_{7.6}Si_{46}$. Although the samples were prepared from the same charge they are not identical with the samples used for the previous Compton scattering experiment. At a fixed analyzer energy of the Rowland type spectrometer the incident energy has been varied accordingly. The samples were pressed into sample holders enabling both transmission and reflection geometry and leading to a momentum transfer q of 1.2 a.u. and 5.17 a.u., respectively. The energy resolution was determined by the FWHM of the Rayleigh line to 0.9 eV for the low momentum transfer and to 1.5 eV for the high momentum transfer case.

After correcting the spectra for background, energy dependent absorption and the scattering cross section the valence electron contributions to the XRS spectra are corrected for. For the low momentum transfer the plasmon tail is fitted by a Pearson function and for the backscattering geometry the corresponding valence Compton profile contribution was found to be negligible. For details refer to Sternemann *et al.* [STERNEMANN2005].

Results and discussion

The edge structures of the alkali-metal doped silicon clathrates (Na_8Si_{46}, $K_{7.6}Si_{46}$) show distinct features at about 108 eV energy transfer. In figure (4.20) the silicon $L_{II,III}$-edge of Na_8Si_{46}, $K_{7.6}Si_{46}$ and Si are compared to photo absorption spectra of amorphous SiO_2 measured by Li *et al.* [Li1994]. The x-ray Raman spectra are depicted for a low momentum transfer to account for the dipole allowed transitions in the photo absorption spectroscopy and the feature related to SiO_2 is marked by an arrow. Especially the spectrum of $K_{7.6}Si_{46}$ shows a strong peak at the given position while the feature is weaker for the Na_8Si_{46} sample. The silicon sample does not show any structure at all. It is evident that the observed peaks are similar in shape and structure to the chemically shifted $L_{II,III}$-edges of the silicon dioxide sample. To underline these results, the difference spectra of Na_8Si_{46} and $K_{7.6}Si_{46}$ with Si_{136} are plotted together with the $Si0_2$ spectrum in figure (4.21).

In order to have a first estimate of the SiO_2 content in the samples, the silicon $L_{II,III}$ edge of the given clathrate is simulated by a best fit of the Si L-edge of the given clathrate. The shape of the L-edge and the position of the peak at 108 eV is reproduced accurately and the results are displayed in figure (4.22). They give an

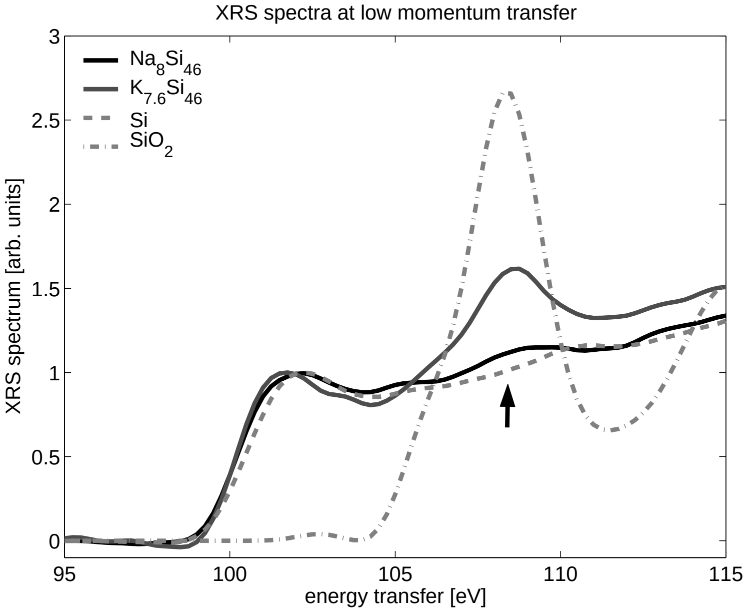

Figure 4.20: *Si L-edges of crystalline silicon (dashed grey line), Na_8Si_{46}(solid black line), $K_{7.6}Si_{46}$(solid dark grey line), and SiO_2 (dashed dotted grey line) for low momentum transfer q.*

amorphous SiO_2 content of about 3.3 % in Na_8Si_{46} and 18.6 % in $K_{7.6}Si_{46}$.

In summary the features of the XRS spectra strongly suggest a significant amount of silicon dioxide in Na_8Si_{46} and $K_{7.6}Si_{46}$. Though the fitting procedure is not suited to give an exact ratio of the SiO_2 content, the results show that the silicon dioxide content is unlikely to originate from mere surface oxidation of the clathrate powder. The average grain size of a clathrate sample is about 2 μm. By assuming a spherical grain with radius $r = 1\,\mu$m even a silicon dioxide content of 2 % would result in an oxide layer of about 7 nm. But the oxide layer in a silicon clathrate is usually about 5 nm [Qiu2001]. Due to the highly focused beam of 50 μm · 50 μm, only a local picture of the overall sample is deduced and might vary with the position on the sample. Therefore, the absolute values of the fitting procedure have to be interpreted carefully. Still, they provide evidence of a significant amount of amorphous SiO_2 in the samples.

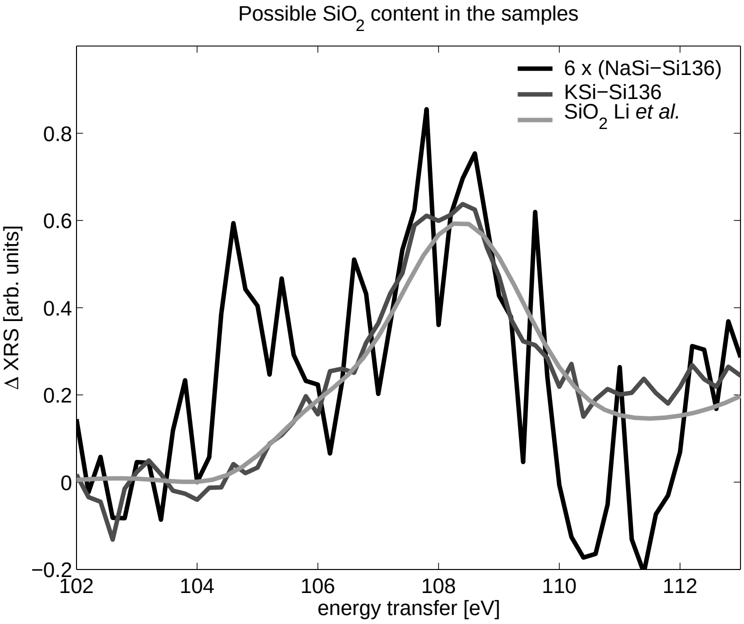

Figure 4.21: *The difference spectra of Na_8Si_{46} (solid black line) and $K_{7.6}Si_{46}$ with Si_{136} (solid dark grey line) and the spectrum of the Si $L_{II,III}$-edge of the amorphous SiO_2 (solid grey line) are presented. As a guide to the eye, the measuring points are connected with lines and the difference spectrum for the sodium clathrate sample is magnified by a factor of six.*

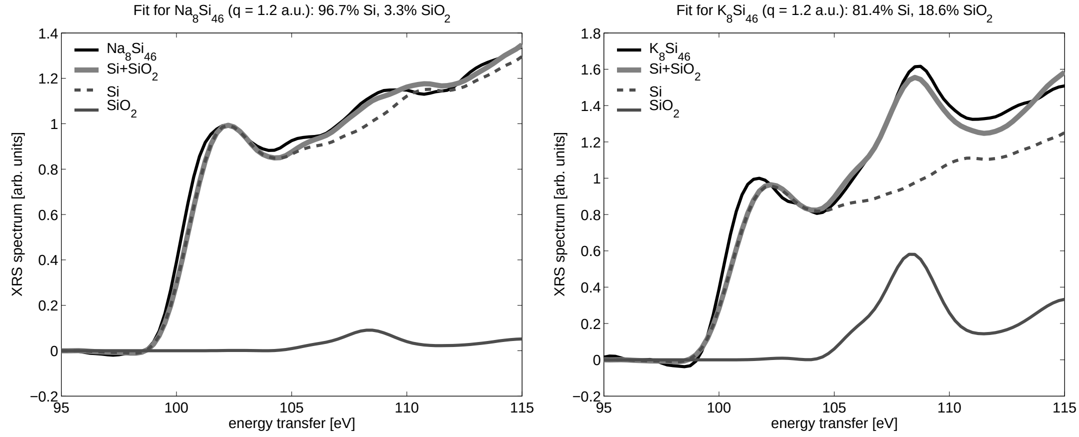

(a) (b)

Figure 4.22: *SiO_2 content in Na_8Si_{46} (a) and $K_{7.6}Si_{46}$ (b) for momentum transfer $q = 1.2$ a.u. The corresponding Si L edge of the given clathrate (solid black line) is compared with the L-edges of diamond phase silicon (dashed dark grey line) and SiO_2 (solid dark grey line). The solid grey line shows a best fit of the L-edge by a silicon sample with SiO_2 content. The spectra are scaled to match their spectral weight.*

4.4.2 Determination of the SiO_2 contribution to the measured Compton profiles

For determining the SiO_2 content in Na_8Si_{46} and $K_{7.6}Si_{46}$ a hypothetical Compton profile $J_{\mathrm{hyp}}(p_z)$ is fitted to the experimentally obtained spectrum.

$$J_{\mathrm{hyp}}(p_z) = \left(J^{\mathrm{exp}}_{\mathrm{Si/Si_{136}}} + J^{\mathrm{HF}}_{\mathrm{Na,K}}\right) + n_{\mathrm{SiO_2}} \cdot J^{\mathrm{exp}}_{\mathrm{SiO_2}} + n_{\mathrm{Si}} \cdot J^{\mathrm{exp}}_{\mathrm{Si}} \tag{4.14}$$

It is composed of the experimental Compton profiles of Si_{136} or polycrystalline silicon $J^{\mathrm{exp}}_{\mathrm{Si/Si_{136}}}$, the core Compton profile of the given guest atom (Hartree-Fock) $J^{\mathrm{HF}}_{\mathrm{Na,K}}$ and a variable SiO_2 component $n_{\mathrm{SiO_2}} \cdot J^{\mathrm{exp}}_{\mathrm{SiO_2}}$. In case of the sodium doped structure I clathrate, the crystalline silicon content of $n_{\mathrm{Si}} = 28.5$ % is also accounted for. As a SiO_2 reference the measured Compton profile of amorphous SiO_2 of setup B is used. The SiO_2 content of the samples is fitted by a least square algorythm on a p_z-range of -10 a.u. to 10 a.u. The valence regime ranging from -3 a.u. to 3 a.u. of the Compton profile is excluded from the fit because $J_{\mathrm{hyp}}(p_z)$ is only a good approximation of the

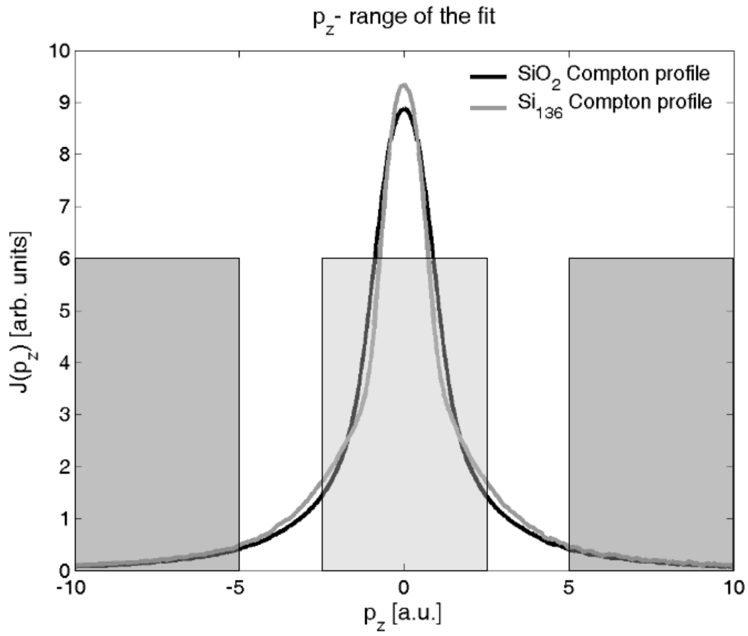

Figure 4.23: *Variation of the p_z-range of the SiO_2 fitting procedure. The brightly shaded area around $p_z = 0$ marks the valence regime of the Compton profile. The darker shaded areas with $|p_z| > 5$ a.u. emphasize the regions where the Compton profiles of silicon and silicon dioxide do have the same shape. The p_z-range of the fitting procedure is varied symmetrically around $p_z = 0$ a.u. in between the unshaded areas of the plot.*

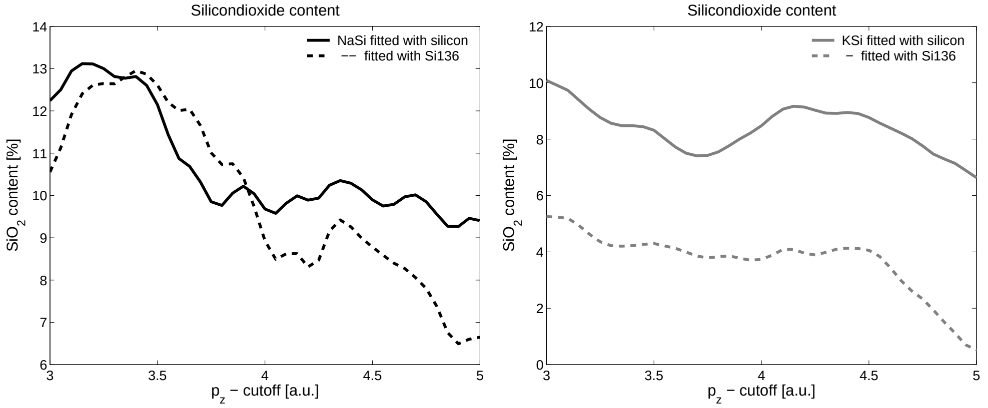

(a) (b)

Figure 4.24: *Estimated SiO_2 content in the clathrate samples. The solid lines are representing the results for the polycrystalline silicon reference and the dashed lines the results for the empty caged silicon clathrate reference.*

core electron contribution to the Compton profile. Therefore, the fitting procedure does not include the valence Compton profile regime of the experiment, which is the region of interest in this study. In figure (4.24), the experimental Compton profiles of silicon dioxide and the empty caged silicon clathrate are presented. Both spectra are normalized to the same area under the Compton profile to be able to compare their difference in shape. For $|p_z| > 5$ a.u. the silicon and the silicon dioxide Compton profiles are matching in shape. Therefore, the excluded area (p_z-cutoff) should be smaller than $|p_z| = 5$ a.u. as this would lead to an underestimation of the SiO_2 content. In figure (4.24) the resulting SiO_2 contents are presented as a function of the excluded p_z-range of the algorythm. The values are varying from 7 to 13 % in case of the Na_8Si_{46} sample and from 4 to 10 % in case of the $K_{7.6}Si_{46}$ sample. Again, this procedure gives only an estimate of the real silicon dioxide in the samples as can be evidenced by the differing results for either the silicon or the silicon clathrate reference in case of the $K_{7.6}Si_{46}$ sample. Therefore, mean values of the SiO_2 content of 9.5 % for Na_8Si_{46} and 6.5 % for $K_{7.6}Si_{46}$ are used for the further analysis of the Compton profiles. The subtracting procedure is detailed in appendix A. The resulting spectra are depicted in figure (4.25) and are compared with Hartree-Fock core Compton profiles of the corresponding guest atoms. Both spectra show an overall agreement with the Hartree-Fock Compton profiles within the errorbars for $|p_z| = 2$ a.u. Finally, the valence contribution of the alkali-metal guest atoms is digested by subtracting the Hartree-Fock spectra from the data. The results are presented in figure (4.26).

Difference CP of Na_8Si_{46} and Si_{136} compared with a HF sodium core CP

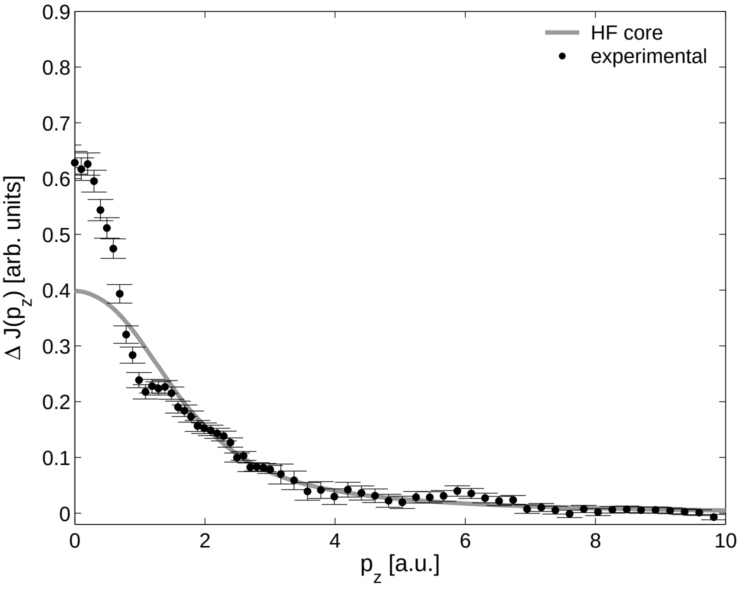

Difference CP of $K_{7.6}Si_{46}$ and Si_{136} compared with a HF potassium core CP

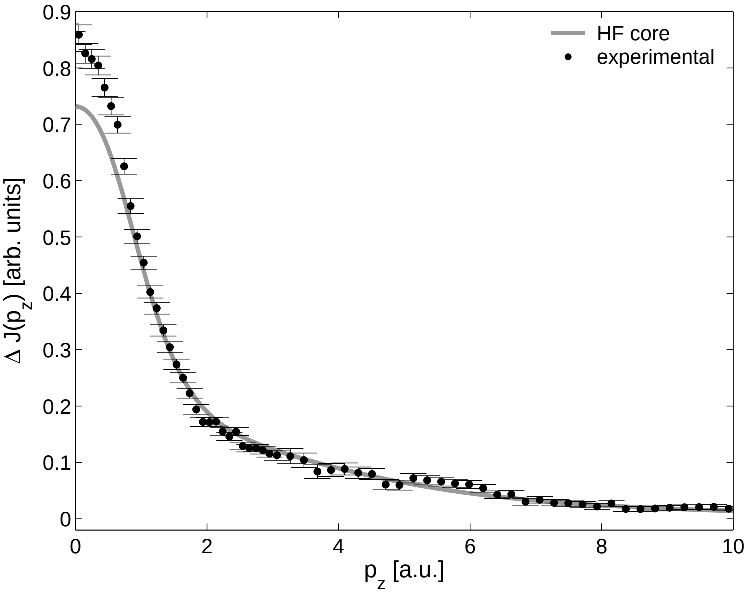

Figure 4.25: *The difference profile of* Na_8Si_{46} *(top) and* $K_{7.6}Si_{46}$ *(bottom) with* Si_{136} *(solid black lines) after correcting for the* SiO_2 *content are plotted together with their corresponding free atomic Hartree-Fock core Compton profiles (solid grey line).*

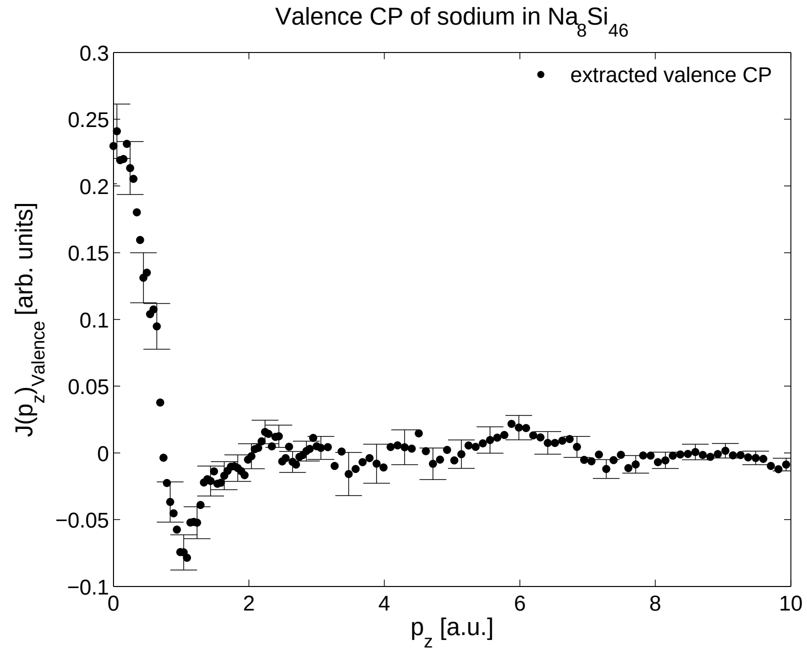

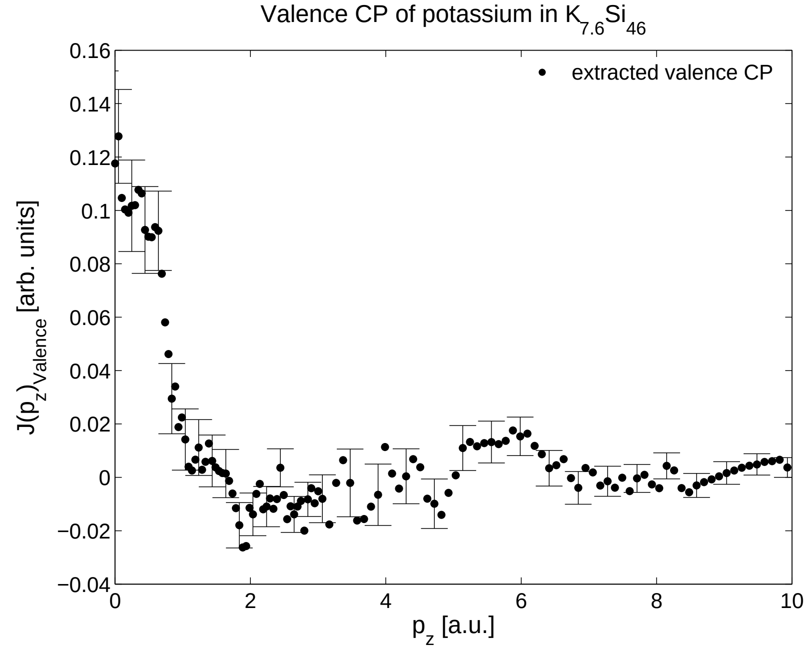

Figure 4.26: *Extracted valence Compton profiles of the alkali-metal guest atoms after all corrections. The contributions of the sodium atoms (top) and the potassium atoms (bottom) are depicted together with the errorbars. The errorbars are plotted examplarily for every fourth point only.*

Chapter 5

Interpretation of the extracted Compton profiles

An important factor for the different physical and chemical properties of differently doped silicon clathrates is the interaction of the valence electron of the guest atom with the silicon host lattice. Here, the charge transfer from the guest atom to the host lattice is of special interest and is discussed differently in the literature. While some authors find evidence for a very low charge transfer [Gryko1996, Pouchard2002] others claim a partial [Conesa 2004] or a nearly complete transfer [Moriguchi2000, Tse2000, Moewes2002]. Therefore, before discussing the interaction on the basis of the DFT calculations in section (5.2), the digested Compton profiles are compared with Hartree-Fock calculated valence Compton profiles of free atomic sodium and potassium (5.1).

5.1 The alkali-metal guest as a free atom

As already suggested by Cros *et al.* [Cros1970], especially nuclear magnetic resonance measurements were interpreted by Gryko *et al.* [Gryko1996] by assuming nearly neutral alkali-metal guest atoms. In figure (5.1) the extracted contributions to the Compton profile of the valence electrons of sodium (lefthand side) and potassium (righthand side) are compared to Hartree-Fock valence Compton profiles of a hypothetically free atomic guest (solid grey lines). The Hartree-Fock Compton profiles are multiplied by a factor of 8/46 for the sodium clathrate and 7.6/46 for the potassium clathrate according to the corresponding occupation numbers. The strong deviation of the experimental spectra to the calculations in both cases is evident. The Hartree-

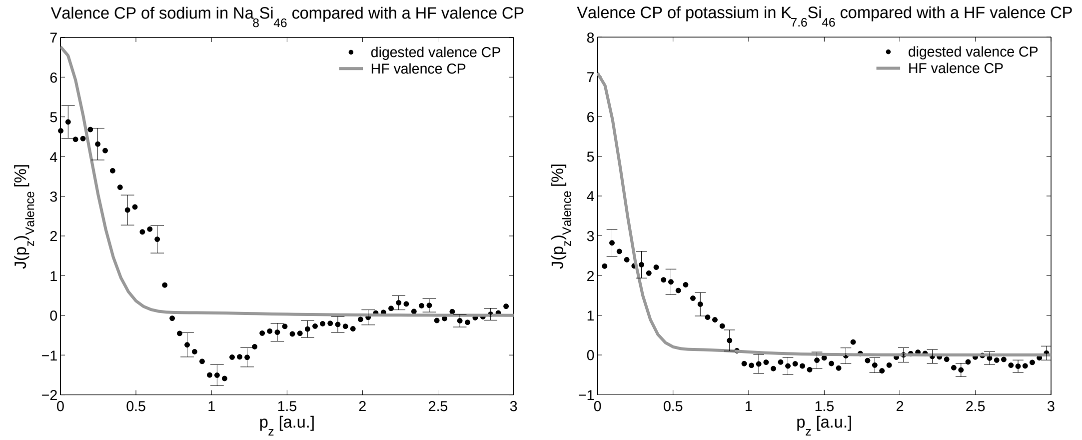

(a) (b)

Figure 5.1: *Extracted valence Compton profiles of the alkali-metal guest atoms (dots) compared with Hartree-Fock calculations (solid grey line) for free atomic sodium (a) and potassium (b). The errorbars are plotted examplarily for every fourth point only.*

Fock spectra are showing a narrow valence Compton profile with a sharp break at about 0.5 a.u. and a smooth Compton peak with no apparent additional features. In contrast to that, both experimental spectra show a sharp break at 1 a.u. although they change in slope at about 0.5 a.u. In conclusion, the experimental results disagree strongly with a free atomic model of nearly neutral alkali-metal guest atoms. This is underlined by the results of He *et al.* [HE2001] who in contrast to Gryko *et al.* [GRYKO1996] interpreted the NMR spectra in terms of a charge transfer of the 3s electrons of the sodium to the silicon host. Therefore, the trapped alkali-metal guest

non-equivalent positions	Distance [Å]
Na(1)-Si(2)	3.263
Na(1)-Si(3)	3.369
Na(2)-Si(1)	3.606
Na(2)-Si(2)	3.786
Na(2)-Si(3)	3.425, 3.948

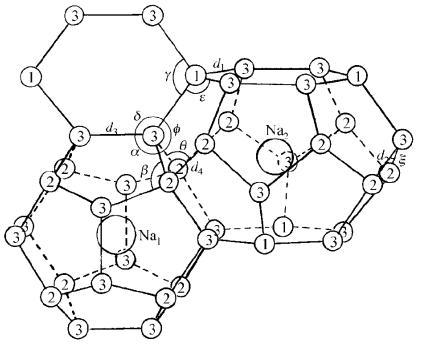

Figure 5.2: *Sodium-Silicon distances in structure I silicon clathrates. The numbers in parentheses correspond to the according numbers depicted for the Na_8Si_{46} structure* [RENY1998].

atom either shares a covalent bonding with the silicon atoms of the host lattice or is ionic in character.

As the trapped metal atoms are residing in the middle of the silicon cages their distance to the silicon atoms exceeds that of a covalent Na-Na bond in e.g. a sodium gas of 3.1 Å [TOURNUS2004] (see table [5.2]). Thus, a covalent bonding seems unlikely and the ionization of the alkali-metal guest atoms is the preferable model.

5.2 Comparison of the extracted Compton profiles with DFT spectra

In the following the extracted experimental valence contribution of the alkali-metal guest atoms are compared to DFT calculated spectra. The theoretical spectra are obtained by subtracting the DFT Compton profile of the empty caged silicon clathrate reference $J^{\mathrm{DFT}}_{Si_{136}}(p_z)$ and the Hartree-Fock core Compton profile of the corresponding guest atom $J^{\mathrm{HF}}_{\mathrm{Na,K}}(p_z)$ from the DFT Compton profile of the alkali-metal doped silicon clathrate $J^{\mathrm{DFT}}_{Na_8Si_{46},K_{7.6}Si_{46}}(p_z)$:

$$J^{\mathrm{theo}}_{\mathrm{valence}}(p_z) = J^{\mathrm{DFT}}_{Na_8Si_{46},K_{7.6}Si_{46}}(p_z) - J^{\mathrm{DFT}}_{Si_{136}}(p_z) - \frac{x}{46} \cdot J^{\mathrm{HF}}_{\mathrm{Na,K}}(p_z)\,. \tag{5.1}$$

Again x denotes the occupation number of the sodium or the potassium guest atoms.

5.2.1 Sodium doped silicon clathrate

In figure (5.3) the extracted experimental (dots) and theoretical (solid grey line) DFT valence Compton profiles of the sodium guest atoms are presented together with a Hartree-Fock valence Compton profile of sodium (dashed dark grey line) and a valence Compton profile of Si_{136} (solid dark grey line). The silicon valence electron Compton profile is normalized to the same area as the other spectra for reasons of comparability. The spectra are given as a fraction of the Compton profile maximum of the experimental $\mathrm{Na_8Si_{46}}$ sample. In general the experimental data and the DFT spectrum match within the errorbars, while small deviations can be detected for the Compton profile maximum and the p_z-regime ranging from 0.8 a.u. to 1.65 a.u. Above this p_z value no significant contributions of the valence electrons are apparent in both spectra. The underestimation of the minimum at 1 a.u. marked by the thick arrow lies within the experimental uncertainty of the $\mathrm{SiO_2}$ subtraction as discussed later (see figure [5.5]). Both, the experimental data and the DFT calculated Compton profile are broader than the Compton profile of Hartree-Fock sodium but are showing a narrower structure at 0.5 a.u. and is marked by the thin arrow. It is exactly the position of the onset of the Hartree-Fock valence Compton profile. This suggests a strong interaction between the guest atoms valence electrons and the silicon host lattice, which could be attributed to a partial charge transfer of the 3s electron of sodium to the silicon host and is discussed in section (5.3).

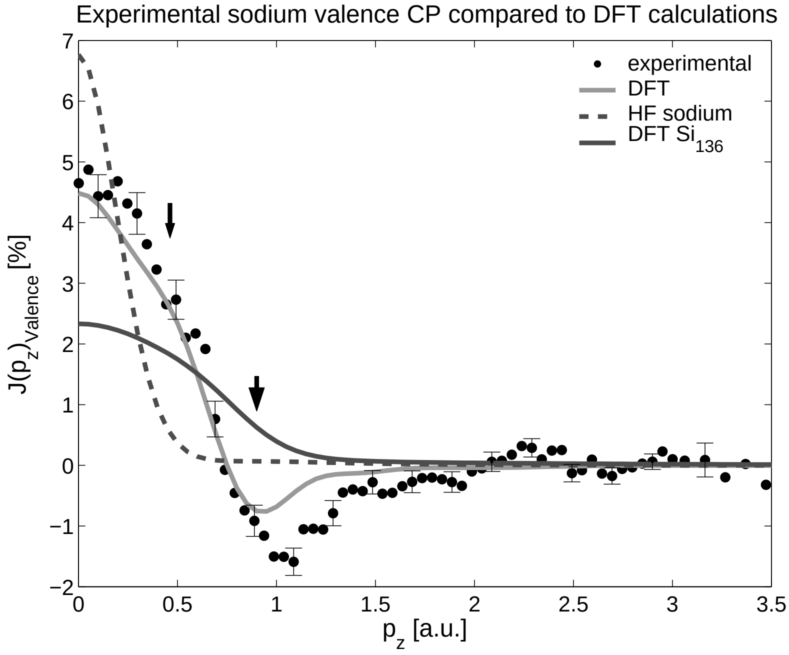

Figure 5.3: *Extracted valence Compton profiles of the sodium guest atoms (dots) compared with DFT calculations (solid grey line) and the Hartree-Fock valence Compton profile of a free sodium atom (dashed dark grey line). As a second reference a valence Compton profile of Si_{136} is depicted (solid dark grey line). The errorbars are plotted for every fourth point only.*

5.2.2 Potassium doped silicon clathrate

In figure (5.4) the extracted experimental (dots) and theoretical (solid grey line) DFT valence Compton profiles of the potassium guest atoms are presented together with a Hartree-Fock valence Compton profile of potassium (dashed dark grey line) and a valence Compton profile of Si_{136} (solid dark grey line). The silicon valence electron Compton profile is normalized as discussed in section 5.2.1. The spectra are given as a fraction of the Compton profile maximum of the experimental $K_{7.6}Si_{46}$ sample.

Within the resolution of the experiment the extracted Compton profile and the DFT spectrum are matching in shape and absolute values. Again, above $p_z = 1.65$ a.u. no significant contributions of the valence electrons to the total Compton profile are observed. Here, the minimum at 1 a.u. is predicted correctly by the DFT calulations (thick arrow). The narrow structure at 0.45 a.u. is more pronounced if compared with the results for the sodium doped silicon clathrate and shares the same p_z regime as the valence Compton profile of the Hartree-Fock potassium (thin arrow). Again, the shape of the experimental and DFT calculated spectra indicate a partial charge transfer of the 4s electron of potassium to the silicon host lattice if compared to the Hartree-Fock result and the DFT Compton profile for a Si_{136} valence electron. The charge transfer and aspects of hybridization are descussed in detail in section (5.3)

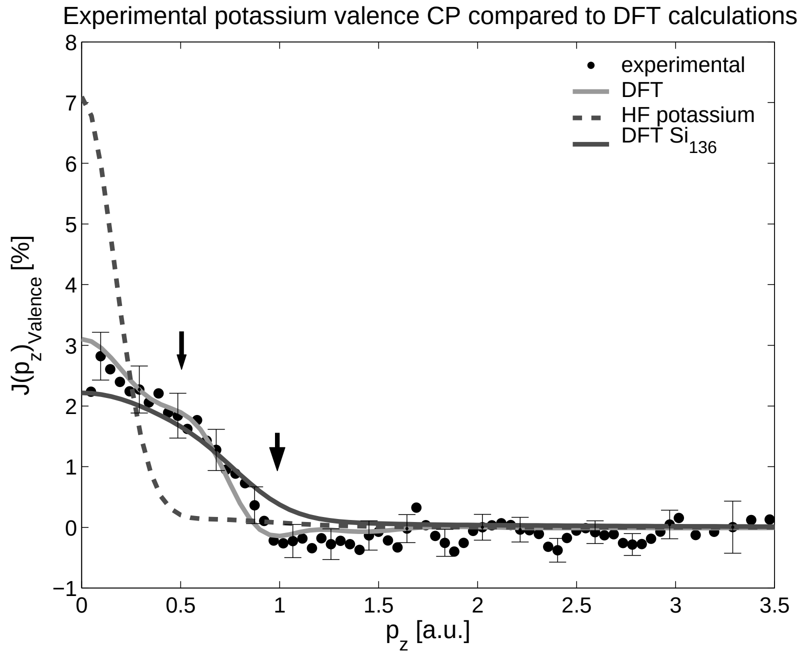

Figure 5.4: *Extracted valence Compton profiles of the potassium guest atoms (dots) compared with DFT calculations (solid grey line) and the Hartree-Fock valence Compton profile of free potassium atom (dashed dark grey line). As a second reference a valence Compton profile of* Si_{136} *is depicted (solid dark grey line). The errorbars are plotted examplarily for every fourth point only.*

5.2.3 Influence of the assumed SiO_2 content

As the evaluation process for determining the silicon dioxide content in the alkali-metal doped silicon clathrates gives only an estimate of the real SiO_2 content, the agreement of the DFT calculated Compton profiles with the experimental data should be tested for varying dioxide concentrations. To reflect for the uncertainty of the evaluation process, the SiO_2 content is varyied by ±2.5%. The resulting spectra for the sodium and the potassium doped silicon clathrate samples are depicted in figures (5.5 and 5.6) and are compared to the according DFT Compton profiles. The overall trend of the experimental spectra remains the same and the largest deviations can be observed around $p_z = 1$ a.u. In case of the Na_8Si_{46} clathrate an enhanced dioxide content even improves the agreement with the theoretical results (solid grey lines). Therefore, within the error limits of the SiO_2 content in the samples the experiment is well described by the presented DFT calulations.

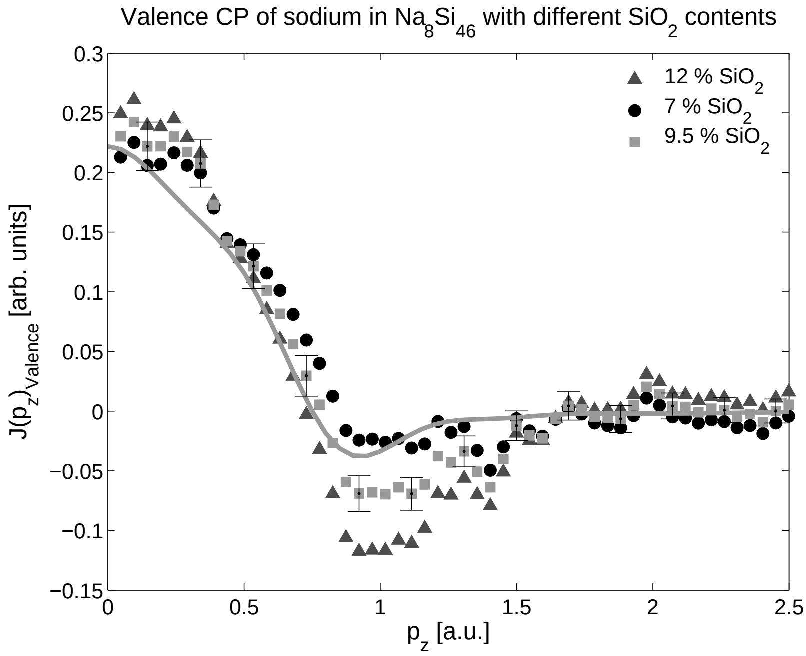

Figure 5.5: *Extracted valence Compton profiles of the sodium guest atoms with varying SiO_2 content (solid triangles, squares and circles) compared with DFT calculations (solid grey line). The errorbars are plotted examplarily for every fourth point only.*

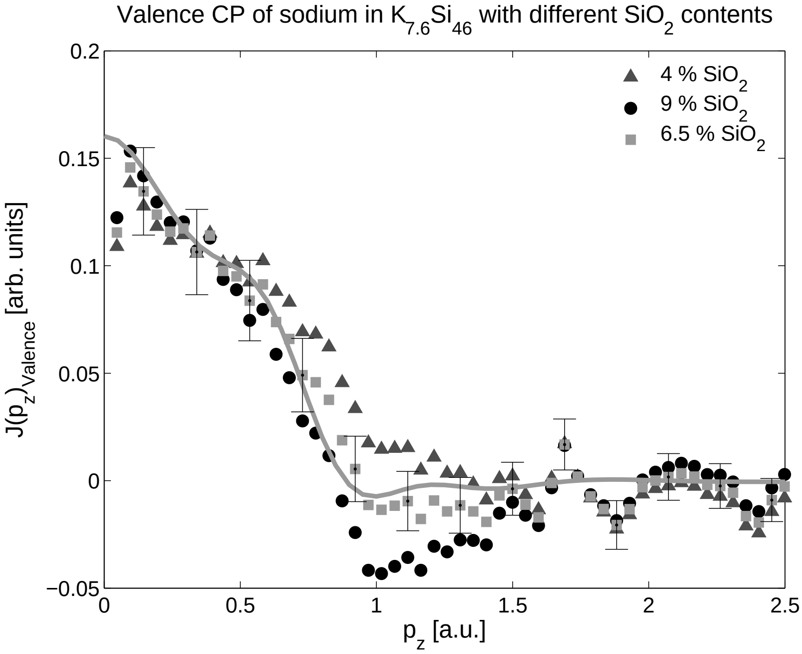

Figure 5.6: *Extracted valence Compton profiles of the potassium guest atoms with varying SiO_2 content (solid triangles, squares and circles) compared with DFT calculations (solid grey line). The errorbars are plotted examplarily for every fourth point only.*

5.2.4 Conclusions

The DFT calculated Compton profiles are in very good agreement with the experimentally obtained spectra. The shape of the extracted contributions of the valence Compton profiles of the alkali-metal guest atoms suggest a partial charge transfer to the silicon host lattice. Even varying the SiO_2 content strongly, the overall agreement of theory and experiment holds. Because the Compton profile is sensitive to changes of the wavefunctions it is a good test of the quality of the computational method and the basis set of wavefunctions used for the calculations [Eisenberger1972, Williams1977, Cooper2004].

Due to the results presented here a further discussion of charge transfer in clathrate compounds on the basis of the calculated wave functions is certainly justified and is presented in the following section.

5.3 Charge transfer

The very good predictions of the DFT calculations support a further analysis of the obtained theoretical results and are expanded to calculations of rubidium doped silicon clathrates. The electron density of states is calculated and analysed in section (5.3.1) and the charge transfer to the silicon host is estimated in section (5.3.2) using Mulliken population analysis [Mulliken1955, Mulliken1962].

5.3.1 Electron density of states

As a reference the electron density of states (DOS) of the empty caged structure I silicon host lattice is used for the comparison with the alkali-metal doped silicon clathrates. The DOS are calculated by the CRYSTAL code [Crystal2006] using a large $8 \cdot 8 \cdot 8$ k point set. The results are convoluted by a Gaussian function with a FWHM of 0.1 eV.

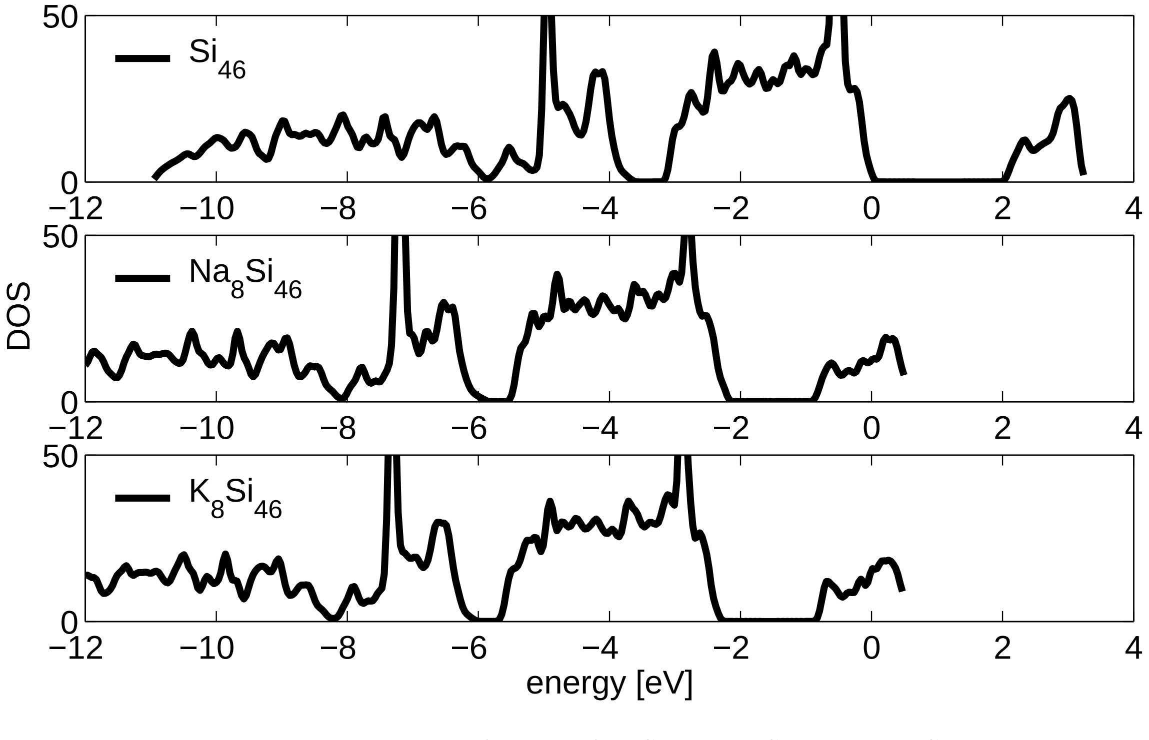

Figure 5.7: *Total electron density of states for* Si_{46}*,* Na_8Si_{46} *and* K_8Si_{46} *as calculated from the DFT results. The results are convoluted by a Gaussian function with a FWHM of 0.1 eV. The zero position on the energy scale marks the Fermi level.*

In figure (5.7) the DOS of Si_{46}, Na_8Si_{46} and K_8Si_{46} are presented. The Si_{46} host lattice has a completely filled valence band and an empty conduction band at 2 eV above the Fermi energy. This is in good agreement to other publications [Saito 1995, Adams1994, Demkov1994, Melinon1998, Menon1997, Gryko2000, Connetable2001]. The shape of the DOS in the sodium and potassium doped silicon clathrates is almost identical to that of the silicon host lattice but the Fermi level shifts to the middle of the conduction band and the band gap narrows to 1.2 eV. Thus, the electrons of the dopants are filling the conduction band giving rise to the metallic properties of the alkali-metal doped materials. The unchanged shape of the valence band indicates only a weak hybridization of the 3s and 4s electrons of sodium and potassium with the electrons of the silicon host and is consistent with a rigid band model.

In figure (5.8), the DOS of Rb_6Si_{46} is compared with the DOS of the silicon host lattice. Though again, the conduction band is filled by the electrons of the rubidium guest, first changes in the valence bands of the clathrate structure can be observed. The band at -4 eV below the Fermi level broadens and becomes less featured. The same evolution is observed for the band at -7 eV below the Fermi level. This either indicates a hybridization of the 5s electrons of the rubidium atoms with the electrons of the silicon host or a rehybridization of the sp^3 bondings due to the sheer size of the rubidium guest.

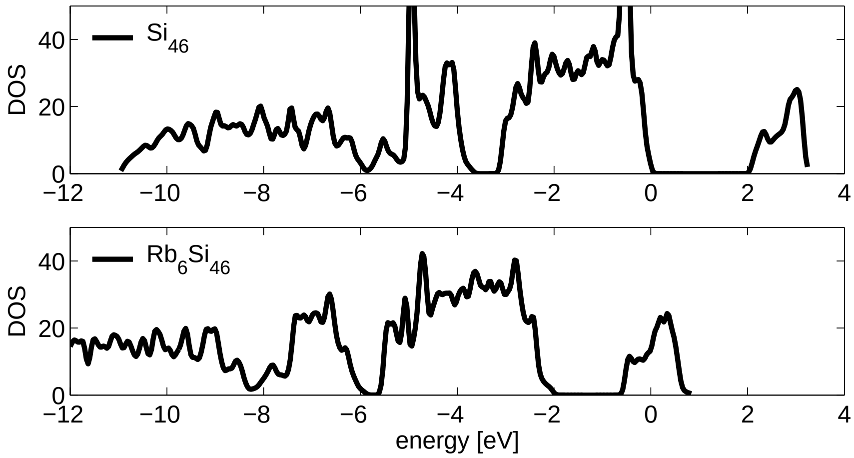

Figure 5.8: *Total electron density of states for Si_{46} and Rb_6Si_{46} as calculated from the DFT results. The results are convoluted by a Gaussian function with a FWHM of 0.1 eV. The zero position on the energy scale marks the Fermi level.*

5.3.2 Mulliken population analysis

To quantify the amount of the charge transfer a Mulliken population analysis is performed [Mulliken1955, Mulliken1962]. It is a widely used scheme for calculating electronic charges. Although the results of the computational scheme depend strongly on the chosen basis set it can easily be calculated within the CRYSTAL code and gives a good idea of the trend of the charge transfer (see e.g. [Wiberg1993, Martin2005]. In table (5.1) the Mulliken charges for the non-equivalent silicon atoms and guest atoms (Na,K, and Rb) are presented. The results suggest a large charge transfer from the alkali-metal atom to the silicon host. There is a general trend, that the transfer reduces with decreasing distance of the guest atom to the silicon lattice. This is most prominent by the variation of the guest atoms size in the larger Si_{24} cages from 0.78 e for sodium to 0.46 e for the rubidium. The same effect is visible when comparing the charge transfer of the smaller Si_{20} with the larger Si_{24} cages. Note, that the smaller cages are not occupied in case of the rubidium doped clathrate.

Table 5.1: *Mulliken charges in alkali-metal doped silicon clathrates.*

Non-equivalent Position of the atoms (M = Na,K,Rb) (Wyckoff notation)	Na_8Si_{46} [e]	K_8Si_{46} [e]	Rb_6Si_{46} [e]
6c Si(1)	-0.14	-0.12	-0.15
16i Si(2)	-0.11	-0.11	-0.01
24k Si(3)	-0.14	-0.14	-0.07
2a M(1) (Si_{20})	0.70	0.69	-
6d M(2) (Si_{24})	0.78	0.72	0.46

5.3.3 Conclusions

As for the experimentally obtained Compton profiles, the further analysis of the DFT results reveals a strong interaction of the alkali-metal guest atoms with the silicon host lattice. In contrast to recent publications [Gryko1996, Pouchard2002] a nearly complete charge transfer of the alkali-metal valence electrons is indicated by the changes of the electron density of states. Especially the results for Na_8Si_{46} and K_8Si_{46} are consistent with a rigid band model. Here, the additional electrons of the metal guests contribute to the DOS by filling the conduction band and shifting the Fermi level to its middle position. The valence bands of sodium and potassium remain nearly unchanged though. First changes of the band structure are observed for the rubidium doped clathrate, a strong hybridization is reported for the heavier barium and iodine guests by Connetable *et al.* [Connetable2001]. These findings are supported by the results of a Mulliken population analysis of the clathrate materials. They show a large charge transfer (see table [5.1]) to the silicon host of 76 %, 71 % and 46 % for the sodium, potassium and rubidium dopants, respectively. The exact amount depends both on the size of the guest atom and the size of the silicon cage. This is exactly the same trend as found by first principles calculations of Conesa *et al.* [Conesa 2004] for Na_8Si_{46}. They find a Mulliken charge of 0.57 e for the Na(1) and of 0.62 e for the Na(2) atom.

Therefore, the results presented here strongly support the ionic character of the alkali-metal dopants proposed by [Moriguchi2000, Tse2000, Moewes2002]. With the results of the Compton measurements presented in this work a very low charge transfer as discussed by e.g. Gryko *et al.* and Pouchard *et al.* referring to a nearly neutral alkali-metal guest atom in the clathrate can be excluded.

Chapter 6

Summary and outlook

The interaction of the trapped guest with the host lattice in silicon clathrates is of special importance and at the origin of the many interesting physical properties like superconductivity, hardness, wide band-gap, and their thermoelectric behaviour. Especially the charge transfer from the alkali-metal guest to the silicon host is discussed controversially in the literature. Therefore, this work presented a systematic theoretical and experimental study of alkali-metal doped silicon clathrates with the focus on the interaction of the alkali-metal valence electrons with the silicon host lattice.

To analyze these interactions Compton scattering experiments on alkali-metal doped silicon clathrates were performed. The valence Compton profiles of the alkali-metal guest atoms were extracted by the use of an adequate reference material. Though hypothetically stable, the empty caged silicon clathrate of structure I could not be synthesized so far. However, it could be evidenced that the available dopant free Si_{136} is a good alternative as a reference material. Systematic errors of the extracted Compton profiles were traced back to silicon and amorphous silicon dioxide impurities using x-ray diffraction and non-resonant x-ray Raman scattering techniques.

The experimental results suggest a strong charge transfer from the alkali-metal guest to the silicon host lattice. A comparison with Hartree-Fock calculated Compton profiles clearly shows, that the trapped atoms are far from being neutral and are not free atoms residing in the middle of the clathrate cages. The comparison with calculated Compton profiles on the basis of Density Functional Theory provides an excellent agreement of the theoretical predictions with the experimental data. Having gained confidence in the theoretical model, the electron density of states has been calculated from there. The results support the idea of a charge transfer. The valence electrons of the dopants are filling the foremost empty conduction band and the Fermi level is shifted following a rigid band model. Therefore, the valence band of the given doped clathrate is nearly unchanged if compared to the empty caged structure and a rehybridization is not taking place. The ionic character of the alkali-metal guest atoms could further be underlined by the results of a Mulliken population analysis. Here, a significant charge transfer is predicted depending on the distance to the silicon host atoms. The larger the guest atom and the smaller the silicon cage, the smaller is the amount of the charge transfer.

For future analysis, the iodine doped silicon clathrate is of particular interest. As the sole dopant being more electronegative than its silicon host, a different guest-host interaction can be expected and could enhance the understanding of the guest-host interactions in general. Furthermore, a systematic analysis of different types of host atoms (Ge, Sn) as well as the study of the electron system under high pressure conditions could give further insight to the complex systems as the distance of the guest atoms to the silicon host is playing a major role in the guest-host interactions. Here, the isostructural volume collapse and the disordering of the alkali-metal guests under high pressure would be of special interest.

An important improvement on the way to understand the physical properties of clathrate materials would be the synthesis of single crystalline clathrate samples enabling the study for example of directional Compton profiles or of the phonon density of states. The phonon coupling plays a key role for understanding superconductivity as well as the low, glass-like thermal conductivity of these materials and is explained by various theoretical models. The verification or falsification of these models would be an important step to develope new and powerful descriptions of clathrate structures.

Appendix A

Diffraction patterns of silicon and silicon clathrates

All diffraction patterns were measured using an imaging plate scanner with a sensitive area of 345 mm in diameter (MAR345). The detector was placed 1006 mm behind the sample, the incident photon energy was 56.74 keV. The MAR picture of the silicon reference sample is depicted in figure (A.1).

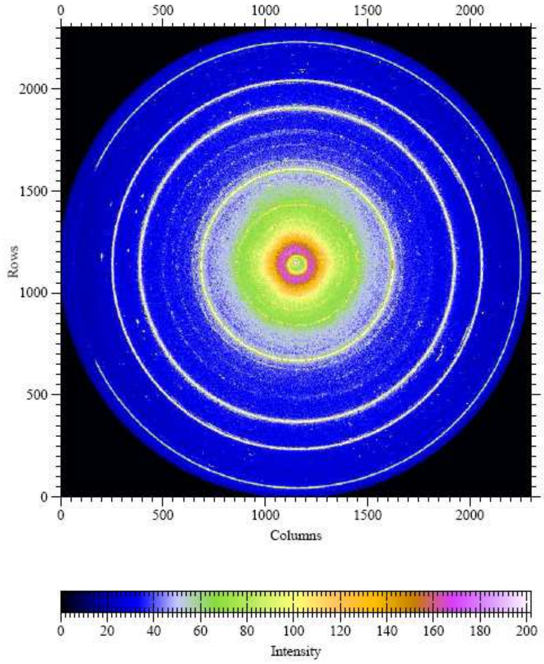

Figure A.1: *Powder diffraction on the silicon sample: The two dimensional image for the silicon sample as obtained by the MAR345 setup of Beamline ID15, ESRF.*

The diffraction pattern was obtained by radially integrating over the two dimensional image after defining the center of the observed Debye rings. This was achieved by using the *Fit2D (v.12.077)* program available at the ESRF webside [ESRF2006, Hummersley1989]. The diffraction pattern for the silicon sample is presented in figure (A.2). The blue lines mark the positions of the expected cd-Si Bragg-reflections. For the Rietveld analysis of Si_{136}, Na_8Si_{46} and $K_{7.6}Si_{46}$, the diffraction pattern of the silicon sample was taken as a reference. The analysis itself was performed by using the GSAS (General Structure Analysis System) code available at the website of the national institute of standards and technology [GSAS2006].

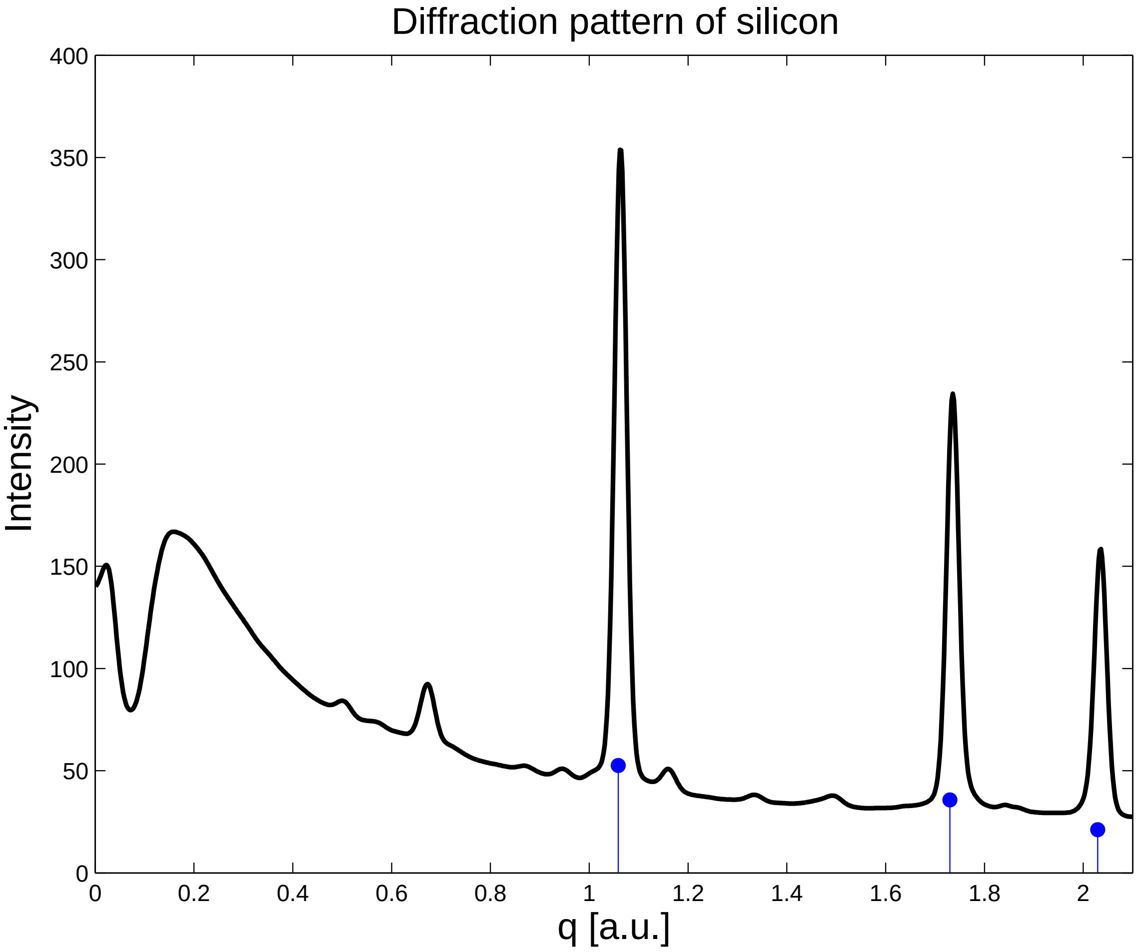

Figure A.2: *Diffraction pattern of the silicon reference sample of setup A (solid black line). The circles depict the expected peak positions.*

Structure I sodium doped clathrate

In figure (A.3) the diffraction pattern of the Na_8Si_{46} sample is presented after the subtraction of the background. The background was determined by fitting a Pearson function to the spectrum. The blue lines mark the Bragg-reflections of cd-Si, the red lines the positions of the clathrate structure peaks. A large cd-Si content is obvious and was veryfied to 28.5 % by the Rietveld analysis.

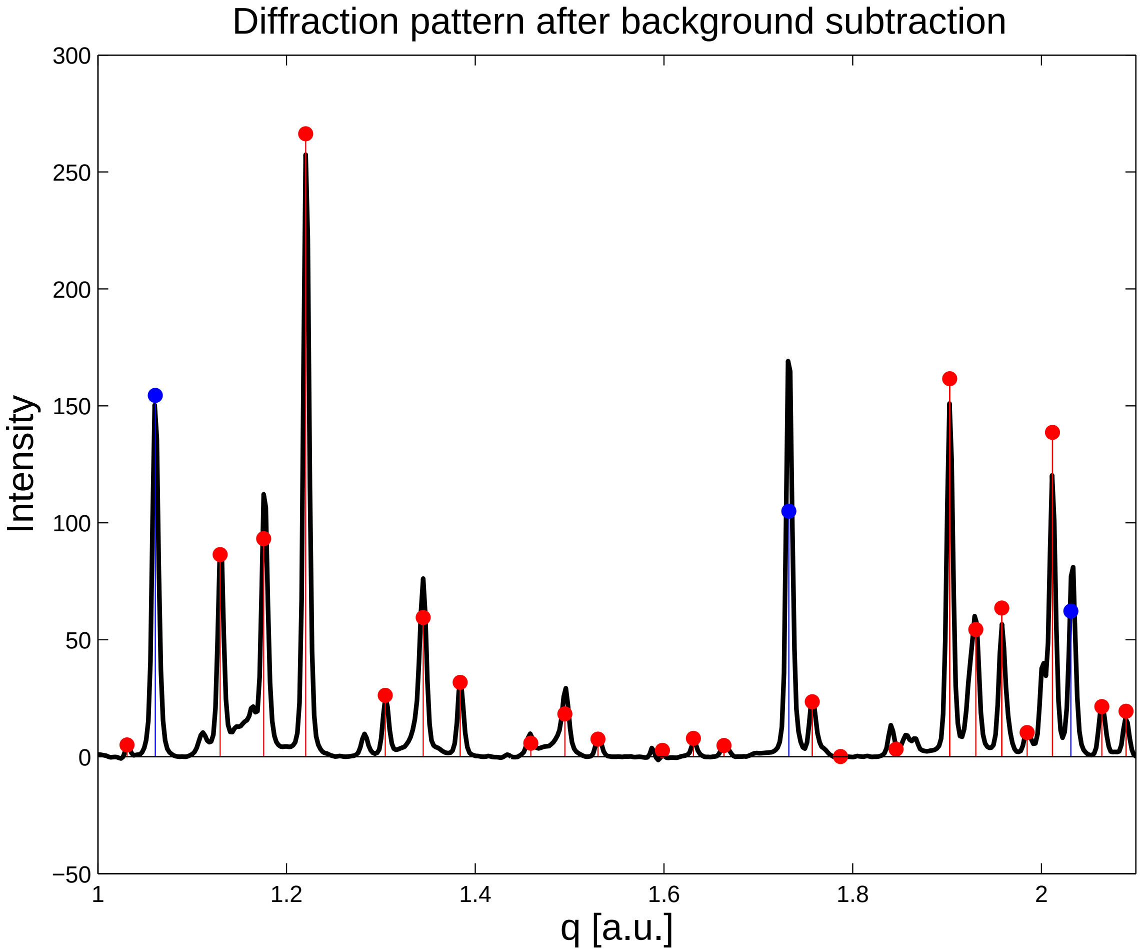

Figure A.3: *Diffraction pattern of the Na_8Si_{46} sample (solid black line). The red circles depict the expected peak positions for the clathrate, the blue circles the expected peak positions of cd-Si.*

In figure (A.4) the result of the Rietveld analysis is presented and is given on a 2 θ scale. The refinement of the diffraction pattern was accomplished by varying the lattice constant, the occupancy of the cages and by adding a variable contribution of cubic diamond silicon phase. The experimental data is depicted by red dots, the green line represents the resulting spectrum of the refinement procedure. The expected positions of the structure peaks of the clathrate and the silicon are marked by the red and the black bars, respectively. The difference spectrum of the refined and the experimentally obtained data is presented as a pink curve. A very good agreement of the refined spectrum with the experimental data is obtained.

Aside the 28.5 % cd-Si content, the refinement varyfied the full occupancy of the Na_8Si_{46} cages and gave a lattice constant of 10.195 Å.

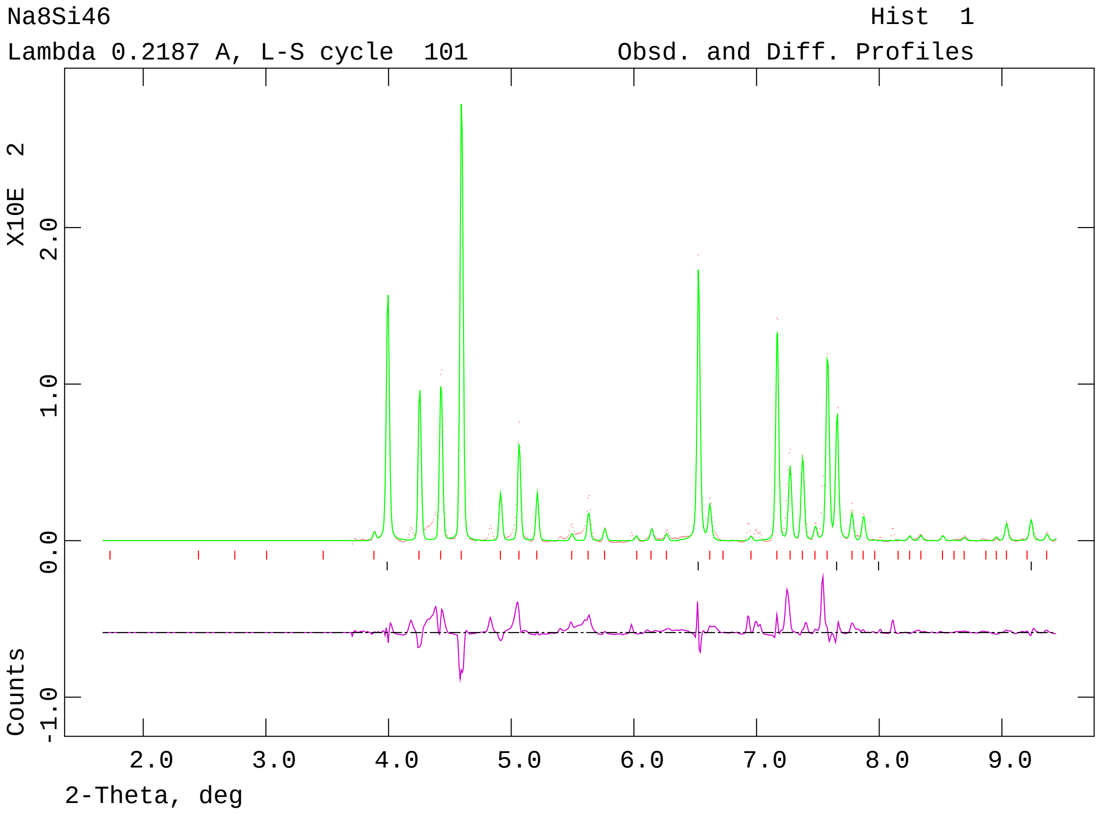

Figure A.4: *Rietveld analysis of the diffraction pattern of Na_8Si_{46}.*

Structure I potassium doped clathrate

In figure (A.5) the diffraction pattern of the $K_{7.6}Si_{46}$ sample is presented after the subtraction of the background. The background was determined by fitting a Pearson function to the spectrum. The red lines mark the positions of the clathrate structure peaks. No cd-Si content is observed in this sample.

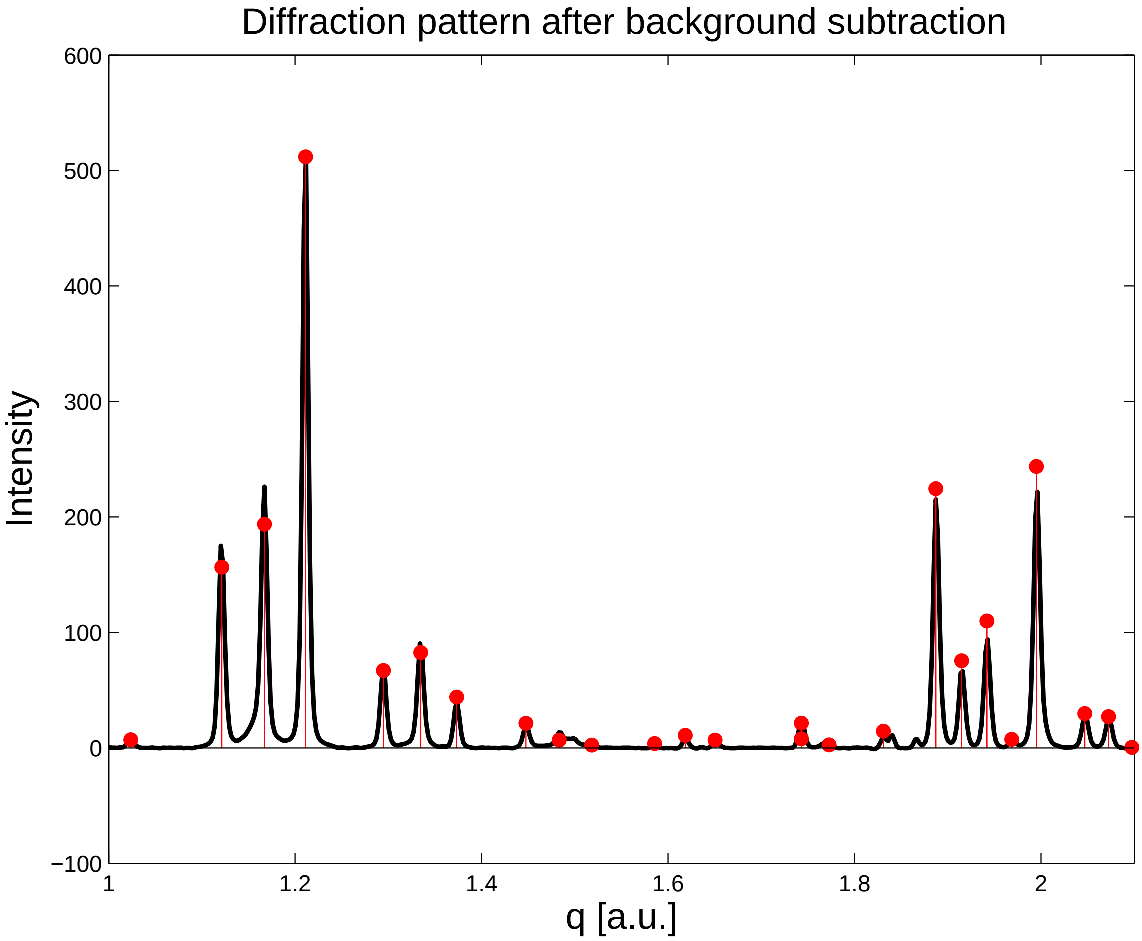

Figure A.5: *Diffraction pattern of the $K_{7.6}Si_{46}$ sample (solid black line). The red circles depict the expected peak positions for the clathrate.*

In figure (A.6) the results of the Rietveld analysis are presented and are given on a 2 θ scale. The refinement of the diffraction pattern was accomplished by varying the lattice constant, the occupancy of the cages and by adding a variable contribution of cubic diamond silicon phase. The experimental data is depicted by red dots, the green line represents the resulting spectrum of the refinement procedure. The expected positions of the structure peaks of the clathrate and the silicon are marked by the red bars. The difference spectrum of the refined and the experimentally obtained data is presented as a pink curve.

The refinement found a nearly full occupancy of the $K_{7.6}Si_{46}$ cages of 7.6 atoms per unit cell. The lattice constant of was determined to 10.195 Å.

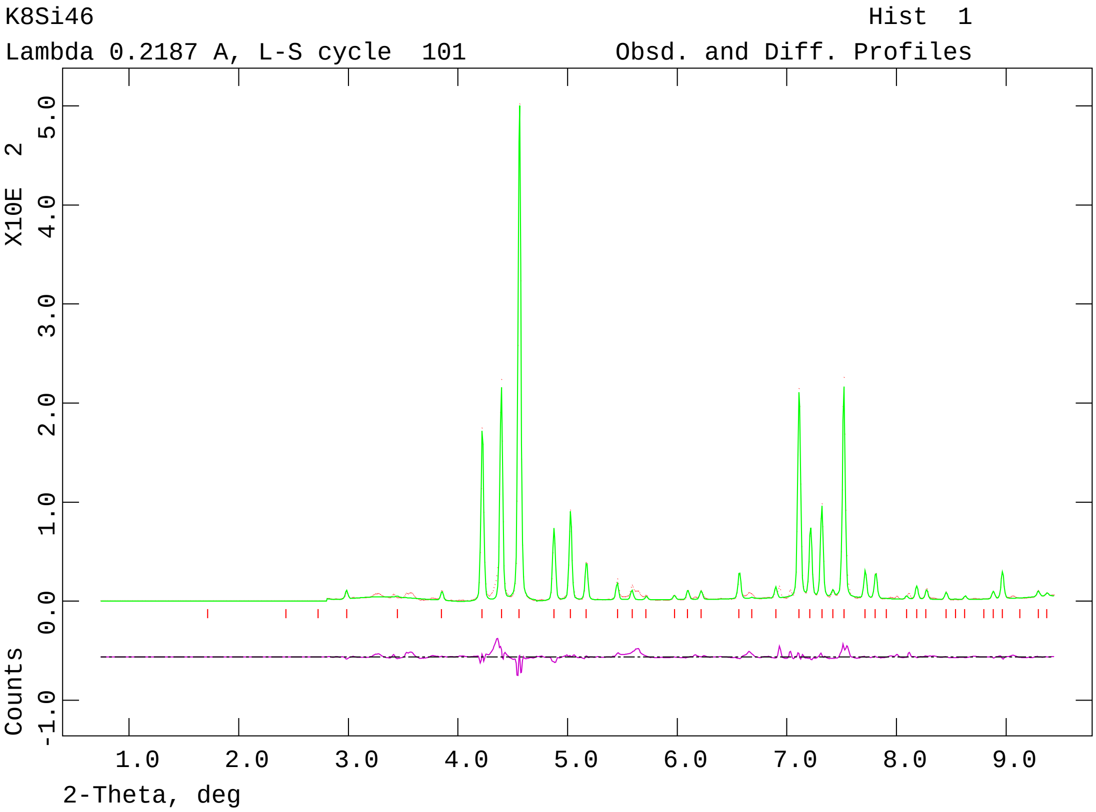

Figure A.6: *Rietveld analysis of the diffraction pattern of* $K_{7.6}Si_{46}$.

Structure II silicon clathrate

In figure (A.7) the diffraction pattern of the Si_{136} sample is presented after the subtraction of the background. The background was determined by fitting a Pearson function to the spectrum. The red lines mark the positions of the clathrate structure peaks. The cd-Si content is determined to 4 %.

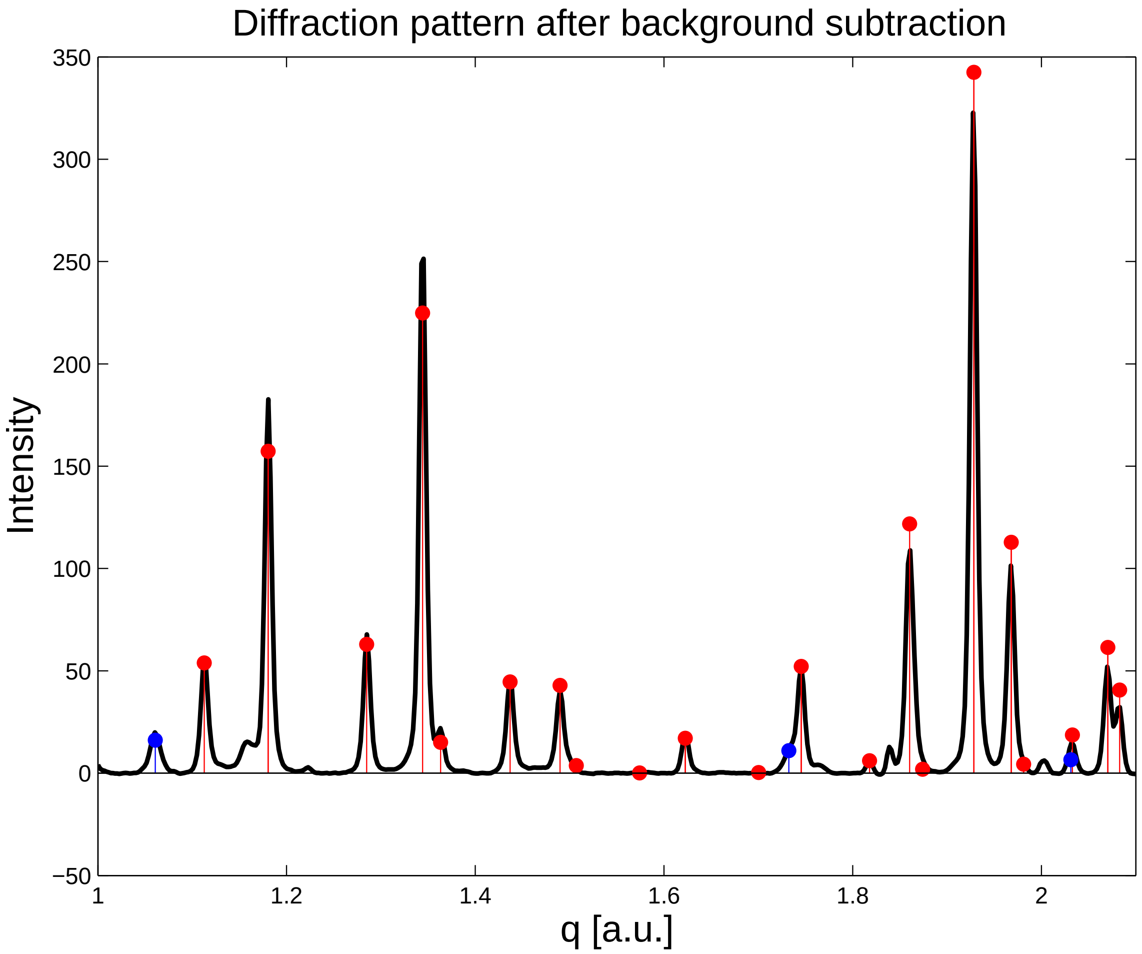

Figure A.7: *Diffraction pattern of the Si_{136} reference sample of setup A (solid black line). The circles depict the expected peak positions for the clathrate, the squares the expected peak positions of cd-Si. The Rietveld analysis gave a 4 % cd-Si content in the sample.*

Subtraction procedure for the silicon and amorphous silicon dioxide contents in the clathrate samples

For the subtraction of the silicon and the amorphous silicon dioxide contents, the experimental Compton profiles of silicon (setup A) and amorphous silicon dioxide (setup B) have been used. The silicon content n_{Si} is determined by the Rietveld analysis of the according diffraction pattern, the $\mathrm{SiO_2}$ content $n_{\mathrm{SiO_2}}$ by the analysis of the given Compton profiles.

Silicon content in Si_{136}

As both samples consist solely of silicon atoms, the Compton profiles are normalized to 14 electrons per atom. Thus, the diamond silicon contribution to the total Compton profile $J_{\mathrm{Si}}(p_z)$ can be subtracted directly from the measured spectrum. Afterwards, the obtained Si_{136} Compton profile has to be rescaled to a 100 % content:

$$J_{\mathrm{corr}}(p_z) = \frac{J(p_z) - n_{\mathrm{Si}} \cdot J_{\mathrm{Si}}(p_z)}{1 - n_{\mathrm{Si}}} \,. \tag{A.1}$$

Silicon and silicon dioxide content in $\mathrm{Na_8Si_{46}}$ and $\mathrm{K_{7.6}Si_{46}}$

The subtraction procedure for $\mathrm{Na_8Si_{46}}$ and $\mathrm{K_{7.6}Si_{46}}$ is somewhat more complex, as the experimental data has to be renormalized before the silicon and the silicon dioxide contributions can be subtracted:

$$J_{\mathrm{ren}}(p_z) = J(p_z) \cdot \frac{\int \left[(1 - n_{\mathrm{Si}} - n_{\mathrm{SiO_2}}) \cdot J(p_z) + n_{\mathrm{Si}} \cdot J_{\mathrm{Si}} + n_{\mathrm{SiO_2}} \cdot J_{\mathrm{SiO_2}}\right] dp_z}{\int J(p_z)\, dp_z} \,. \tag{A.2}$$

Again, the corrected spectra have to be rescaled to a 100 % content:

$$J_{\mathrm{corr}}(p_z) = \frac{J_{\mathrm{ren}}(p_z) - n_{\mathrm{Si}} \cdot J_{\mathrm{Si}}(p_z) - n_{\mathrm{SiO_2}} \cdot J_{\mathrm{SiO_2}}(p_z)}{1 - n_{\mathrm{Si}}} \,. \tag{A.3}$$

Bibliography

[Adams1994] G.B. Adams, M. O'Keeffe, A.A. Demkov, O.F. Sankey, Y.M. Huang, Phys. Rev. B **49** 8048 (1994)

[Ammar2004] A. Ammar, C. Cros, M. Pouchard, N. Jaussaud, J.-M. Bassat, G. Villeneuve, M. Duttine, M. Menetrie, and E. Reny, Solid State Sci. **6** 393 (2004)

[Ashcroft1976] N.W. Ashcroft and N.D. Mermin, Solid State Physics (Brooks/Cole, 1976)

[Barone1994] V. Barone, Chem. Phys. Lett. **226** 392 (1994)

[Becke1988] A.D. Becke, J. Chem. Phys. **38** 3098 (1988)

[Biggs1975] F. Biggs, L.B. Mendelsohn, J.B. Mann, Atomic Data and Nuclear Data Tables **16** 201 (1975)

[Bardeen1957] J. Bardeen, L.N. Cooper, and J.R. Schrieffer, Phys. Rev. **108** 1175 (1957) and J. Bardeen, L.N. Cooper, and J.R. Schrieffer, Phys. Rev. **106** 162 (1957)

[Blake1999] N.P. Blake, L. Mollnitz, G. Kresse, and H. Metiu, J. Chem. Phys. **111** 3133 (1999)

[Blase2003] X. Blase, Phys. Rev. B **67** 35211 (2003)

[Brunet2000] F. Brunet, P. Melinon, A. San-Miguel, P. Keghelian, A. Perez, A.M. Flank, E. Reny, C. Cros, M. Pouchard, Phys. Rev. B **61** 16550 (2000)

[Cohn1999] J.L. Cohn, G.S. Nolas, V. Fessatidis, T.H. Metcalf, and G.A. Slack, Phys. Rev. Lett. **82** 779 (1999)

[Compton1923] A.H. Compton, Phys. Rev. **21** 483 (1923)

[Conesa 2004] J.C. Conesa, C. Tablero, and P. Wahnon, J. Chem. Phys. **120** 6142 (2004)

[Connetable2001] D. Connetable, V. Timoshevskii, E. Artacho, and X. Blase, Phys. Rev. Lett. **87** 206405 (2001)

[Connetable2003] D. Connetable, V. Timoshevskii, B. Masenelli, J. Beille, J. Marcus, B. Barbara, A.M. Saitta, G.-M. Rignanse, P. Melinon, S. Yamanaka, and X. Blase, Phys. Rev. Lett. **91** 247001 (2003)

[Cooper2004] M.J. Cooper, P.E. Mijnarends, N. Shiotani, N. Sakai, and A. Bansil, X-Ray Compton Scattering (Oxford University Press, 2004)

[Cordier1991] G. Cordier and P. Woll, J. Less-Common Met. **169** 291 (1991)

[Cros1965] C. Cros, M. Pouchard, P. Hagenmuller, Compte. Rendu. Acad. Sci. Paris **260** 4764 (1965)

[Cros1970] C. Cros, M. Pouchard, P. Hagenmuller, J. Solid State Chem. **2** 570 (1970)

[Cros1971] C. Cros, M. Pouchard, P. Hagenmuller, Bull. Soc. Chim. Fr. **2** 379 (1971)

[Cros1972] C. Cros and J.C. Benejan, Bull. Soc. Chim. Fr. **5** 1739 (1972)

[Crystal2006] http://www.crystal.unito.it/ (2006)

[Demkov1994] A.A. Demkov, O.F. Sankey, K.E. Schmidt, G.B. Adams, M. O'Keeffe, Phys. Rev. B**50** 17001 (1994)

[Dong2001] J. Dong, O.F. Sankey, and C.W. Myles, Phys. Rev. Lett. **86** 2361 (2001)

[DuMond1929] J.W.M. DuMond, Phys. Rev. **33** 643 (1929)

[DuMond1933] J.W.M. DuMond, Rev. Mod. Phys. **5** 628 (1933)

[Eisenberger1970] P. Eisenberger and P.M. Platzmann, Phys. Rev. A **2** 415 (1970)

[Eisenberger1972] P. Eisenberger, Phys. Rev. A **5** 628 (1972)

[Erola1990] E. Erola, V. Eteläniemi, P. Suortti, P. Pattison, and W. Thomlinson, J. Appl. Cryst. **23** 35 (1990)

[ESRF2006] European Synchrotron Radiation Facility (ESRF), http://www.esrf.fr (2006)

[Fang1998] S.L. Fang, L. Grigorean, P.C. Eklund, G. Dresselhaus, H. Kawaji, and S. Yamanaka, Phys. Rev. B **57** 7686 (1998)

[Fujita2006] I. Fujita, K. Kishimoto, M.Sato, H. Anno, and T. Koyanagi, J. Appl. Phys. **99** 093707 (2006)

[Gallmeier1967] J. Gallmeier, H. Schäfer, A.Weiss, Z. Naturforschung B **22** 1080 (1967)

[Gallmeier1969] J. Gallmeier, H. Schäfer, A.Weiss, Z. Naturforschung B **24** 665 (1969)

[Gao2005] X. Gao, K. Uehera, D.D.Klug, S. Patchkovskii, J.S. Tse, and T.M. Tritt, Phys. Rev. B **72** 125202 (2005)

[Goldsmid1986] H.J. Goldsmid, Electronic Refrigeration (Pion Limited, 1986)

[Gryko1996] J. Gryko, P.F. McMillan, and O.F. Sankey, Phys. Rev. B **54** 3037 (1996)

[Gryko 1998] J. Gryko, P.F. McMillan, R.F. Marzke, A.P. Dodokin, A.A. Demkov, and O.F. Sankey, Phys. Rev. B **57** 4172 (1998)

[Gryko2000] J. Gryko, P.F. McMillan, R.F. Marzke, G.K. Ramachandran, D. Petton, S.K. Deb, and O.F. Sankey, Phys. Rev. B **62** R7707 (2000)

[GSAS2006] General Structural Analysis System (GSAS), available at http://www.ncnr.nist.gov/xtal/software/gsas.html (2006)

[Guyot1998] Y. Guyot, B. Champagnon, E. Reny, C. Cros, M. Pouchard, P. Melinon, A. Perez, and I. Gregora, Phys. Rev. B **57** R9475 (1998)

[Guyot1999] Y. Guyot, L. Grosvalet, B. Champagnon, E. Reny, C. Cros, and M. Pouchard, Phys. Rev. B **60** 14507 (1999)

[He2001] J. He, D.D. Klug, K. Uehara, K.F. Preston, C.I. Ratcliffe, and J.S. Tse, J. Phys. Chem. B **105** 3475 (2001)

[Hebard1991] A.F. Hebard, M.S. Rosseinsky, R.C. Haddon, D.W. Murphy, S.H. Glarum, T.T.M. Palstra, A.P. Ramirez, and A.R. Kortan, Nature **350** 600 (1991)

[Hermann1998] R. Herrmann, K. Tanigaki, S. Kuroshima, and H. Suematsu, Chem. Phys. Lett. **282** 14532 (1998)

[Hiraoka2005] Hiraoka N, Buslaps T, Honkimaki V, Suortti P, J. Syn. Radiation **12** 670 (2005)

[Hiraoka2006] Hiraoka N, private communication (2006)

[Hohenberg1964] P. Hohenberg and W. Kohn, Phys. Rev. **136** B864 (1964)

[Holm1988] P. Holm, R. Ribberfors, Phys. Rev. A **37** 3706 (1988)

[Holm1989] P. Holm, R. Ribberfors, Phys. Rev. A **40** 6251 (1989)

[Honkamäki2006] V. Honkamäki, private communications (2006)

[Hummersley1989] A.P. Hummersley, Synchrotron Radiat. News **2** 24 (1989)

[Huotari2001] S. Huotari, K. Hämäläininen, S. Manninen, A. Issolah, and M. Marangolo, J. Phys. Chem. Sol. **62** 2205 (2001)

[Ioffe1957] A. F. Ioffe, Semiconductor Thermoelements and Thermoelectric Cooling, Infosearch Ltd. (1957)

[Itou2005] M. Itou, Y. Sakurai, M. Usuda, C. Cros, H. Fukuoka, S. Yamanaka, Phys. Rev. B **71** 125125 (2005)

[Iversen2000] B.B. Iversen, L. Molnitz, G. Kresse, and H. Metiu, J. Solid State Chem. **149** 455 (2000)

[Kahn1997] D. Kahn and J.P. Lu, Phys. Rev. B **56** 13898 (1997)

[Kappeler1936] H. Kappeler, Ann. der Physik **27** 129 (1936)

[Kasper1965] J.S. Kasper, P. Hagenmuller, M. Pouchard, C. Cros, Science **150** 1713 (1965)

[Kawaji1995] H. Kawaji, H.-o. Horie, S. Yamanaka, and M. Ishikawa, Phys. Rev. Lett. **74** 1427 (1995)

[Kohn1965] W. Kohn, L.J. Sham, Phys. Rev. **140** A1133 (1965)

[Kralik1998] B. Kralik, P. Delaney, and S.G. Louie, Phys. Rev. Lett. **80** 4253 (1998)

[Kramers1925] H.A. Kramers, W. Heisenberg, Z. Physik **31** 681 (1925)

[Kume2003] T. Kume, H. Fukuoka, T. Koda, S. Sasaki, H. Shimizu, and S. Yamanaka, Phys. Rev. Lett. **90** 155503 (2003)

[Kume2004] T. Kume, T. Koda, S. Sasaki, H. Shimizu, and J. Tse, Phys. Rev. B **70** 52101 (2004)

[Li1994] D. Li, G.M. Bancroft, M. Kasrai, M.E. Flut, R.E. Secco, X.H. Feng, K.H. Tan, B.X. Yang, Am. Mineral. **79** 622 (1994)

[Loewdin1955] P.-O. Loewdin, Phys. Rev. **97** 1474 (1955)

[MAR345] For specifications see http://www.marresearch.com/

[Martin2005] F. Martin, H. Zipse, J. Comput. Chem. **26** 97 (2005)

[Melinon1998] P. Melinon, P. Keghelian, X. Blase, J. Le Brusc, A. Perez, E. Reny, C. Cros, and M. Pouchard, Phys. Rev. B **58** 12590 (1998)

[Melinon1999] P. Melinon, P. Keghelian, A. Perez, B. Champagnon, Y. Guyot, L Savoit, E. Reny, C. Cros, M. Pouchard, and A.J. Dianoux, Phys. Rev. B **59** 10099 (1999)

[Menon1997] M. Menon, E. Richter, and K.R. Subbaswamy, Phys. Rev. B **56** 12290 (1997)

[Mizuno1967] Y. Mizuno and Y. Ohmura, J. Phys. Soc. Jpn. **22** 445 (1967)

[Moewes2002] A. Moewes, E.Z. Kurmaev, J.S. Tse, M. Geshi, M.J. Ferguson, V.A. Trofimova, and Y.M. Yarmoshenko, Phys. Rev. B **65** 153106 (2002)

[Monkhorst1976] H.J. Monkhorst, J.D. Pack, Phy Rev. B **13** 5188 (1976)

[Moriguchi2000] K. Moriguchi, M. Yonemura, and A. Shintani, Phys. Rev. B **61** 9859 (2000)

[Mott1973] N.F. Mott, J. Solid State Chem. **6** 348 (1973)

[Mudryk2002] Y. Mudryk, P. Rogl, C. Paul, S. Berger, E. Bauer, G. Hilscher, C. Godart, and H. Noel, J. Phys.: Cond. Matt. **14** 7991 (2002)

[Mulliken1955] R.S. Mulliken, J. Chem. Phys. **23** 1833 (1955)

[Mulliken1962] R.S. Mulliken, J. Chem. Phys. **36** 3428 (1962)

[Nolas1998] G.S. Nolas, J.L. Cohn, G.A. Slack, and S.B. Schujman, Appl. Phys. Lett. **73** 178 (1998)

[Nolas2003] G.S. Nolas, M. Beekman, J. Gryko, G.A. Lamberton, Jr., T.M. Tritt, and P.F. McMillan, Appl. Phys. Lett. **82** 910 (2003)

[Nistor1994] L. Nistor, G. van Tendeloo, S. Amelinckx, and C. Cros, Phys. Status Solidi **146** 119 (1994)

[Pauling1952] L. Pauling and R.E. Marsh, Proc. Natl. Acad. Sci. **36** 112 (1952)

[Perdew1992] J.P. Perdew and Y. Wang, Phys. Rev. B **45** 13244 (1992)

[Pitkänen1987] T. Pitkänen, M.J. Cooper, D. Laundy, and R.S. Holt, Nucl. Instrum. Methods A **257** 384 (1987), see also Ref. [Cooper2004] p. 152

[Pouchard2002] M. Pouchard, C. Cros, P. Hagenmuller, E. Reny, A. Ammar, M. Menetrier, J.-M. Bassart, Solid State Sciences **4** 723 (2002)

[Powell1948] H.J. Powell, J.Chem. Soc. **1** 61 (1948)

[Qiu2001] L. Qiu, M.A. White, Z. Li, J.S. Tse, C.I. Ratcliffe, C.A. Tulk, J. Dong, and O.F. Sankey, Phys. Rev. B **64** 24303 (2001)

[Ramachandran1998] G.K. Ramachandran, J. Diefenbacher, O.F. Sankey, R. Sharma, R.F. Marzke, M. O'Keeffe, J. Gryko and P.F. McMillan, Mat. Res. Soc. Symp. Proc. **507** 483 (1998)

[Ramachandran1999(b)] G.K. Ramachandran, J. Dong, J. Diefenbacher, J. Gryko, R.F. Marzke, O.F. Sankey,and P.F. McMillan, J. Solid State Chem. **45** 716 (1999)

[Ramachandran1999(a)] G.K. Ramachandran and P.F. McMillan, Phys. Rev. B **60** 12294 (1999)

[Ramachandran2000] G.K. Ramachandran, P.F. McMillan, S.K. Deb, M.Somayazulu, J. Gryko, J. Dong, and O.F. Sankey, J. Phys.: Condens. Matter **12** 4013 (2000)

[Reny1998] E. Reny, P. Gravereau, C. Cros, and M. Pouchard, J. Mat. Chem. **8** 2839 (1998)

[Reny2000] E. Reny, S. Yamanaka, C. Cros, and M. Pouchard, Chem. Comm. p. 2839 (2000)

[Reny2002(a)] E. Reny, S. Yamanaka, C. Cros and M. Pouchard, J. Phys.: Cond. Matt. **14** 11233 (2002)

[Reny2002(b)] E. Reny, A. San-Miguel, Y. Guyot, B. Masenelli, P. Melinon, L. Savoit, S. Yamanaka, B. Champagnon, C. Cros, M.Pouchard, M. Borowski, and A.J. Dianoux, Phys. Rev. B **66** 14532 (2002)

[Ribberfors1975] R. Ribberfors, Phys. Rev. B **12** 2067 (1975)

[ROSSEINSKY1991] M.J. Rosseinsky, A.P. Ramirez, S.H. Glarum, D.W. Murphy, R.C. Haddon, A.F. Hebard, T.T. Palstra, A.R. Kortan, S.M. Zahurak, and A.V. Makhija, Phys. Rev. Lett. **66** 2830 (1991)

[ROY1992] S.B. Roy, K.E. Sim, and A.D. Caplin, Philos. Mag. B **65** 1445 (1992)

[SAITO 1995] S. Saito and A. Oshiyama, Phys. Rev. B **51** 2628 (1995)

[SAN-MIGUEL1999] A. San-Miguel, P. Keghelian, X. Blase, P. Melinon, A. Perez, J.P. Itie, A. Polian, E. Reny, C. Cros, and M. Pouchard, Phys. Rev. Lett. **83** 5290 (1999)

[SAN-MIGUEL2002] A. San-Miguel, P. Melinon, D. Connetable, X. Blase, F. Tournus, E. Reny, S. Yamanaka, and J.P. Itie, Phys. Rev. B **65** 54109 (2002)

[SAN-MIGUEL2005 (A)] A. San-Miguel, A. Merlen, P. Toulemonde, T. Kume, S. Le Floch, A. Aouizerat, S. Pascarelli, G. Aquilanti, O. Mathon, T. Le Bihan, J.P. Itie, and S. Yamanaka, Europhys. Lett. **69** 556 (2005)

[SAN-MIGUEL2005 (B)] A. San-Miguel and P. Toulemonde, High Pressure Research **25** 159 (2005)

[SCHÜLKE1991] W. Schülke in Handbook on Synchrotron Radiation Vol. 3, edited by G.S. Brown and D.E. Moncton (Elsevier, 1991)

[SCHÜLKE2004] W. Schülke in *X-Ray Compton Scattering* (2004) , see also [Cooper 2004]

[SHIMIZU1996] F. Shimizu, Y. Maniwa, K. Kume, H. Kawaji, S. Yamanaka, and M. Ishikawa, Phys. Rev. B **54** 13242 (1996)

[SLACK1995] G. Slack in CRC Handbook of Thermoelectrics, pp. 407-440. edited by D.M. Rowe (CRC Press, 1995)

[SLOAN1998] E.D. Sloan Jr., *Clathrate Hydrates of Natural Gases* (Marcel Dekker, New York, 1998)

[Stephens1994] P.J. Stephens, F.J. Devlin, C.F. Chabalowski, M.J. Frisch, J. Phys. Chem. **98** 11623 (1994)

[Sternemann2000] C. Sternemann, K. Hämäläinen, A. Kaprolat, A. Soininen, G. Döring, C.-C. Kao, S. Manninen, W. Schülke, Phys. Rev. B **62**, R7687 (2000)

[Sternemann2003] C. Sternemann, M. Volmer, J.A. Soininen, H. Nagasawa, M. Paulus, H. Enkisch, G. Schmidt, M. Tolan, W. Schülke, Phys. Rev. B **68**, 35111 (2003)

[Sternemann2005] C. Sternemann, J.A. Soininen, S. Huotari, G. Vanko, M. Volmer, R.A. Secco, J.S. Tse, M. Tolan, Phys. Rev. B, **72**, 35104 (2005)

[Suortti1995] P. Suortti, T. Tschentscher, Rev. Sci. Instruments **66** 1798 (1995)

[Suortti1999] P. Suortti, T. Buslaps, P. Fajardo, V. Honkimaki, M. Kretzschmer, U. Lienert, J.E. McCarthy, M. Renier, A. Shukla, T. Tschentscher, T. Meinander, J. Synchrotron Rad. **6** 69 (1999)

[Suortti2001] P. Suortti, T. Buslaps, M. DiMichiel, V. Honkimaki, U. Lienert, J.E. McCarthy, J.M. Merino, A. Shukla, Nuclear Instruments & Methods in Physics Research Sectiom A-Accelerators Spectrometers Detectors and Associated Equipment **467** 1541 (2001)

[Tanigaki1991] K. Tanigaki, T.W. Ebbesen, S. Saito, J. Mizuki, J.S. Tsai, Y. Kubo, andS. Kuroshima, Nature **352** 222 (1991)

[Tournus2004] F. Tournus, B. Masenelli, P. Melinon, D. Connetable, X. Blase, A.M. Flank, P. Lagarde, C. Cros, M. Pouchard, Phys. Rev. B **69** 35208 (2004)

[Tse2000] J.S. Tse, K. Uehara, R. Rousseau, A. Ker, C.I. Ratcliffe, M.A. White, and G. MacKay, Phys. Rev. Lett. **85** 114 (2000)

[Tse2001] J.S. Tse, Z. Li, and K. Uehara, Europhys. Lett. **56** 261 (2001)

[Tse2002] J.S. Tse, S. Desgreniers, Z. Li, M.R. Ferguson, and Y. Kawazoe, Phys. Rev. Lett. **89** 195507 (2002)

[Tse2005] J.S. Tse, D.D. Klug, J.Y. Zhao, W. Sturhahn, E.E. Alp, J. Baumert, C. Gutt, M.R. Johnson, and W. Press, Nature Mat. **4** 917 (2005)

[Tse2006] All DFT calculations have been performed by J.S. Tse.

[Univ. of Liege 2006] from the website of the University of Liege, downloaded in 2006: http://www.ulg.ac.be/le15jour/106/S05.html

[Wiberg1993] K.B. Wiberg, P.R. Rablen, J. Comput. Chem. **14** 1504 (1993)

[Williams1977] B.G. Williams, *Compton Scattering*, (McGraw Hill, New York, 1977)

[Wyckoff1963] R.W.D. Wyckoff, *Crystal Structures*, (Interscience Publishers, Inc. 1963) and references therein.

[Yamanaka1995] S. Yamanaka, H. Horie, H. Nakano, and M. Ishikawa, Fullerene Sci. Tech. **3** 21 (1995)

[Yamanaka2000] S. Yamanaka, E. Enishi, H. Fukuoka, and M. Yasukawa, Inorg. Chem. **39** 56 (2000)

[Yin1982] M.T. Yin, and M.L. Cohen, Phys. Rev. B **26** 5668 (1982)

[Yokoya2001] T. Yokoya, A. Fukuchima, T. Kiss, K. Kobayashi, S. Shin, K. Moriguchi, A. Shintani, H. Fukuoka, and S. Yamanaka, Phys. Rev. B **64** 172504 (2001)

List of Figures

Publications

C. Sternemann, M. Volmer, J.A. Soininen, H. Nagasawa, M. Paulus, H. Enkisch, G. Schmidt, M. Tolan, W. Schülke, *Momentum-transfer dependence of x-ray Raman scattering at the Be K-edge*, Phys. Rev. B **68**, 35111 (2003)

H. Enkisch, C. Sternemann, M. Paulus, M. Volmer, W. Schülke, *3d spectator hole satellites of the Cu* $K\beta_{1,3}$ *and* $\beta_{2,5}$ *emission spectrum*, Phys. Rev. A, **70**, 22508 (2004)

C. Sternemann, J.A. Soininen, S. Huotari, G. Vanko, M. Volmer, R.A. Secco, J.S. Tse, M. Tolan, *X-ray Raman scattering at the L edges of elemental Na, Si, and the N edge of Ba in* Ba_8Si_{46}, Phys. Rev. B, **72**, 35104 (2005)

M. Paulus, R. Fendt, C. Sternemann, C. Gutt, H. Hövel, M. Volmer, M. Tolan, K. Wille, *An internet-based synchrotron experiment for students measuring the X-ray magnetic circular dichroism of PtFe alloy*, Journal of Synchrotron radiation **12**, 246 (2005)

C. Sternemann, S. Huotari, G. Vanko, M. Volmer, G. Monaco, A. Gusarov, H. Lustfeld, K. Sturm, W. Schuelke, *Correlation-induced double-plasmon excitation in simple metals studied by inelastic X-ray scattering*, Phys. Rev. Lett. **95**, 157401 (2005)

J.S. Tse, D.D. Klug, D.T. Jiang, C. Sternemann C, M. Volmer, S. Huotari, N. Hiraoka, V. Honkimäki, K. Hämäläinen, *Compton scattering of elemental silicon at high pressure*, Appl. Phys. Lett. **87**, 191905, (2005)

C. Sternemann, J.A. Soininen, M. Volmer, A. Hohl, G. Vanko, S. Streit, M. Tolan, *X-ray Raman scattering at the Si L-II,(III)-edge of bulk amorphous SiO*, Journal of Physics and Chemistry of Solids **66**, 2277, (2005)

C. Krywka, M. Paulus, C. Sternemann, M. Volmer, A. Remhof, G. Nowak, A. Nefedov, B. Pöter, M. Spiegel, M. Tolan, *The new diffractometer for surface diffraction at BL9 of DELTA*, Journal of Synchrotron radiation, **13**, 8 (2006)

C. Sternemann, S. Huotari, M. Hakala, M. Paulus, M. Volmer, C. Gutt, T. Buslaps, N. Hiraoka, D.D. Klug, K. Hämäläinen , M. Tolan, J.S. Tse, *Electronic stucture of methane hydrate studied by Compton scattering*, Phys. Rev. B, **73**, 195104 (2006)

Acknowledgements

First of all I would like to thank my supervisor Christian Sternemann for the support he has given to me over the last four and a half years. Without him this work would not have been possible and his advise is always welcome not only as a scientist but also as a friend. I also like to thank Mr. Tolan for giving me the opportunity to work in his group for the last years and for providing me with all the freedom I needed. Of course I want to thank Michael Paulus. From the first days of my studies we have worked together and he has become a dear friend in the course of the years.

It has always been a pleasure to work with all the people at EIa and DELTA and I want to thank all of them for the constructive atmosphere. Especially, I want to thank Henning Sternemann and Saskia Schmacke for supporting me in many ways during the last weeks of this work and Peter Heines for helping with the Rietveld analysis of the diffraction patterns.

As an international collaboration, this work was supported by many people. First of all I would like to mention John S. Tse who calculated all the spectra and provided most of the samples. He also joined in many of the experiments and gave his support in fruitful discussions. I also like to thank Simo Huotari for helping me with the multiple scattering calculations. He has been of invaluable help in many discussions. I will remember many hours of hard work, of playing pool and of course of singing Jesus Christ Superstar. Finally, I like to thank the beamline staff of ID15 and ID16 at the ESRF for giving their support for the numerous experiments I was able to perform at their facility.

Danksagung

Zuallererst möchte ich meinen Eltern danken. Ihr habt schon früh in meinem Leben den Mut bewiesen mir alle wichtigen Entscheidungen selbst zu überlassen. Obwohl ich sicher nicht immer die richtigen Entscheidungen getroffen habe, so hat es mir dennoch Selbstbewusstsein und Vertrauen gegeben. Ohne beides hätte ich weder das Studium und sicher nicht die letzten Wochen dieser Arbeit durchgestanden.

Die letzten Worte sollen meiner Frau Tanja gewidmet sein. Deine Liebe und Dein Vertrauen geben mir einen festen Anker im Leben und sicher habe ich es einer kleinen Kopfwäsche zu verdanken, das Studium überhaupt so gut abgeschlossen zu haben. Für all das danke ich Dir.

Eidesstattliche Erklärung

Hiermit erkläre ich an Eides Statt, dass die vorliegende Dissertation - abgesehen von der Beratung durch meine wissenschaftlichen Lehrer - nach Inhalt und Form meine eigene Arbeit ist. Sie wurde weder ganz noch in Teilen an anderer Stelle im Rahmen eines Prüfungsverfahrens vorgelegt. Frühere Promotionsversuche wurden von mir nicht vorgenommen.

Dortmund, Juni 2006

(Martin Volmer geb. Schenkel)